Using the balance function to search for late hadronization in Au+Au collisions at a center of mass energy of 130 GeV per nucleon pair

By

Marguerite Belt Tonjes

A DISSERTATION

Submitted to
Michigan State University
in partial fulfillment of the requirements
for the Degree of

DOCTOR OF PHILOSOPHY

Department of Physics and Astronomy

2002

ABSTRACT

Using the balance function to search for late hadronization in Au+Au collisions at a center of mass energy of 130 GeV per nucleon pair

By

Marguerite Belt Tonjes

Relativistic heavy ion physics is the study of nuclear matter interacting at high energies and densities. The collisions of gold nuclei at the Relativistic Heavy Ion Collider (RHIC) provide a source of high density matter for the study and creation of a novel state of matter, the Quark-Gluon Plasma(QGP). The data set studied in this dissertation is taken from Au+Au interactions at a center of mass energy of 130 GeV, measured in summer 2000. This is the first such data produced at RHIC. The analysis presented here focuses upon the measurement of balance functions, which are new observables in the field of heavy ion physics. The balance function for heavy ion physics is introduced in Bass, Danielewicz, and Pratt, Phys. Rev. Lett. **85**, 2689 (2000). The data were taken with the STAR (Solenoidal Tracker At RHIC) detector, with analysis performed on charged particles in a pseudorapidity region of $|\eta| < 1.3$.

The balance function measured for conserving charge/anti-charge pion pairs as a function of rapidity is predicted to have a width which indicates the time of hadronization of the measured particles. Charge/anti-charged particle pairs are created at the same point in space time, and are correlated in rapidity. Pairs which are created early have a wide separation in rapidity due to diffusion. However, pairs which are created late have a narrow separation in rapidity. Balance functions with a broad width show an early hadronization and are reflective of collisions which can be described as a superposition of nucleon-nucleon collisions. Balance functions which have a narrow width suggest late hadronization which is indicative of the formation of a QGP. In

addition to late hadronization, flow can narrow the balance function width even more than just the formation of QGP.

The balance function was measured for all charged particle pairs and pion pairs as a function of pseudorapidity, with respect to four centralities of collisions ranging from the most central to the peripheral. The balance function was also measured for pion pairs as a function of rapidity. For these measurements, it is found that the central events have a narrow balance function when compared to peripheral events, with a smooth variation in the intervening centralities. The HIJING simulated nucleon-nucleon interactions has a width consistent with that of the peripheral data balance functions, when the simulated events are processed through a STAR detector simulation. A Bjorken thermal model in the simulated STAR detector gives a pion pair balance function width which is wider than the central events (although narrower than peripheral). However the addition of flow narrows the Bjorken model balance function to that of the central data. The contribution of the acceptance of the detector was studied with various mixed events, pseudorapidity cuts, and with a different normalization method in the balance function calculation.

These measurements indicate that central events suggest late hadronization, which is consistent with Bjorken model predictions with the inclusion of additional radial flow. The balance function width of the peripheral collisions is consistent with model predictions incorporating a superposition of nucleon-nucleon scattering.

To Dr. Charles Banks Belt, Jr.

ACKNOWLEDGMENTS

Thanks go to a number of people, most of all to Wayne Tonjes, PhD for support and editing. Hugs to family and friends who put up with thesis-writing and data-analysis related silence and moods.

Professionally, I'd like to thank Dr. Michael Cherney for setting me on the path to research relativistic heavy ion physics. Thanks to Professors Gary Westfall and Scott Pratt for many enlightening discussions. Many thanks go to the Department of Energy and the National Science Foundation for providing funding to allow this type of exciting and innovative research to happen.

Although the work I did on the ElectroMagnetic Calorimeter did not make it into this dissertation, there is a part of me in those optical fibers. I hope the Calorimeter brings us interesting data for years to come.

Thanks to Apple computer for OSX, the iPod, and the G4. These were indispensable for fast data analysis, and carrying my thesis text and music to keep me happy.

King of Swamp Castle "Someday, all this will all be yours."

Prince Herbert "What, the curtains?"

Monty Python and the Holy Grail

CONTENTS

LIST OF TABLES

LIST OF FIGURES

Abbreviations & Definitions

ADC Analog to Digital Converter

AGS Alternating Gradient Synchrotron

BNL Brookhaven National Laboratory

BRAHMS Broad RAnge Hadron Magnetic Spectrometers experiment at (RHIC)

CERN European Organization for Nuclear Research

charged particle pairs For this dissertation, charged particle pairs refers to measurement without identified electrons unless otherwise stated.

CMOS Complementary Metal Oxide Semiconductor, integrated circuit

CTB Central Trigger Barrel, a detector in STAR

D variable used to measure charge fluctuations

DAQ Data AQuisition

dE/dx Energy loss per length. Usually keV/cm, used for PID in the STAR TPC

DST Data Storage Tape (can be real tape or a data storage file)

μ**DST** size and information reduced data storage file

EMC ElectroMagnetic Calorimeter, a detector in STAR

eta The pseudorapidity, η, defined as η = - ln tan $\theta/2$, where $p_z = |\mathbf{p}| \cos\theta$. For a massless particle, pseudorapidity $\approx$ rapidity.

ExB Electric field cross Magnetic field, in this case for corrections of interactions in the STAR TPC

FTPC Forward TPC, detector in STAR

GEANT A system of detector description and simulation tools to help physicists in high energy experiment design and studies

GSTAR framework to run STAR detector simulations using GEANT

HBT Hanbury-Brown-Twiss, a method of interferometry to determine source size

HIJING Heavy Ion Jet INteraction Generator

HIJING-GEANT in this dissertation, refers to HIJING simulated events which have been processed through GSTAR and TRS

L3 Level 3 trigger used in STAR (found in logbook notes, Appendix Table A.2)

minbias Minimum bias trigger (from logbook notes, Appendix Table A.2)

P00hi production library version of STAR 2000 data

P00hm production library version of STAR 2000 data (contains ExB corrections)

P10 Gas of 90% Argon, 10% methane, in the STAR TPC

PHENIX Pioneering High ENergy Ion eXperiment (at RHIC)

PHOBOS Experiment at RHIC

PID Particle IDentification

pQCD Perturbative QCD

Primvtx % of events with primary vertex (from logbook notes, Appendix Table A.2)

PYTHIA Program for the generation of high-energy physics events

QCD Quantum ChromoDynamics, model to describe the strong nuclear interaction

QGP Quark-Gluon Plasma

rapidity Defined as $y = -\frac{1}{2} \ln \frac{E+p_z}{E-p_z}$, also $y = -\tanh^{-1} \beta_z$

RICH Ring Imaging Cherenkov Hodoscope (in STAR)

RHIC Relativistic Heavy Ion Collider

ROOT An Object-Oriented Data Analysis Framework

RQMD Relativistic Quantum Chromo-Dynamics (heavy ion interaction simulator)

SPS Super Proton Synchrotron (at CERN)

STAR Solenoidal Tracker At RHIC, experiment

SVT Silicon Vertex Tracker (in STAR)

TPC Time Projection Chamber (in STAR)

TRS TPC Response Simulator (STAR software)

UNIX Operating system

ZDC Zero Degree Calorimeter (detector common to RHIC experiments)

Chapter 1

Introduction

1.1 Quark Gluon Plasma

It is thought that with sufficiently high energy density and temperature, a new phase of matter could be formed known as the quark-gluon plasma (QGP) [1]. During formation of this QGP, the quarks and gluons are liberated within this plasma. QGP is theorized to have existed in the early universe, before a phase transition from QGP to hadronic matter occurred at ~ 10 μs after the Big Bang. The nuclear phase diagram is shown in Figure 1.1 [2]. The nuclear liquid-gas phase transition has been studied in nuclear physics, however the transition to QGP is just beginning to be studied and understood in the field of relativistic heavy ion physics.

The search for QGP is not only important in the formation of new matter, but also to prove or disprove theories of fundamental particle interaction. The theory of interactions of particles with the strong force is known as Quantum ChromoDynamics (QCD) [3]. QCD is a complex and difficult theory which will not be described here, as more details can be found in reference [3]. QCD predictions are usually made in the perturbative regime, where the terms are calculable. The ground state of QCD, the vacuum, is still not understood [4], and by producing and studying QGP, more can be learned about the vacuum.

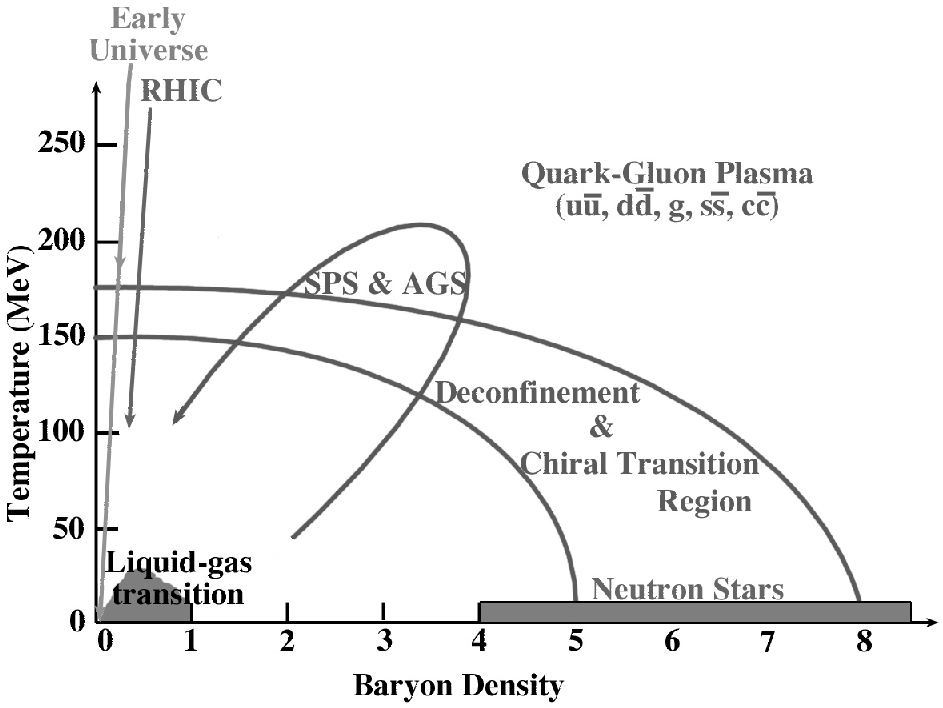

Figure 1.1: Illustration of different phases of nuclear matter, the x-axis is the Baryon density relative to normal nuclear matter (ρ/ρ_0), and on the y-axis is temperature (in MeV).

In 2000, physicists at the CERN(European Organization for Nuclear Research) SPS(Super Proton Synchrotron) announced that they had observed evidence for the formation of QGP [5] - [25]. Combining the measurements of several different SPS experiments they claim that there is evidence for a new state of matter in which quarks and gluons are deconfined. This evidence includes J/Ψ suppression, strangeness enhancement, as well as other observables. CERN studied lead ions colliding on lead at beam energies of 40 to 160 GeV per nucleon.

In a summary of QGP theory and measurements, S. Bass (reference [26]) states that "the SPS experiments have created a new state of high energy-density and temperature matter", and "the concept of a QGP needs to be rethought". It seems that both the SPS results and the early results from the RHIC collider (RHIC is discussed in Section 1.2) have given the theory of QGP a challenge with a set of observations to explain.

1.2 Relativistic Heavy Ion Collider

The Relativistic Heavy Ion Collider was built to search for the QGP and to study interactions of heavy nuclei and polarized protons at high energies. RHIC was built at Brookhaven National Laboratory in Long Island, New York, USA. An aerial photo of the collider is shown in Figure 1.2.

The two 2.4 mile (3.86 km) circumference beamlines cross at six interaction points. At four of the interaction regions are experiments which are designed to detect the particles resulting from the collisions at the interaction points. The two physically larger experiments are STAR and PHENIX. The two smaller experiments are PHOBOS and BRAHMS. Each is located as shown in Figure 1.3. RHIC is also designed to provide interactions of polarized protons to study the fundamental nature of the spin content of protons, as well as to create p+p reference collisions for the heavy ion program. This dissertation will focus upon Au+Au collisions detected in the STAR

Figure 1.2: View of Brookhaven lab from the air showing the RHIC ring (largest circle) [27].

experiment.

1.3 STAR

STAR is the Solenoidal Tracker At RHIC [28]. It is a large detector with multiple components designed to search for signatures of QGP and study the behavior of matter which interacts at a high energy density. STAR is designed to measure many interesting observables simultaneously, both over many events and on an event-by-event basis. The design of STAR will allow for measurement of variables which indicate entropy, temperature, and strangeness chemical potential for collisions. Particle fluctuations and collective motion of particles and energy (flow) can also be measured. STAR is designed to measure high transverse momentum processes above 2 GeV/c as well. The features of STAR are described in more detail in Chapter 2. STAR measurements performed at RHIC at the time of this writing are published in references [29]- [35].

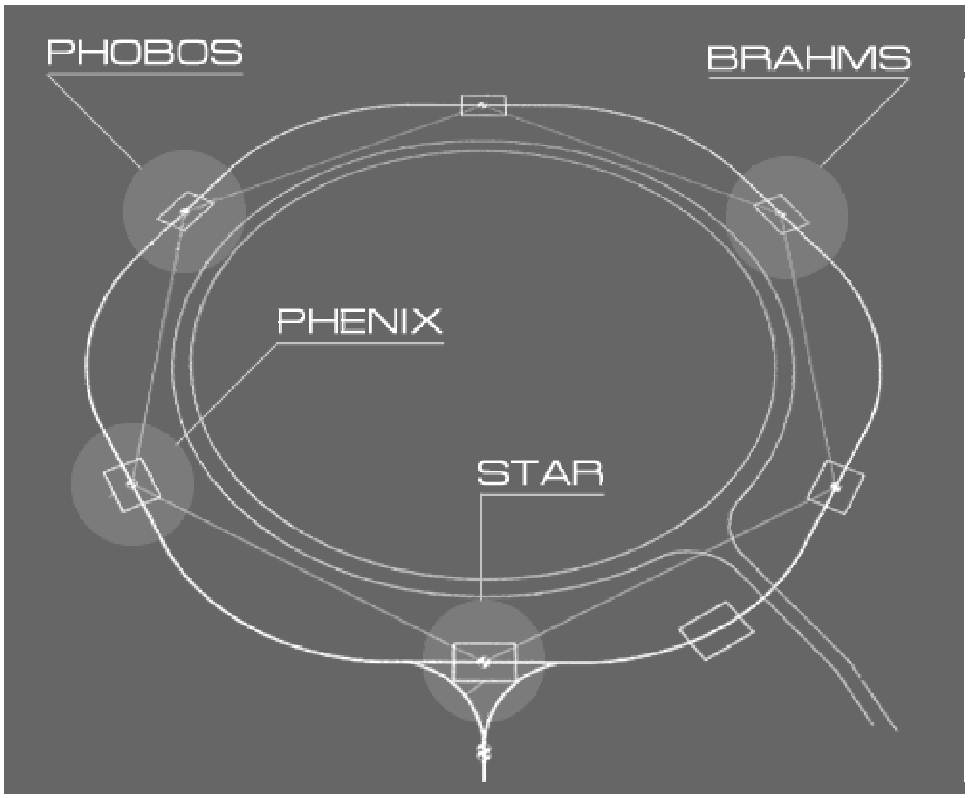

Figure 1.3: Schematic of the RHIC ring, showing the six interaction regions and the placement of the four experiments [36].

Chapter 2

STAR in Year 2000

The data used in this analysis was taken in the summer of 2000, during which RHIC collided Au+Au ions at a center of mass energy of $\sqrt{s_{NN}}$=130 GeV. The collisions were below the collider's design energy, but still gave the opportunity to measure heavy ion collisions at a higher interaction density and energy combination than previously studied. The main detector used for particle tracking in the summer 2000 data taking run was the Time Projection Chamber(TPC). The Ring Imaging Cherenkov Hodoscope (RICH) detector, and a section of the Silicon Vertex Tracker (SVT) were installed in STAR at the time, but the data analyzed in this dissertation is from the TPC only. Trigger detectors installed and used were the Zero Degree Calorimeters (ZDCs), and the Central Trigger Barrel (CTB). Also used was a solenoidal magnet. An illustration of the STAR setup for year 2000 is shown in Figure 2.1.

2.1 Magnet

The STAR solenoidal magnet is essential for the identification and tracking of charged particles. The magnet is designed to give a uniform field parallel to the direction of the beam. The magnet structure also contains the main subdetectors of STAR, the TPC, CTB, RICH, and eventually the ElectroMagnetic Calorimeter (EMC). The

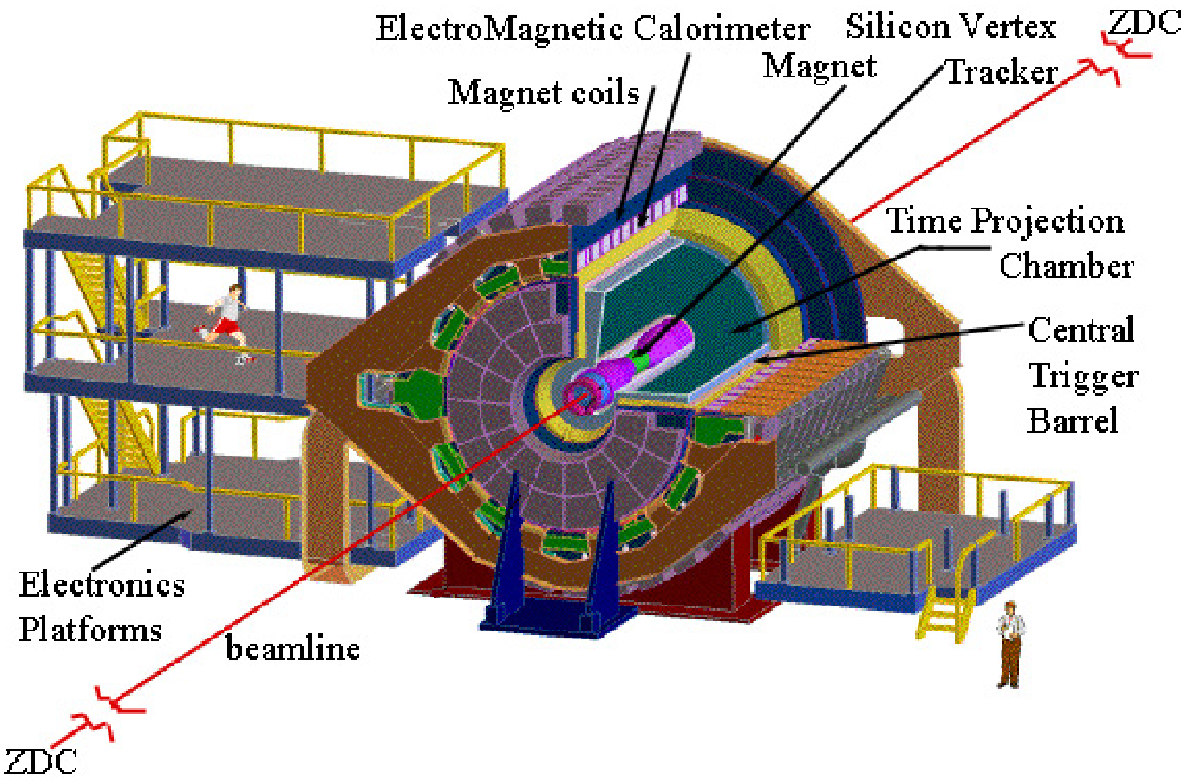

Figure 2.1: Illustration of the STAR detector, pointing out detectors installed for the year 2000 summer collisions, excluding the RICH. ZDC stands for Zero Degree Calorimeter. [28].

EMC is still being installed in stages for use in 2001 and beyond. The magnet can be operated at a field strength up to 0.5 Tesla, however for the year 2000 run, the magnet was operated at $B_z = 0.25$ T. The magnetic field was mapped before the installation of the TPC, with a precision of 1-2 Gauss for all dimensional components of the field [37]. The uniform field along the beamline of the magnet eases the tracking pattern recognition in analysis, as a simple helix model can be used for particle tracks.

2.2 The Time Projection Chamber

The main sub-detector in STAR is the TPC. The TPC is designed to measure many of the basic physics observables in RHIC's heavy ion collisions. This detector covers a total pseudorapidity range of $-2.0 < \eta < 2.0$, as well as a full 2π of the azimuthal direction. The pseudorapidity is defined as $\eta = -\ln\tan(\theta/2)$, where θ is the angle radially from the beamline direction, z. With a magnetic field of 0.25 T, particles can be measured with $p_t \geq 50$ MeV/c. The TPC covers a tracking volume with a length of 4.2 meters, an inner radius of 0.5 meters, and extending to 2 meters outer radius. The TPC uses time slices of signals to achieve a three dimensional image of the charged particle tracks which pass through the detector. An illustration of the TPC is shown in Figure 2.2 [28].

The TPC contains a gas which is a mixture of 90% Ar and 10% methane (P10). This gas was chosen due to several properties, including negligible attenuation of the drifting electrons, a reasonable drift velocity, a high efficiency for dE/dx, and operation at atmospheric pressure. The two endcaps of the TPC each contain 12 sectors, each sector having an inner and outer radius module. Each of these sector modules has wire planes in front of a cathode plane, creating a pad segmentation. The pads are arranged in concentric rows to maximize the detection of high transverse momentum tracks. The central membrane, which can be seen in Figure 2.2, is a cathode operated at high voltage at the center of the TPC. The inner and outer field

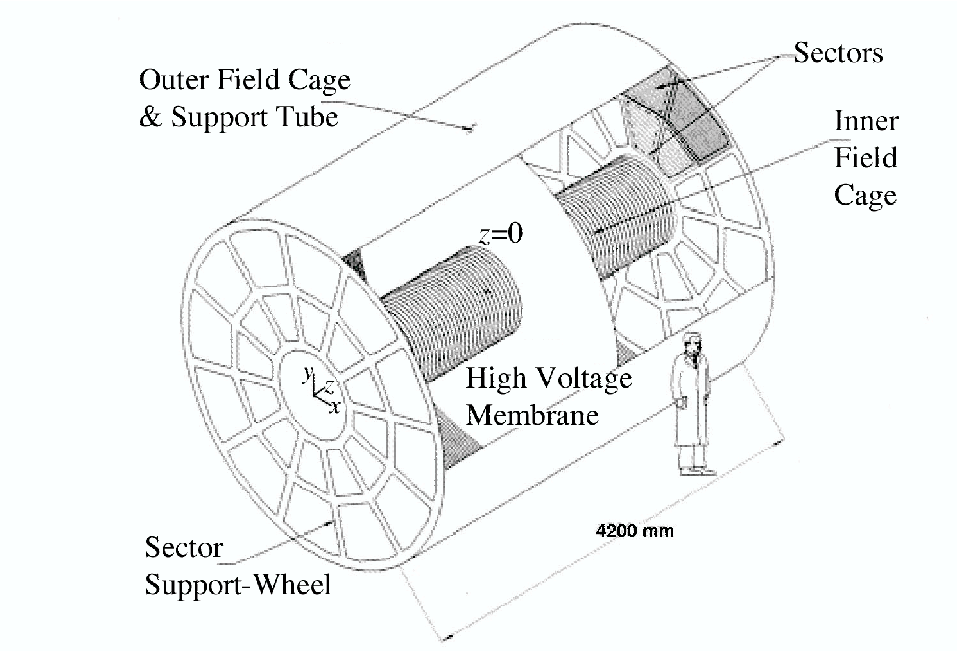

Figure 2.2: Schematic of the STAR Time Projection Chamber [28].

cages constrain the electric potential as well as providing containment for the P10 gas. The inner radius of the TPC is at 0.5 m, designed with the expectation that in full luminosity RHIC Au+Au events, the track density would be too high to resolve individual tracks at smaller radii.

A charged particle which enters the TPC will ionize the P10 gas. The electrons formed along the particle's track will then drift towards an endcap due to the electric potential created between the central membrane and the endcaps. The drift velocity of the electrons in the TPC was measured to be 5.44 ± 0.01 cm/μs with the variation of drift velocity being over a number of days. For the summer 2000 data run, the position resolution in the z direction was ≈ 500 μm. Figure 2.2 shows the direction convention used in STAR, that is z is along the beamline, and x and y are on the plane radially outward from the beamline. The field strength near the anode wires in front of the cathode planes is similar to that of a cylindrical capacitor. Thus, electrons that have drifted to the pad plane would gain kinetic energy from this electric field, which ionizes the gas near the wire. This creates an electron avalanche that is detected

on the anode wire. The anode's pulse is amplified with custom CMOS circuits [37]. Figure 2.3 shows a cross section of the pad wire geometry. There is a third layer of wires, the gating grid, before the cathode (or shield plane) and anode. The gating grid wires remove field distortions from the extra ions formed around the anode wires, yet allows the signal electrons through to be detected. The gating grid may also be controlled to clean the pad plane area between triggers. To maintain a signal to noise ratio of 20:1 for the pads including both the small outer sector and large inner sector pads, the anode voltages were set to a gain of 1100 (3000) in the outer (inner) sector.

The longest drift time in the TPC is 40 μs. The electrons reaching the pads are read in by 512 channels, reading each time slice at 100 ns per channel. The position of the particle which created the detected electron signal (the hit) is converted from time to position given the known drift velocity. The position resolution in the radial direction depends on the size of the pad planes which detected the particle. A schematic of the pad plane layout is given in Figure 2.4. The outer sector has 3,940 pads, with each pad having a radial size of 19.5 mm and an azimuthal size of 6.2 mm. The inner sector contains 1,750 pads, with a pad size of 11.5 mm radially and 2.85 mm azimuthally. The outer radius of the tracking volume constrains the pseudorapidity coverage of the TPC to $|\eta| < 1$, and the inner radius covers $|\eta| < 2$. The useful tracking volume extends out to about $|\eta| < 1.5$, because a track requires at least 10 pad row hits to be reconstructed as a good track. More about tracking will be covered in Section 2.6.

The TPC is designed to be effective at measuring charged particle tracks at both high and low multiplicities for RHIC collisions. The TPC has worked well in both calibration and data taking runs as well as laser calibration tests. For more details on the STAR TPC, see references [28], [38], [39] and [40].

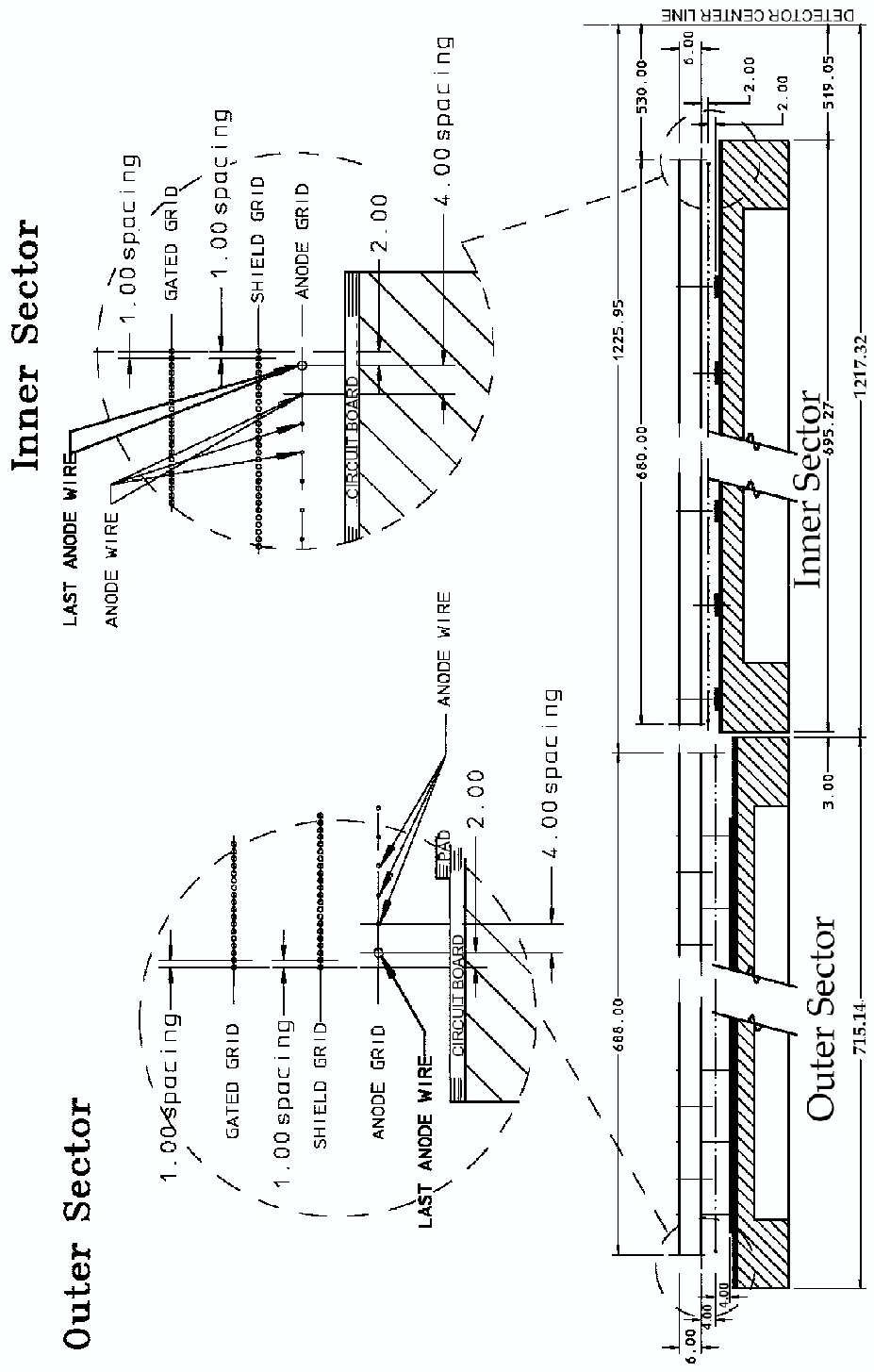

Figure 2.3: Side view of the inner and outer sector of the TPC pad plane showing the wire geometry, with all measurements in mm [37].

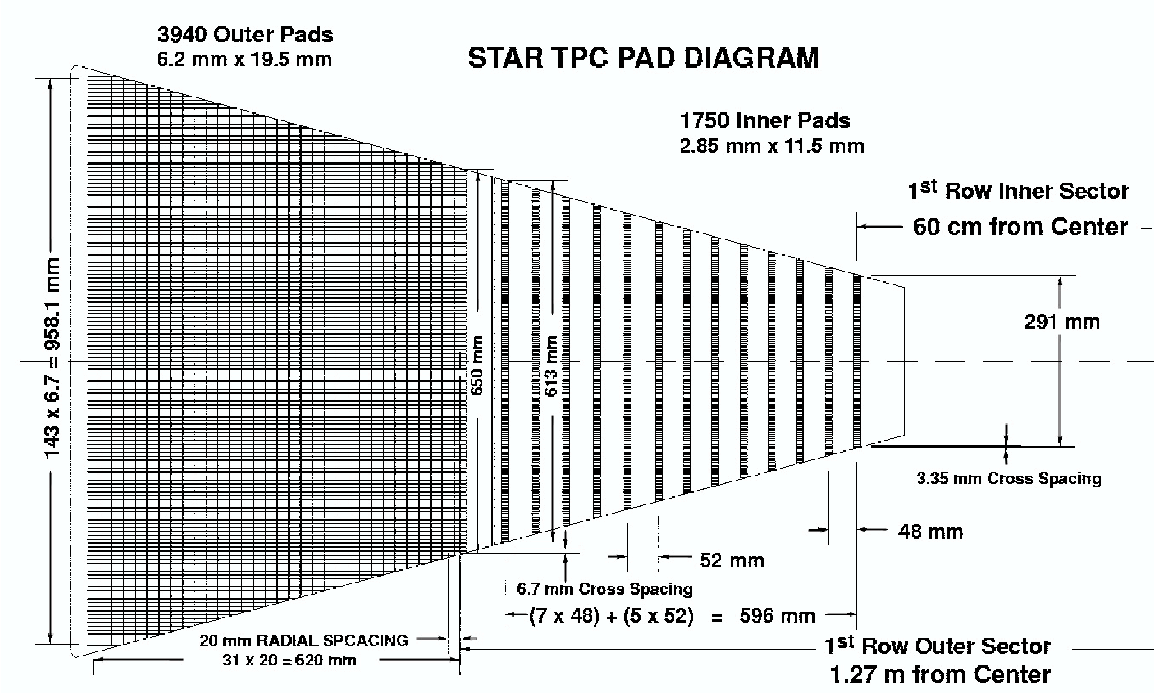

Figure 2.4: Schematic of a TPC sector with inner and outer pads [37].

2.3 The Trigger

The two trigger systems used in summer 2000 were the Zero Degree Calorimeters (ZDCs) [41], and the Central Trigger Barrel (CTB). The ZDCs are hadronic calorimeters located $\pm$ 18.25 m from the center of STAR along the beamline. All four of the RHIC experiments have similar systems. The CTB is a cylinder of scintillator slats surrounding the TPC covering a pseudorapidity region of $|\eta| < 1.0$. The CTB measures charged particle multiplicity with a 2π azimuthal coverage for every RHIC crossing. These detectors were designed to operate at a luminosity of 2×10^{26} cm^{-2} s^{-1} for Au+Au collisions at $\sqrt{s_{NN}}$ = 200 GeV, as well as for polarized p+p collisions at 500 GeV with a luminosity of 2×10^{32} cm^{-2} s^{-1}. RHIC is designed to operate with 117 bunches in each of the two rings, with a time between bunch crossings of $\simeq$ 105 ns [37]. The STAR TPC can record data at a rate of 4 events/second which as the slowest detector, limits the amount of data taken. To choose which collisions contain useful physics information, the ZDCs are used to measure the spectator neutrons

emerging from a collision. If there are signals in coincidence above threshold in the ZDCs, then a minimum bias event has occurred. The data set with this trigger is labeled as minimum bias for any sort of collision event of gold nuclei, whether the gold ions hit each other peripherally or hit head-on (centrally). Using the CTB, the efficiency of the coincidence ZDC trigger was found to be above 99% for the whole range of multiplicities used in this dissertation [37]. A trigger for interesting central events uses the ZDC signal together with a CTB signal above threshold. The central trigger events use the highest 15% CTB signals. Central events are those in which the ions have collided head-on. In a central collision, a large number of particles are produced, many of them transverse to the beam direction. More about STAR triggers can be found in [28] and [42].

2.4 Centrality

There are a number of different types of collisions, from those that are the most peripheral where the nuclei glance off of each other, to central collisions where the nuclei hit head-on. To compare these different classes of collisions, an observable is necessary to define centrality. In heavy ion collisions, the number of particles measured gives a good estimate of the centrality of the collision, and thus, the impact parameter. In Figure 2.5, the centrality definitions used in this analysis are shown. The number of tracks are primary tracks measured in the complete TPC for the minimum bias triggered data. Primary tracks are those which reconstruct back towards the primary collision vertex. The integral of the normalized curve to a specific bin gives the percentage of centrality. The top 10% of the integrated histogram represents the most central events, referred to hereafter as the central data set. The next 30% of centrality are the midcentral events. The next 30% are the midperipheral events, leaving the last 26% as peripheral events. The most peripheral events, those with 5 tracks or less, were omitted as there are indications that these were non-hadronic

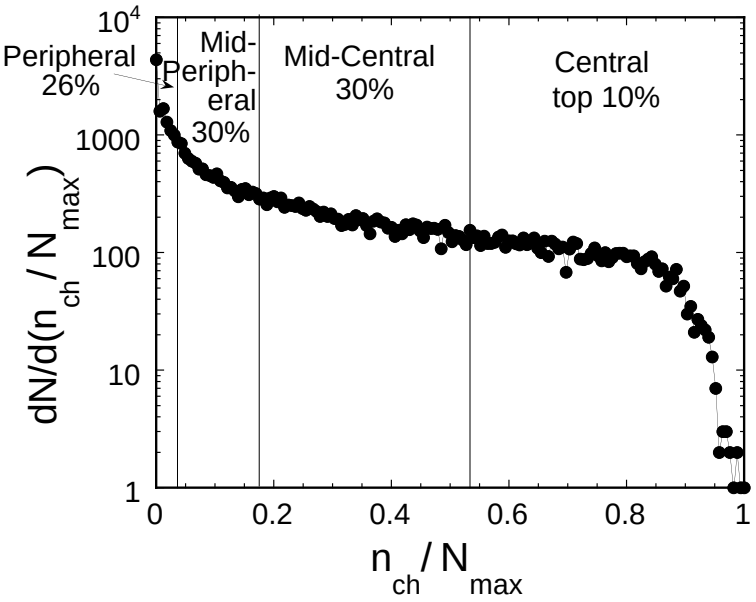

Figure 2.5: Minimum bias year 2000 STAR events with four centrality bins labeled.

events [43]. The events used had a reconstructed collision vertex, and the tracks used for centrality were primary tracks which point back to that vertex. This technique also reduces the number of beam-gas collisions in the peripheral data set. The events which were used in the balance function measurements also had at least two charged particle primary tracks within the TPC track cuts (Section 2.6.)

2.5 Event Cuts

During the year 2000 data taking, the RHIC collision region was as large as the TPC in the z direction. Collisions which had an event vertex within 75 cm of the center of the TPC in the z direction are chosen in this analysis. A track which would normally extend over the whole length of the TPC in a vertex(z) = 0 collision might not be fully detected in a vertex(z) = 100 cm collision. This partial detection of larger vertex(z) collisions can be seen in Figures 2.6 and 2.7, which show 2 of 10 possible vertex bins. Figure 2.6 shows the pseudorapidity distribution for the farthest negative vertex bin, which is centered around 62.5 cm. In contrast, Figure 2.7 shows the pseudorapidity

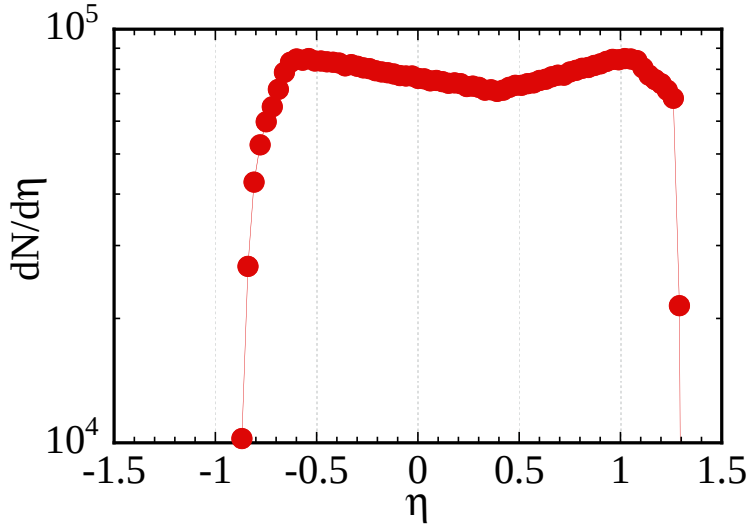

Figure 2.6: Pseudorapidity histogram for central events in the -62.5 cm vertex bin.

(dN/$d\eta$) distribution for central trigger events which have a vertex centered around zero, in the most central vertex bin. The edges of the TPC along with the track cuts (discussed in Section 2.6) are visible as sharp drops in the pseudorapidity distribution. Events which had an x or y position of the vertex more than 1 cm from the center of the TPC were not analyzed, providing the least amount of variation in ϕ given the TPC resolution.

The distribution of vertices used in events analyzed from the year 2000 data is

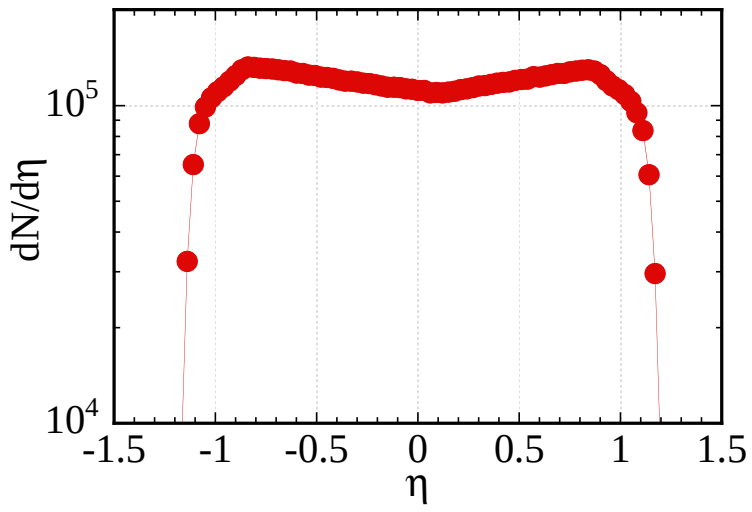

Figure 2.7: Pseudorapidity histogram for central events in the 0 cm vertex bin.

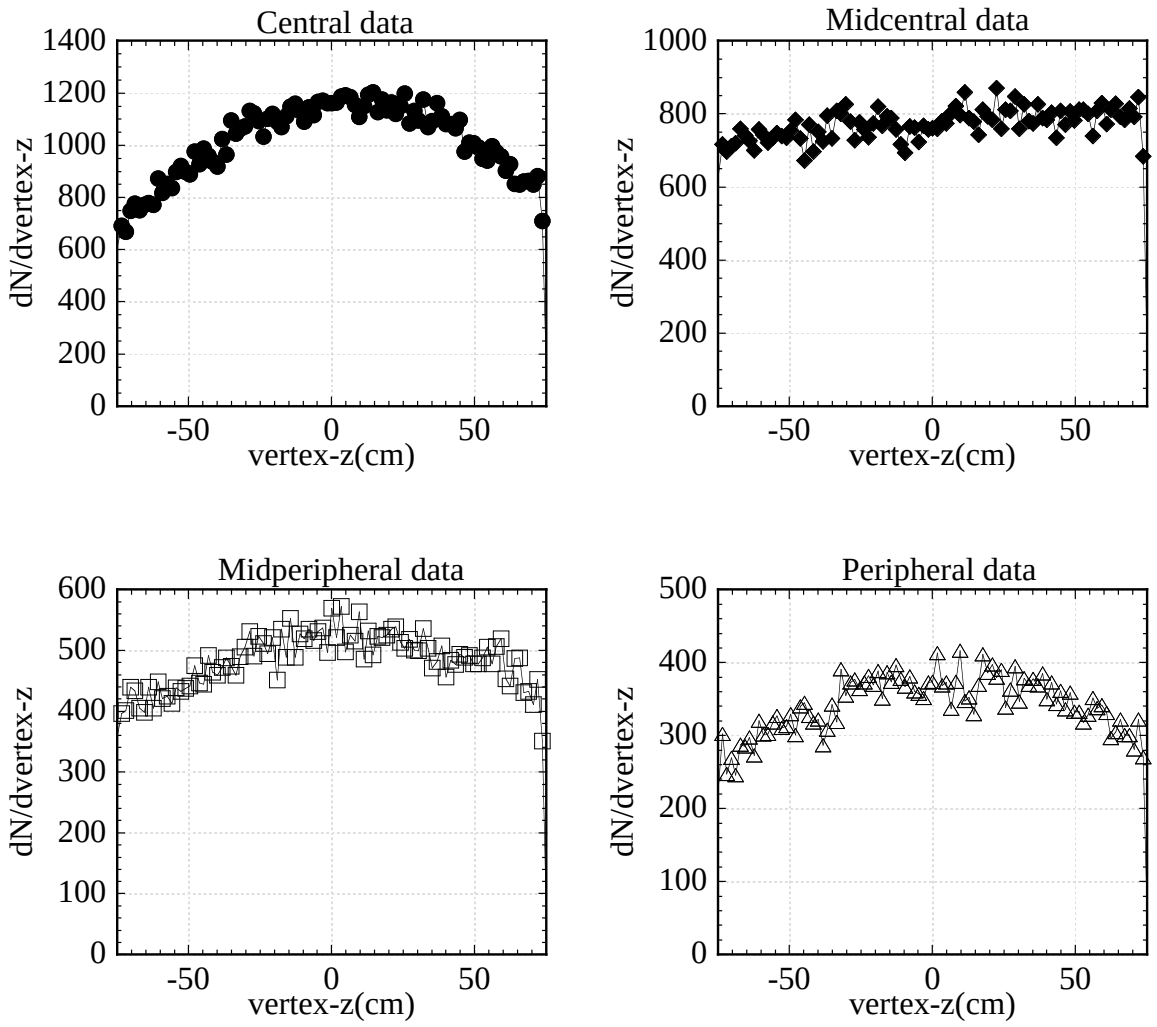

Figure 2.8: Vertex distribution for year 2000 events used in the analysis, all four centralities are shown.

shown in Figure 2.8.

2.6 Track Cuts

The energy deposited from charged particles is detected as TPC ADC (Analog to Digital Converted) signals, giving a 3-dimensional picture of the collision. These signals are analyzed with a track fitting algorithm that finds the primary vertex of the collision and fits tracks based upon an expected helical geometry which point back towards the primary vertex. These tracks are known as primary tracks. Global tracks

are all tracks that are found in the detector. In the 2000 data, global tracks are merely TPC tracks, but in later data runs, they will include other installed and instrumented detectors such as the EMC and SVT.

For the balance function analysis, the particles that contain the signal are those which come directly from the primary vertex of the collision. Thus, only primary tracks are used in the analysis. The initial check of the quality of the track for data analysis is the flag variable, which is greater than zero for good tracks. All tracks used in the analysis must be primary tracks which are labeled as good tracks. There are other measurements which are used to label the tracks which are appropriate for data analysis use. These measurements, using cuts to remove unusable tracks, are based upon studies of various track cuts by the STAR collaboration. The cuts used here were chosen for the analysis in the first STAR publication studying flow [29], and similar track cuts have been used in many STAR analyses. References [32], [33], and [37] discuss effects of different cuts.

Tracks are used which have a pseudorapidity measured within $|\eta| < 1.3$. Theories of QGP identification require the measurement of variables over at least two units of rapidity [44]. The limit of pseudorapidity was chosen to strike a balance between maximizing statistics and minimizing systematic error from the detector. Smaller pseudorapidity regions were explored for balance function analysis, as covered in Section 7.2. Another condition is that tracks must have at least 15 hit points used in the fit. To eliminate double counting, the ratio of fit points to the possible number of points must be greater than 0.52. This reduces the possibility of having a single track labeled as two separate tracks (track splitting), and then being counted twice. The tracks are limited to a momentum of $0.1 < p < 2$ GeV/c. The distance of closest approach (dca) between the track and the collision vertex can be calculated, and tracks are used which have a $|\text{dca}| < 1\text{cm}$. The dca cut reduces most of the background that comes from tracks which are the product of secondary decays. These conditions assure

that the tracks used in the analysis have a detection efficiency of 85% ± 5%. However, there is an estimated 5% of the particles which are electrons from narrow decays which happen to point back to the collision vertex. Once a particle track survives all these tracks cuts, it can be used in balance function analysis.

2.7 Particle Identification

For a balance function measured with all charged particle pairs, some particle identification is needed to remove the secondary electron contamination from the primary particle signal. The necessity for removing these electrons is discussed in Section 5.2. When the balance function is constructed with pion pairs, particle identification is needed to separate the pions in the events from the other particles. Particle identification is done using the measured energy loss of the tracks as the particles leave the TPC. The energy loss values for each hit on a track are used with a truncated mean method to reduce fluctuations. The $\mathrm{dE}/\mathrm{d}x$, mean energy loss per unit length, for each primary track in a selection of minimum bias events is shown plotted versus momentum in Figure 2.9. The lines on this logarithmic plot are a calculation of the expected Bethe-Bloch parameterization for electrons (the line almost parallel to the x-axis), pions (the leftmost line), kaons (the next line), and protons (the far right line). The events shown were not included in the final analysis due to problems with the trigger, however, the particle types and momenta are consistent with the data taken in year 2000.

Tracks within events which pass the quality cuts were first compared to the expected energy loss for pions. The expected $\mathrm{dE}/\mathrm{d}x$ for a pion is calculated with the momentum of the tracks. The number of σ the track is from the perfect Bethe-Bloch particle can be found with the measured mean $\mathrm{dE}/\mathrm{d}x$ and momentum as shown in

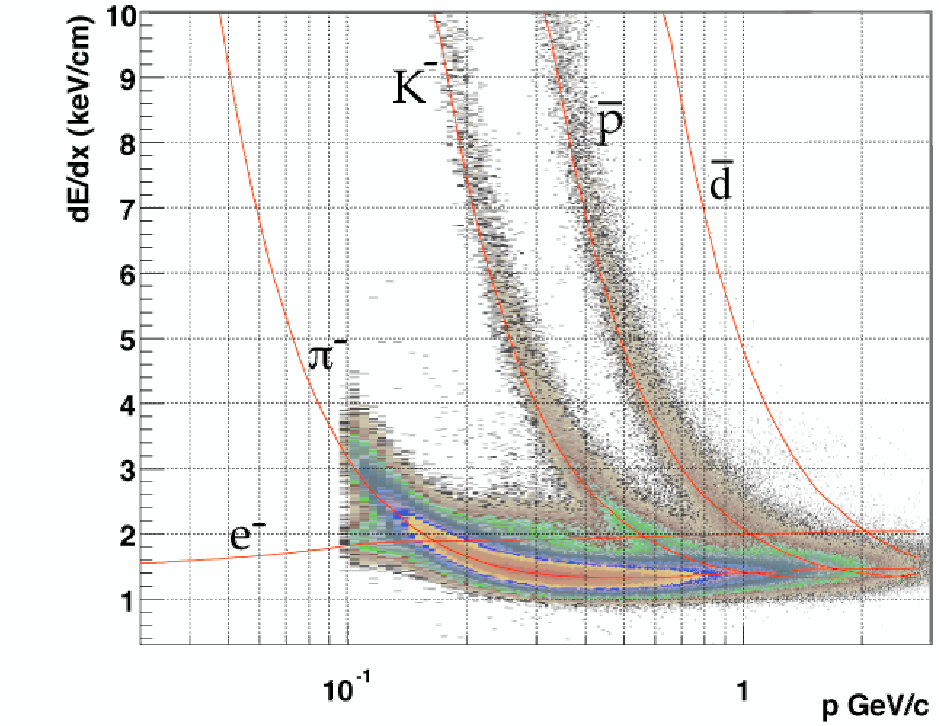

Figure 2.9: dE/dx vs. momentum for negative charged particles identified as primary in the TPC for July data. The lines drawn through represent the predicted dE/dx from the Bethe-Bloch equation for different particles as labeled. The different shades represent density of tracks, with the highest density being in the center of the pion region, and the lowest on the edges of the proton region.

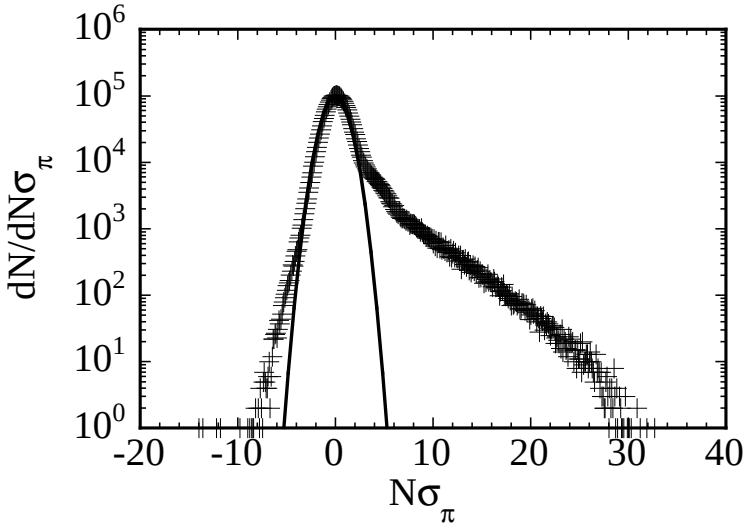

Figure 2.10: The Nσ_π values for all negative particles passing track cuts in minimum bias run 1248015. The Gaussian fit marks the pion signal.

Equation 2.1.

$$\begin{aligned} Z_\pi &\equiv \ln \frac{\text{mean dE/d}x}{\text{expected dE/d}x(\pi)}, \\ N\sigma_\pi &\equiv \frac{Z_\pi}{\text{dE/d}x \text{ resolution}}. \end{aligned} \tag{2.1}$$

For the other particles, the π is replaced by K, p, or e for each case respectively. In this method, the number of sigma a track is from any of these four particles can be used for particle identification. The profile of Nσ_π for all negative particles in one minimum bias run (~22,000 events) is shown in Figure 2.10. The shoulder to the left of the Gaussian curve is probably electrons. The Gaussian shows the pion range, and to the right are kaons and protons. When the events are analyzed, the track is first compared with the pion ionization. If the track is within 2σ of the expected result, i.e. if $|\text{N}\sigma_\pi| < 2$, then the particle is tagged as a pion.

In Figure 2.9, it can be seen that the dE/dx signal for pions and kaons begins to mix at a momentum greater than 0.7 GeV/c. Thus, the particle is kept with the pion tag only if its momentum is less than or equal to 0.7 GeV/c, and its ionization is within

2σ of the calibrated ionization for a pion. Particles which do not fit those qualifications are then checked against the expected ionization for kaons. The kaon and proton signals in the dE/dx vs. momentum space begin to mix at 0.8 GeV/c. Thus, particles that have not been tagged as pions, have $p \leq 0.8$ GeV/c, and $|\mathrm{N}\sigma_{\mathrm{K}}| < 0.2$ are tagged as kaons. From the remainder of the tracks, protons are tagged for those whose momentum is less than or equal to 1 GeV/c to avoid mixing in deuterons and $|\mathrm{N}\sigma_{\mathrm{p}}| < 0.2$. The untagged particles which are left are identified as electrons if they fall within 2σ of the electron Bethe-Bloch curve. The remainder particles are labeled as unidentified particles. All particles are kept for the different types of analyses. There is an estimated 1% contamination of secondary electrons within the pion signal, however, the pions compromise the majority of detected particles within a heavy ion collision. The effect of secondary electrons is strongest at small changes in rapidity (or pseudorapidity), as discussed in Section 5.1. The resolution of the dE/dx measurement is estimated to be about 10% [37].

2.8 Physical Characteristics of a Track

Each track is recorded in the STAR TPC as a series of hits in three dimensions. A track fitting algorithm is used together with the magnetic field information and the particle hits. In future data taking, STAR will use information for track reconstruction from all detectors, not just the TPC. However the track data used in this analysis is from the TPC only. The track fitter used was based upon the expectation that every particle track would be a section of a helix. The track fitting routine was developed and tested by STAR collaborators. The track fitting uses the specifics of the track helix such as the curvature, starting point, azimuthal angle of the track direction at the starting point, and the fit of a circle in the xy plane with the value of the magnetic field in the z direction to calculate information about the geometry of the particle's path. The curvature of the track in the magnetic field gives a measurement of the

momentum of the track in three dimensions. The direction of the curvature of the particle's track gives the charge of the particle. The pseudorapidity of the track can be found from the momentum vectors [45] [46]. Once a track is tagged as a primary track with a good fit and the track passes the track cuts described in Section 2.6, the necessary information for balance function analysis is written to file. The file creation and analysis structure is discussed in Chapter 4.

Chapter 3

The Balance Function

3.1 Definition

The balance function is an observable proposed by Bass, Danielewicz, and Pratt [47] to indicate the hadronization time of particles that emerge from a heavy ion collision. While there are many standard observables used to probe the interactions of nuclei at high energies, the balance function is new to the field of heavy ion physics. In p+p collisions, the charge density balance was measured [48] in a functional form similar to the balance function. The measurement of the width of the charge density balance for selected particles in a four jet structure was used to determine that jet fragmentation is universal. The associated charge density was used in e^+e^- collisions for the study of strangeness correlations [49] and baryon correlations [50].

In Au+Au collisions, the balance function can be used to clock particle hadronization. The time of hadronization could be an indicator of the type of collision that occurred. It is theorized that at a high enough energy and density, a quark-gluon plasma (QGP) will be formed [4]. This QGP will exist for a finite amount of time before it cools off, hadronizing into pions and other particles. The particles detected in a relativistic heavy ion experiment can be studied to determine features of the source that created them. There are many observables that can be measured which

differentiate a QGP from a hadron gas [51]. The particles which hadronize from a QGP are theorized to be created at a later time, since the QGP exists for a short time with quarks and gluons existing without being bound into separate hadrons. Thus, having an observable which indicates the time of hadronic particle creation would give a glimpse into the nature of the source that created those particles.

To understand how the balance function measures time, consider the relativistic heavy ion collision just after it occurs, as seen schematically in Figure 3.1. For a QGP, the long cylinder of material stretched out between the two receding ions maintains its quark deconfinement for a short time before hadronization [52]. When hadronization occurs, the particles and their partner anti-particles are produced at the same space/time point from quark/anti-quark pairs. At hadronization is when the fractional charge carried by the quarks is combined into unit charge in particle$^+$/anti-particle$^-$ pairs. These particles do maintain a collective motion, or flow, which can be measured [29]. However, because hadronization occurs some time after the collision, the final state interactions of the produced particles have a smaller cross section than if they are formed earlier. The particles would emerge with a small spread in rapidity between particle and its partner anti-particle. In contrast, if a hadronic gas is created instantly, the particle/anti-particle pairs are created very early in the collision, right after the ions collide. These particles have much opportunity to interact with other particles in the cylinder, as the system is pulled apart while the beam ions recede. Thus, the particle pairs which are created from the hadron gas can have a large spread in rapidity.

The next apparent challenge is to identify the particle/anti-particle pairs which were created together. When particles are identified in the detector, there is no identification tag to label which particle pairs with a specific anti-particle. Thus a statistical method must be used. The balance function is constructed to identify pairs on a statistical basis and provide a measure of the rapidity spread of particle/anti-particle

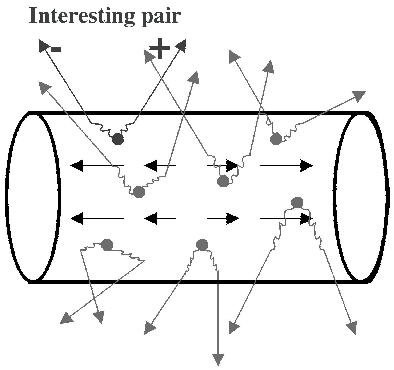

Figure 3.1: A schematic of the collision during hadronization. Arrows to the left and right represent the spreading of matter. Arrows emerging from the dots represent particle pairs created together. The jagged lines represent the interactions of those particles in the medium.

pairs. The balance function in its most general form [47] is:

$$\begin{aligned} B(p_1|p_2) &= \frac{1}{2}\left[\rho(b,p_2|a,p_1) - \rho(b,p_2|b,p_1) + \rho(a,p_2|b,p_1) - \rho(a,p_2|a,p_1)\right], \\ \rho(b,p_2|a,p_1) &= \frac{N(b,p_2|a,p_1)}{N(a,p_1)}. \end{aligned} \tag{3.1}$$

$\rho(b,p_2|a,p_1)$ is the conditional probability of observing a particle of type b in bin p_2 given the existence of a particle of type a in bin p_1. Thus, if bin p_1 refers to a particle measured in the right half of a detector, then bin p_2 could refer to a particle measured in a smaller subset of the right half of a detector such as one-fourth of that. These conditional probabilities would then be measured over all possible sub-bins of the detector. The balance function can be used to consider not only the balance of charged particle pairs and pion pairs, but also for any quantity which is conserved, such as strangeness which is measured in the balance function for kaons or baryon number with proton pairs. However, this thesis will concentrate upon the charged particle pair and pion pair balance function measurements. The form of the balance function used in this dissertation is:

$$B(\Delta y) = \frac{1}{2 * \text{binsize}} \left\{ \frac{N_{+-}(\Delta y) - N_{++}(\Delta y)}{N_+} + \frac{N_{-+}(\Delta y) - N_{--}(\Delta y)}{N_-} \right\}, \quad (3.2)$$

$$y = rapidity = -\frac{1}{2} \ln \frac{E + p_z}{E - p_z}, \quad (3.3)$$

if mass of particle is small, $y \approx \eta$.

$N_{+-}(\Delta y)$ is the histogram of $|y(\pi^+) - y(\pi^-)|$ for all possible pairs within an individual event. This histogram is summed over all measured collision events. $N_+(N_-)$ refers to all the positive(negative) particles used in the pairing. It is possible to construct a balance function with all possible charged particle pairs instead of pion pairs, except the argument of B would be $\Delta\eta$ instead of Δy. The binsize is included so that the balance function measured in a perfect detector will normalize to one. Here, the summations over all possible pairs and then events are not given explicitly, but are done in the construction of a measurement from events in different Δy (or $\Delta\eta$) bins.

The individual terms of the balance function are calculated separately for each event, which classifies this measurement as an event-by-event observable. The form of the balance function pulls out the correlation in rapidity (or pseudorapidity) of a particle/anti-particle pair which has been formed together. The validity of this model can be demonstrated with a simple simulation. A Bjorken thermal simulation code was obtained from Pratt [47] which can test that this statistical summing method works to accurately reconstruct the given input. This simulator first produces a particle with a random 4-momentum, and then an anti-particle with another random 4-momentum. For a given amount of time, particles are moved forward along straight-line trajectories and given a random chance weighted by the number of particles at elastically scattering within a given time. This is followed by more straight-line trajectories and scattering until a final time. Then both particles are spread by the same

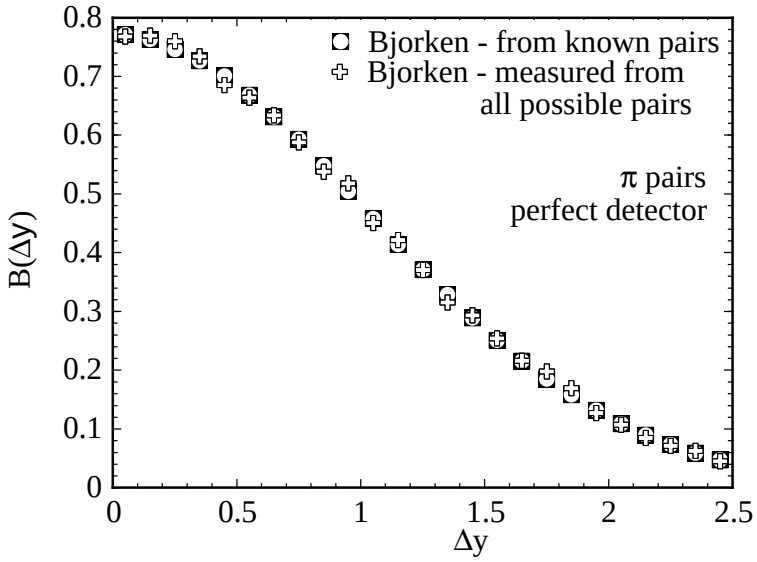

Figure 3.2: The shape of the balance function plotted for a perfect detector. Plusses are from the statistical measure, whereas squares with circles are from known balancing pairs.

random rapidity. The simulated particles are written to a separate file in a format containing particle identification, momentum, transverse momentum, and pseudorapidity (to mimic the real datastream). However, as the particles are written to file, the difference in rapidity between the co-created particle pairs can also be written to file, in a histogram which normalizes to one over all possible Δy. The comparison between these two methods is shown in Figure 3.2. The default settings of the Bjorken thermal model were used, with a bin width of 0.1, initial temperature of 225 MeV, final temperature of 120 MeV, with temperature for hadronization of 165 MeV, and a formation time of 9 fm/c. The rapidity spread is ± 2 and there are an average of 3 collisions per particle in this simulation.

3.2 Predictions

The comparison of known balancing pairs to a statistical measurement of the balance function shows visually that the balance function does indeed reconstruct the rapidity difference between co-created particle/anti-particle pairs. In reference [47],

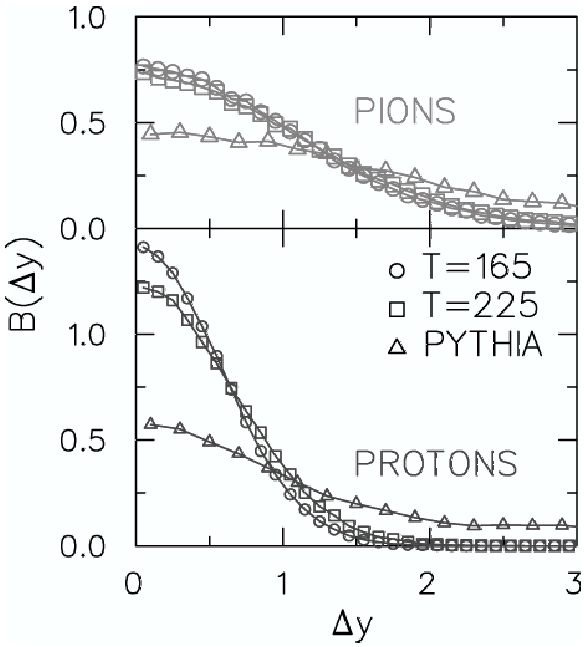

Figure 3.3: Balance functions for pions (top) and protons (bottom) calculated with respect to Δy. Bjorken thermal model simulations of a QGP are in circles and squares. PYTHIA p+p collisions (representing the hadron gas model) are shown in triangles [47].

Bass, Danielewicz, and Pratt not only describe the construction and theory of the balance function, but make predictions for balance function measurement. Figure 3.3-top shows the balance function measured in a perfect detector for a Bjorken thermal model (circles and squares), and PYTHIA p+p events (triangles). PYTHIA [53] is a model used to simulates p+p events at $\sqrt{s_{NN}}$ =200 GeV, which represents the hadron gas scenario. PYTHIA models hadronic reactions for p+p collisions as well as hadron-nucleus and nucleus-nucleus collisions [54]. PYTHIA uses the Lund string fragmentation model, and its specific predictions have been confirmed by experimental measurement [53]. The Bjorken thermal model [47], [52] is the same as the one described above in Section 3.1 without the rapidity spread, which creates an expanding pion gas after a given time at a specified temperature.

It is evident from Figure 3.3 that the Bjorken model has a narrower balance function than the PYTHIA model. The width of the balance function can be understood as

$\sigma^2_{\Delta y} = 2(\sigma^2_{\text{thermal}} + \sigma^2_{\text{diffusion}})$. The thermal term refers to the thermal rapidity spreading due to the collective behavior of particles after the collision. The diffusion term represents the rescattering of particles within the medium. Rescattering of particles would broaden the balance function by diffusing the charge/anti-charge pairs in space, or rather rapidity. Considering the discussion in Section 3.1, a QGP model would have a smaller time to diffuse, so that term in the width could approach zero. This diffusion term would be affected by whether the created charge moved as a free quark in a QGP or a as hadron in its early history. Annihilations of particles could also broaden the balance function, although reference [47] predicts that the balance function for a QGP would still remain narrower than that of a hadron gas. The predictions in reference [47] do not cover the issues of resonance decays such as $\rho^0 \rightarrow \pi^+\pi^-$ and the effects of experimental acceptance on the balance function. To understand the effects of having a real detector as opposed to a 'perfect' detector, simulations can be used.

To summarize the predictions, the balance function measured from a QGP would exhibit a narrow shape in comparison to the balance function from a hadron gas from the superposition of nucleon-nucleon collisions. For small rapidity differences, the broader hadron gas model is expected to have a lower initial balance function than that of a QGP. However, experimental and model dependent factors which influence the shape of the balance function require understanding. The relative time of particle hadronization may be qualitatively found by measuring the balance function.

Chapter 4

Analysis Method

4.1 Software

Data from the TPC are collected by electronics and analyzed in the first step by the STAR analysis software. The STAR analysis system is based upon ROOT, a C++ based physics graphing and data analysis package developed at the CERN laboratory. Collaborators developed software to read this TPC information, with a framework that allows for many types of data analysis. The TPC information was analyzed and track reconstruction was performed in production stage. The production was run with two different libraries, which include the calibrations of the TPC, as well as all the track-fitting and reconstruction software. Production libraries will be discussed in Section 4.1.1.

At the time the analysis in this dissertation was performed, the ROOT input/output procedure was time-consuming, as a separate file would need to be opened for each Data AcQuisition (DAQ) file, or about every 500 events. Thus, the necessary particle information for the balance function calculation was output to a binary file. This method created what is referred to as a micro Data Storage Tape (μDST), a smaller data set created from the total track information on file.

The data set was written out with a header file and a data file. The header file

contains the information related to each particular event, the STAR run number, the STAR event number, and the local analysis event number for that run. Each event was checked to see if it was within the event quality cuts described in Section 2.5, and events which were acceptable had the local event number indexed. Two integers were also written to the header file that contained the number of tracks. The first integer contains the number of good primary tracks in the TPC. This is the total number of tracks detected which have the track flag > 0. The track flag is a variable which is set negative if the track reconstruction routine finds something wrong with the track. This first number of tracks variable is the one that is used for a centrality cut, as it covers all the primary tracks detected by the TPC. The next integer contains the number of accepted tracks which are written to the data file. These are the tracks which pass the track quality cuts for the balance function calculation.

The data file which is written out contains the passed event number, the passed track amount, and the needed data for each track. For the P00hi library analysis, this was the particle ID (PID), the mean $\mathrm{dE/d}x$ value in keV/cm of the track, the magnitude of the momentum (GeV/c), the transverse momentum(GeV/c), and the pseudorapidity of the track. For the P00hm library analysis, the mean $\mathrm{dE/d}x$ variable was replaced by the number of σ the $\mathrm{dE/d}x$ was from different particle models. The different particle models considered were electron, pion, kaon, and proton. In each case, the particle identification was performed as discussed in Section 2.7, and a PID was written out, with the sign of the PID integer being the charge of the particle. The PIDs were assigned as follows in Table 4.1.

The data files were written out with one binary header and one binary data file per data-taking run. This allowed for simple quality cuts later, when specific runs were found to contain faulty data, the good and bad runs are tabulated in Appendix A in Tables A.1 and A.2. The binary data format allowed for simple, quick, repetitive analysis with compiled C++ programs on any computer platform. It also allows

particle	|PID|
electron	1
pion	2
kaon	3
proton	4
unknown	11

Table 4.1: Particle and absolute value of PID (particle identification) codes used in balance function analysis.

for simple data backup and eliminates dependence on computers at Brookhaven lab through the network.

4.1.1 STAR to Local Data Conversion

To convert the data from STAR reconstruction files to a local DST, analysis modules were written. For the P00hi production data, a module was created using the example of M. Calderon's μDST PionTree maker [37]. This system created a file with ROOT tree structures that contained the accepted track data. The accepted tracks and event information were then written to text files which were transferred over the network and then translated to binary. During each step of the data sort and transfer, histograms of the variables written were compared to assure that accuracy and information was not lost. Histograms were created in ROOT directly from the production. Comparative and analysis histograms were created locally through a C++ program and plotted in KaleidaGraph. Specific variables were also written out during testing with event identification to give a specific numeric check.

The same procedure was done for the P00hm production data. However, the data translation from the STAR ROOT files to binary files was done with a simpler program than for P00hi which was based upon a template program, StAnalysis Maker [55]. Data from concurrent runs in both P00hi and P00hm were analyzed with the balance function program to assure that the results did not change with respect to the different production libraries. The charged particle balance function for the same set of events

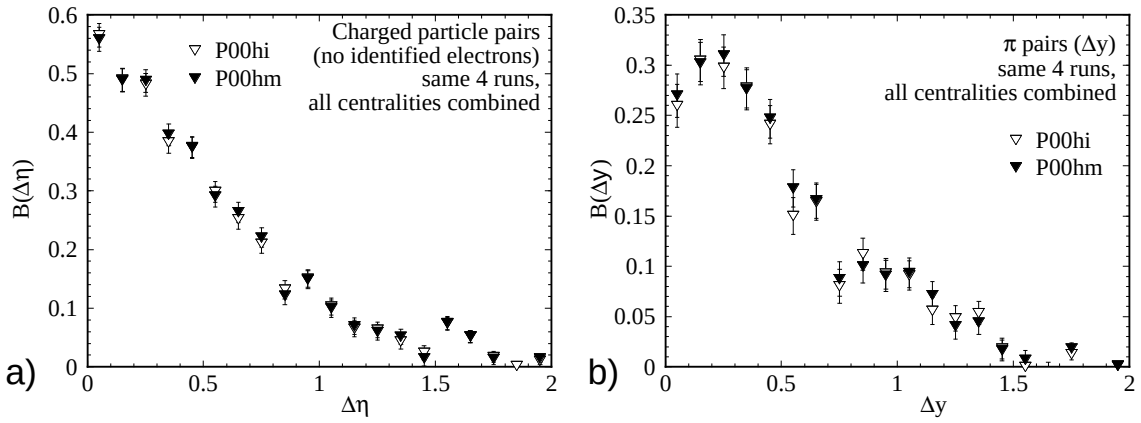

Figure 4.1: a) Charged particle pair and b) pion pair balance functions measured for runs 1243059, 1245006, 1245012, and 1246009. Open triangles are P00hi production library, and closed triangles are P00hm.

analyzed in P00hi and P00hm is shown in Figure 4.1. The shape and structure of the balance function will be discussed later in Chapter 5. What is important is that the production both with (P00hm) and without (P00hi) the electric and magnetic field correction produce the same result within statistical error bars for the balance function.

4.1.2 Local Data Analysis

The binary files were analyzed with two programs, balance.cp and balanceout.cp. Both programs were written for use on Macintosh and UNIX platforms. The balance.cp program analyzed each run separately, calculating the N_{+-} & N_{+}-type terms. These terms were then written to a text file, with a separate file for each particle-centrality combination. The balanceout.cp program would take a specified set of runs and sum the balance function terms over those runs, calculate the balance function, the error, the integral, and the weighted average of the balance function. All these variables calculated would be output to a file in a format readable by KaleidaGraph.

4.2 Data Quality

4.2.1 Logbook Information

The quality of the data used was checked with a variety of methods. One of the simplest ones to start with was the fact that the data had been written to file in a STAR production. This meant that the computer tags on the files used would be labeled Physics runs, with either central or minimum bias trigger. Logbook information is also useful for quality, and for STAR this was kept online. During data taking shifts, the information about the magnetic field, actual trigger parameters used, and any other important information about the run was entered into the online run log. This run log can be browsed by a STAR collaborator over the internet, allowing for access of data logbook information at any time. As the summer 2000 data was the first physics data that STAR recorded, the information for event quality was scattered in a number of sources. These sources included the online run log, E-mails to the Quality Assurance team, and the STAR software team E-mails [55]. Runs such as 1228031, 1240008, and 1246017, were all labeled as Physics data runs, however, the online run log information showed that the trigger used was a laser trigger. The laser trigger is used for TPC calibration. A STAR collaborator warned the collaboration of troublesome runs which were taken on August 15th, 2000. These were runs where the trigger had lost contact with the RHIC clock, and thus had possibly mistimed collisions. If the timing is off, it is possible to record an event which includes pieces of two overlapping events. The TPC track momentum and pseudorapidity would look normal, but the multiplicity in the TPC would give an inaccurate representation of the centrality of the collision. Collisions which were recorded with a ultra-peripheral trigger were also not used in the analysis, as the trigger that was implemented in summer 2000 for ultra-peripheral collisions was biased as it was optimized for two track events [56]. Also, when the logbook had runs tagged as being trigger tests, they

were not used for similar reasons. Also, the data from the trigger detectors, ZDC and CTB were checked during the program which converted data from ROOT files to simple binary files.

Run log information included many details. One type of note found in the log for particular runs was regarding TPC sector failures. A few times during data taking, parts of the TPC would fail and require startup. Any run which had this tag on it, as well as runs close in time would not be used in the balance function analysis. This type of analysis depends on measuring the conserved charge emerging from the collision in all directions, given the detector's known efficiency. With a missing TPC sector, a piece of the detector is missing which changes the coverage of what is measured. Events from runs which are missing TPC sectors could be used in other types of data analyses, but were not used in the balance function analysis. There were a few data runs where the magnet was off or experienced a failure during or just before that run. The magnet needed to be operational during the run, as the calibration and reconstruction depend on having tracks which curve in the magnetic field. Runs were omitted in which the magnet was off, or had tripped during the run.

In addition to particular run quality, the software used in track reconstruction was checked for accuracy. Members of the collaboration used GEANT-created tracks embedded into real data events to check software library reconstruction accuracy as well as the TPC particle detection efficiency. This work is reported in detail in [37]. There were two software libraries used in this analysis, P00hi and P00hm. P00hi was the first stable production library used in data analysis. It was shown to give correct reconstruction and a high reconstruction efficiency for tracks studied. This production library included all the necessary TPC calibrations and reconstruction software, with which the end-user would merely need to read the reconstructed event data from a file and have most variables needed for most analyses. The P00hm software library was an upgrade of the P00hi library.

The change which has the greatest possibility to affect data analysis is the addition of an ExB field correction. This correction is implemented to add the correction for the slight misorientation of the electric and magnetic fields to the parallel of the beamline and to each other. A three dimensional map of the TPC's magnetic field was made. The deviations of the magnetic field from parallel together with the electric field can create an additional force which changes the expected motion of charged particles away from the primary vertex. As the tracks are reconstructed based upon their expected behavior in the TPC, the electromagnetic fields would need to be known precisely. Some runs that were analyzed in the P00hi software library were analyzed using P00hm, and many runs not analyzed in P00hi were analyzed in P00hm. The balance function measurement for the two libraries was compared, and there was no change seen in the P00hm upgrade, as seen in Figure 4.1. Runs used in the final analysis included those analyzed by both P00hi and P00hm STAR software libraries.

Another piece of information is the runs which were analyzed in production. The offline reconstruction (production) of the data would perform simple quality checks. It was found that there were runs analyzed in the P00hi library that were not reconstructed in P00hm due to quality. A final check was communication with other colleagues analyzing the same data. In this way, runs were found which showed trouble with the triggering, which can allow multiple events to overlap. In summary, the Appendix A Table A.1 shows some logbook information for runs which were used in the analysis in this dissertation. Appendix A Table A.2 shows the logbook information for both P00hi and P00hm data runs which were omitted for reasons given in the last column of that table.

4.2.2 Amount of Data

A total of 244,718 events from the year 2000 passed the event quality cuts, 150,756 minimum bias events, and 102,173 of central events. Table 4.2 shows the amount of

centrality	amount	trigger
central	79,844	central
midcentral	25,656	central
midperipheral	897	central
peripheral	581	central
central	15,360	minimum bias
midcentral	46,655	minimum bias
midperipheral	44,267	minimum bias
peripheral	31,458	minimum bias

Table 4.2: Amount of events used in analysis for each of the four centralities from central trigger (top), and minimum bias trigger (bottom).

events for each of the four centralities for the two different triggers.

These are sufficient statistics to perform a charged particle balance function measurement. With the majority of the particles detected in an event being pions, this also means that a pion balance function may be constructed. However, these statistics are too low to measure the balance function for kaons and protons. As is discussed in reference [47], 10^5 events are necessary to have a clear signal considering the statistical error bars. The error bars will be discussed in Chapter 5.

4.2.3 Graphical Data Quality Check

The quality of the data was also checked graphically. A multiplicity plot was made for the combined set of minimum bias and central trigger events, as can be seen in Figure 4.2. Recalling the shape of the minimum bias multiplicity distribution from the discussion of centrality in Figure 2.5, it can be seen that there is a bump in the high multiplicity region. This bump corresponds to the central trigger events. By studying this multiplicity distribution on a run by run basis, the runs beginning with 1229 recorded on 8/16/2000 were found to contain data which appeared to be of a minimum bias trigger, although they were apparently recorded with a central trigger. This study was one aspect that led those runs to be removed from the final analysis.

The distributions for other variables used were also checked for each run. Figure 4.3

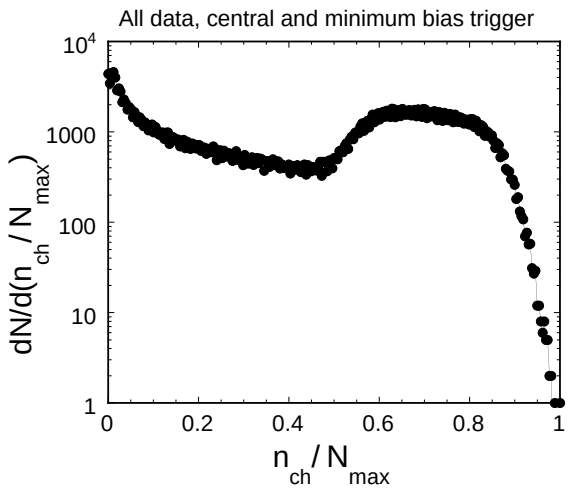

Figure 4.2: Multiplicity distribution for both triggers used for the data set analyzed here.

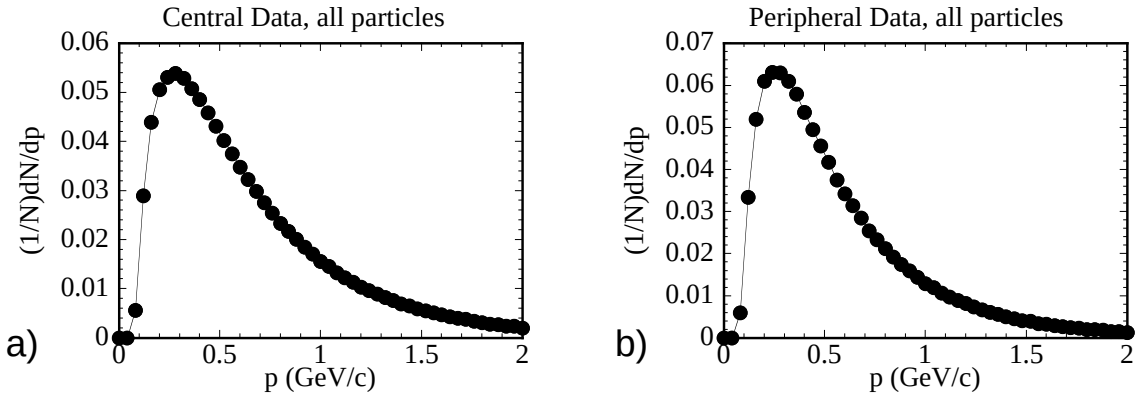

Figure 4.3: All charged particles normalized momentum distribution for a) central and b) peripheral events.

shows the momentum magnitude and pseudorapidity distributions for central events. The overall shape is typical of primary particles with the specific track cuts that were used, as detailed in Section 2.6.

At this scale, differences cannot be seen between centralities for the central and peripheral momentum distributions. Examining the pseudorapidity histograms, there appears to be a difference between centralities. However, it should be considered that there are different pseudorapidity distributions for the differing vertex bins. The dependence of pseudorapidity distributions on the vertex is shown in Section 2.5. Thus, the vertex distribution of the centrality cuts should be examined. Figure 4.4 shows

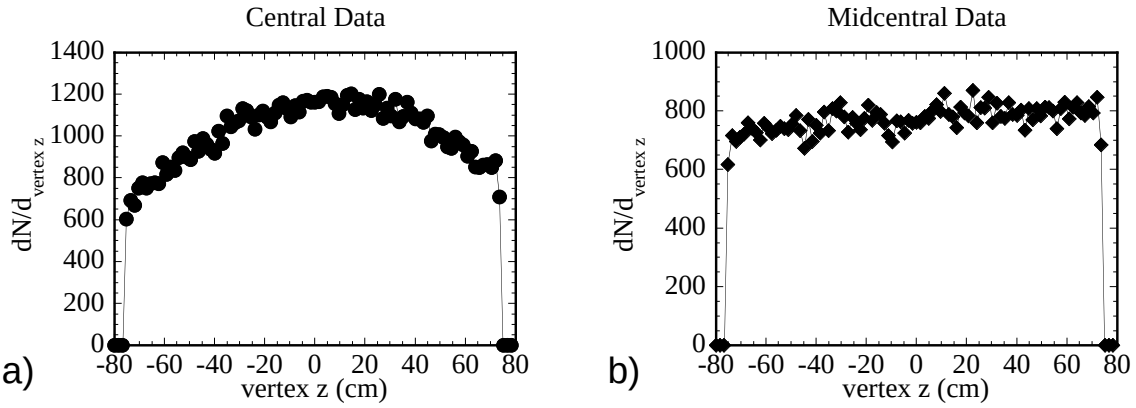

Figure 4.4: All charged particles non-normalized vertex distribution for a) central and b) midcentral events.

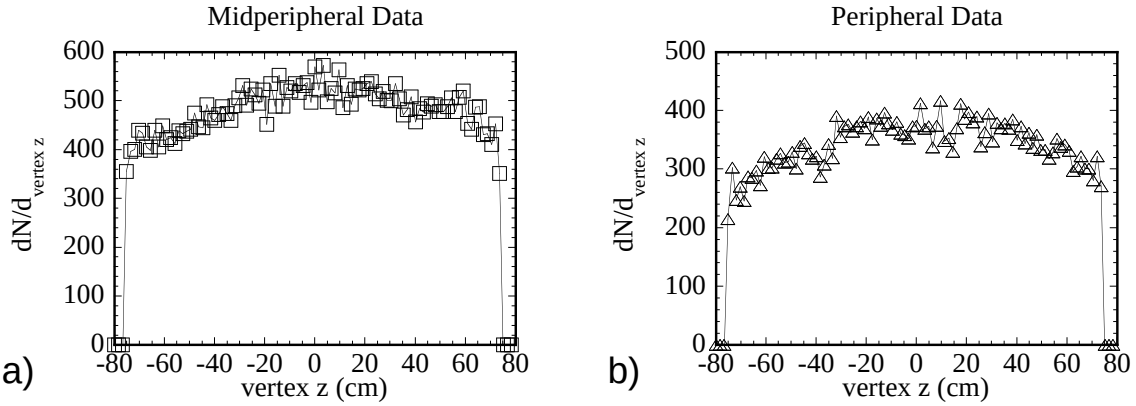

Figure 4.5: All charged particles non-normalized vertex distribution for a) midperipheral and b) peripheral events.

the non-normalized vertex distributions for central and midcentral events. Figure 4.5 shows the vertex distributions for midperipheral and peripheral events.

The dN/dη distributions for the four different centrality bins are shown in Figures 4.6 and 4.7. The differences in shape may be partly attributed to the differing vertex profiles for the different triggers. In general, these histograms may be used as a guideline to check validity of the data. The form of the rapidity distribution for the pions used in the balance function is also useful. Figure 4.8 shows both the pseudorapidity histogram for all charged particles again, with the rapidity histogram for pions beside for comparison. For the pions, the histograms have similar shape to the charged particle histograms, although the momentum cut does cut the momentum histogram

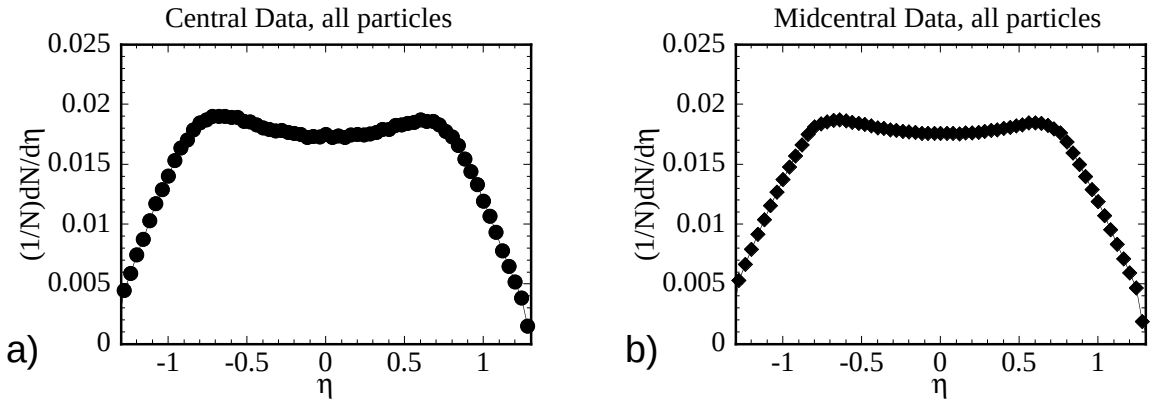

Figure 4.6: All charged particles normalized η distribution for a) central and b) midcentral events.

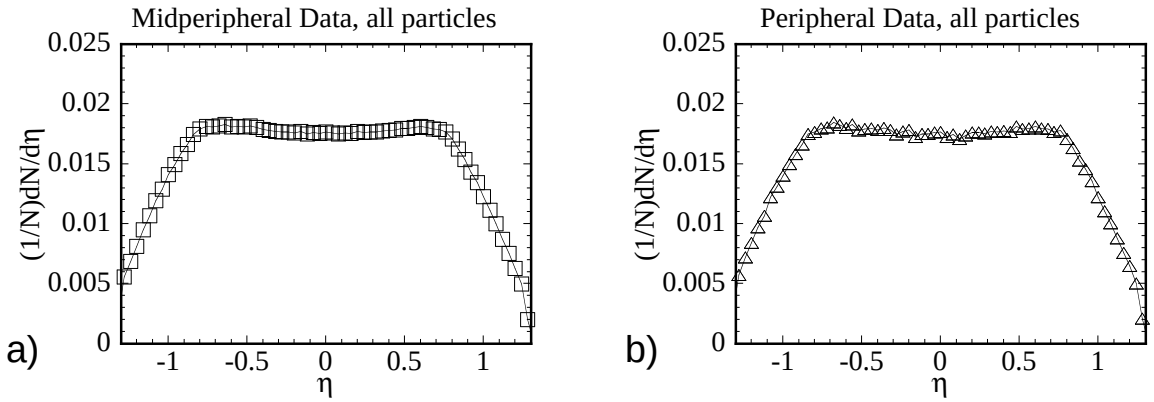

Figure 4.7: All charged particles normalized η distribution for a) midperipheral and b) peripheral events.

at a p of 0.7 GeV/c.

The plots shown are characteristic of the overall behavior of the data. Individual runs were examined to be certain that none of the variables deviated markedly from the data. Overall, the runs examined had reasonable plots. A large number of these plots were made during analysis, and most will not be reproduced here. The figures shown above do give a general sense of the typical shape for the data which is useful in qualitative comparison with simulations.

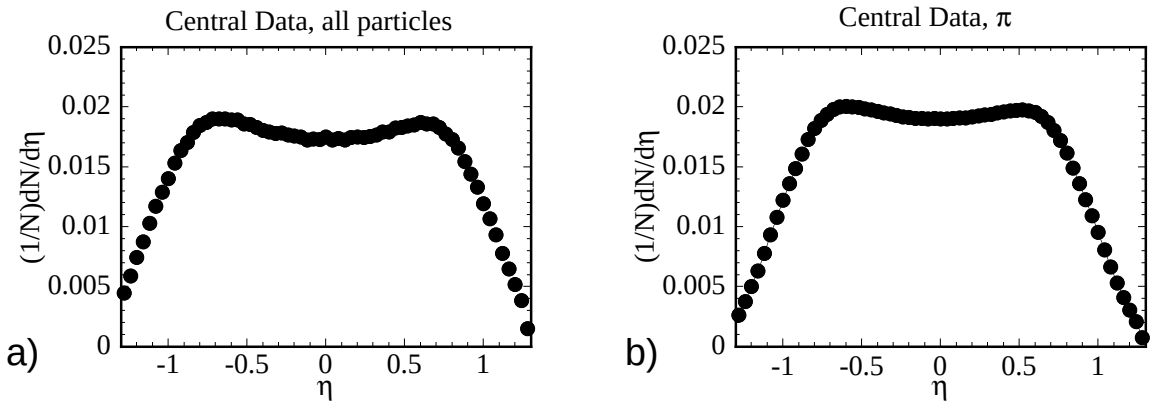

Figure 4.8: a) All charged particles normalized pseudorapidity distribution compared to b) pion pseudorapidity distribution.

4.2.4 Programming Quality Assurance

During the writing of the programs balance.cp and balanceout.cp, the programs and subroutines were checked for quality. In this case, quality meant that the calculations were accurate. One method used was to take a known small set of data, and ensure that the same balance function measurement was found calculated by the program and by hand. By hand usually included using a calculator or a simple analysis program to check the calculation steps.

4.2.5 Simulation Quality Assurance

Simulations of nucleon-nucleon heavy ion collisions were performed with the simulator HIJING, described in Section 6.1. HIJING stands for Heavy Ion Jet INteraction Generator [57]. HIJING was processed with the STAR GEANT framework, GSTAR, as well as the TPC Reconstruction Simulator (TRS), and then analyzed with the STAR reconstruction chain, treated as if the events were of real data. These simulations will be referred to as HIJING-GEANT. The GSTAR and TRS code was checked for quality by STAR collaboration members [58] [59] [60]. Appendix A Table A.3 shows the summary of HIJING-GEANT events which were used in this dissertation, the impact parameters and number of events.

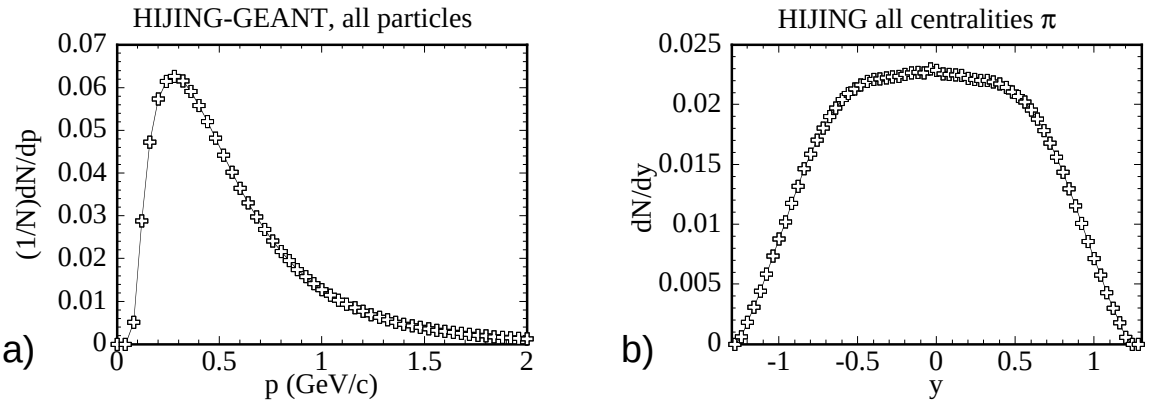

Figure 4.9: HIJING-GEANT normalized a) momentum distribution for all charged particles and b) rapidity distribution for pions.

Similar to the data quality check, histograms of variables such as p and η can show the quality of the HIJING-GEANT events. In particular, comparing these histograms to those of the data illustrate the effectiveness of the detector simulation as well as the underlying physics simulation. For HIJING-GEANT events, there is no centrality separation, as all impact parameters are expected to have the same balance function physics. This shall be examined further in Section 6.1.3. Figure 4.9 shows the momentum and rapidity distribution for HIJING-GEANT events, with the momentum shown for all charged particles, and pseudorapidity for pions. Both plots seem similar to the data, however the momentum distribution seems narrower at high momenta, and the rapidity distribution has a strange peak. Figure 4.10 shows the vertex and pseudorapidity distribution for these simulated events. The vertex distribution is nicely centered, unlike the data. The η distribution appears very similar to the data. Given these quality plots, it appears that there is nothing very wrong about the HIJING-GEANT simulations. However, the charged particle distributions are more similar in shape to the data than the pion distributions.

Nothing obviously wrong was found with the data sets or the simulations to be used in the balance function analysis. Any suspect data was removed, as described in the previous sections. The quality check proved to be useful, as a large slope change

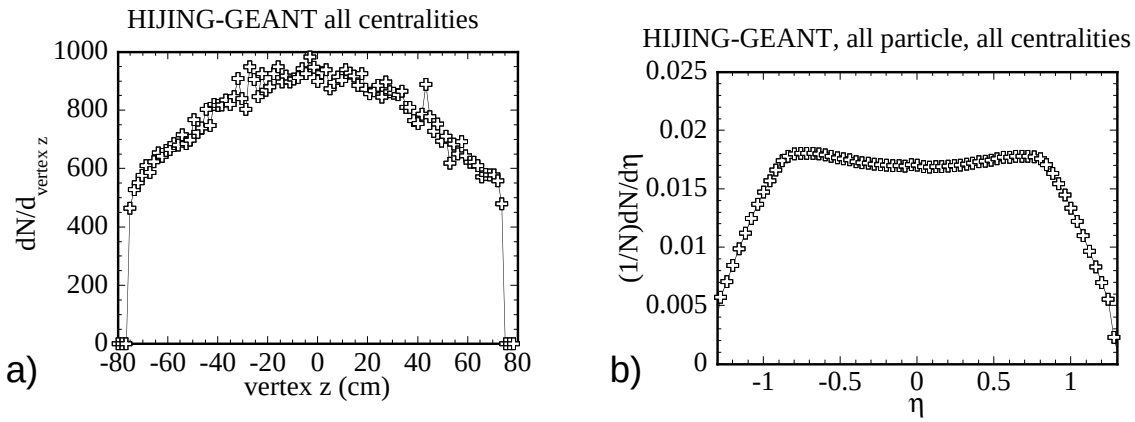

Figure 4.10: HIJING-GEANT a) non-normalized vertex distribution and b) normalized η distribution, both for charged particles.

was evident in the midperipheral balance function. Once the runs with faulty trigger were removed, the large slope change no longer appeared in the measured balance function. Removing suspect runs does decrease the statistics of data available for analysis, however it also ensures a cleaner data set with the same detector-dependent influence on the measurement.

Chapter 5

Data Balance Function Measurements

The balance function measurements shown in this chapter use the same form shown in Equation 3.2:

$$B(\Delta y) = \frac{1}{2 * \text{binsize}} \left\{ \frac{N_{+-}(\Delta y) - N_{++}(\Delta y)}{N_+} + \frac{N_{-+}(\Delta y) - N_{--}(\Delta y)}{N_-} \right\}, \quad (5.1)$$

where $N_{+-}(\Delta y)$ is the histogram of $|y(\pi^+) - y(\pi^-)|$ for all possible pairs within an individual event. $N_+(N_-)$ refers to all the positive(negative) particles used in the pairing.

5.1 Charged Particle Pairs

To begin the analysis of the balance function in heavy ion collisions, charged particle pairs are used. This measurement does not rely on particle identification and includes the most statistics possible that can indicate an overall behavior of the system. Further studies will show the behavior of pions as outlined in Section 5.3, kaons, or protons in particular.

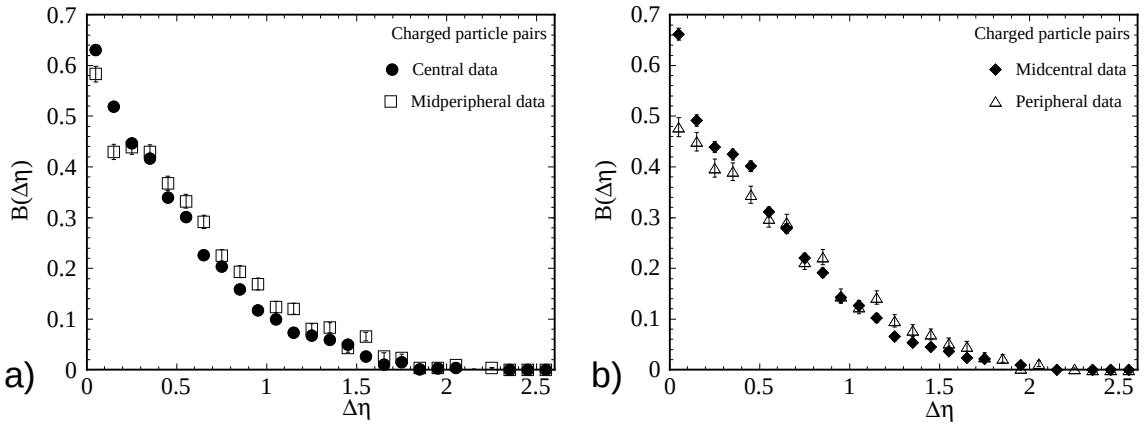

Figure 5.1: a) Central (circles) and midperipheral (squares) charged particle balance function, b) midcentral (diamonds), and peripheral (triangles) charged particle balance function.

The balance function measured for charged particle pairs is shown in Figure 5.1. This measurement consists of events from both central and minimum bias triggered data which pass the event, track, and quality cuts as discussed in Sections 2.5, 2.6, and 4.2.1. The centrality is defined as shown in Section 2.4, with the central multiplicity events represented by closed circles, the midcentral by open squares, the midperipheral by closed diamonds, and the peripheral by open triangles. The error bars shown are statistical only, calculated as shown in Equation 5.2.

$$\delta B_i = \frac{1}{2 * \text{binsize}} \sqrt{\left(\frac{\sqrt{N_{+-} + N_{++}}}{N_+}\right)^2 + \left(\frac{\sqrt{N_{-+} + N_{--}}}{N_-}\right)^2}. \qquad (5.2)$$

N_{+-} is the number of possible $|\eta(\text{particle}^+) - \eta(\text{particle}^-)|$ in a given $\Delta\eta_i$ bin. Here, the implicit summation over events is used as discussed in Chapter 3. The argument used is pseudorapidity (η), as rapidity cannot be calculated without each particle's mass known. The subscript i refers to the bins used, in this section the maximum number of bins is 26, with a binsize of 0.1.

A large peak near $\Delta\eta = 0$ can be seen in these charged particle pair balance functions. This peak did not agree with the predictions of the balance function shape in the simulations of reference [47], which seemed more Gaussian. Looking at the

dE/dx vs. p plot used for particle identification in Figure 2.9, one can see that there are particles which have a dE/dx profile similar to that of electrons in the primary particle data set. However, there should not be many electrons emerging from the primary particles of the collision. These electrons are most likely the products of secondary decays. Therefore, those electrons which can be identified are removed. Here, the $\Delta\eta$ axis is plotted out to the largest possible $\Delta\eta$ of 2.6, however there does not appear to be a significant balance function past $\Delta\eta$ of 2.0. Future plots will cut off at $\Delta\eta = 2.0$.

5.2 Charged Particle Pairs (No Electrons)

The balance function for charged particle pairs with identified electrons removed is shown in Figure 5.2. The central multiplicity events are represented by circles, the midcentral by squares, the midperipheral by diamonds, and the peripheral by triangles. The peak near $\Delta\eta = 0$ has now been diminished, although there appears to still be some electron contamination in the particles used. This contamination occurs when the electron dE/dx band crosses the pion, kaon, and proton bands. Hereafter all measurements labeled charged particle pair in the text are calculated without identified electrons, unless otherwise stated. It can be seen in Figure 5.2 that the balance function for charged particle pairs has a narrower width when measured for central events than peripheral events. The error bars shown are statistical only.

To make a comparison of the balance function of the different centrality bins, a method to calculate the width is necessary. One simple procedure is to calculate the weighted average of the balance function. That is:

$$\langle \Delta\eta \rangle = \frac{\sum_i (\Delta\eta_i B_i)}{\sum_i B_i}, \tag{5.3}$$

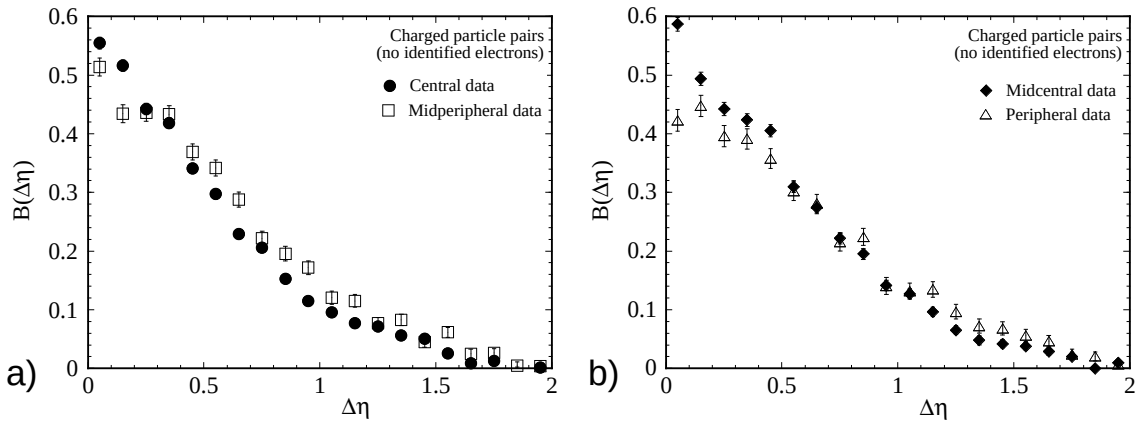

Figure 5.2: a) Central (circles) and midperipheral (squares) charged particle balance function, b) midcentral (diamonds), and peripheral (triangles) charged particle balance function. Charged particles do not include identified electrons.

where B_i is the balance function for each bin of the histogram. For charged particle pairs, $\Delta\eta_i$ is the value of the bin i calculated at the middle of the bin. The error on the balance function for each bin i is δB_i as given by Equation. 5.2. The summary of widths for the charged particle pairs at different centralities can be seen in Figure 5.3. The vertical error bars are calculated from statistics only, as in the equation 5.4.

$$\delta\langle\Delta\eta\rangle = \frac{\sum_i \Delta\eta_i B_i}{\sum_i B_i} \sqrt{\left[\frac{\sqrt{\sum_i \Delta\eta_i^2 \delta B_i^2}}{\sum_i \Delta\eta_i B_i}\right]^2 + \left[\frac{\sqrt{\sum_i (\delta B_i)^2}}{\sum_i B_i}\right]^2}. \tag{5.4}$$

Here, i represents the bins of the histogram, δB_i is from Equation. 5.2, and $\Delta\eta_i$ is the middle value of the i^{th} $\Delta\eta$ bin. Estimates for the systematic error will be covered in Section 5.6.

The horizontal error bars on the horizontal of Figure 5.3 represent the centrality width of each of the centrality bins. The widths are shown plotted with respect to centrality bins, however a more physical quantity can be used. The impact parameter was calculated with a simple geometrical model. The impact parameter refers to how central or head-on the different types of collisions are, as discussed in Section 1.2.

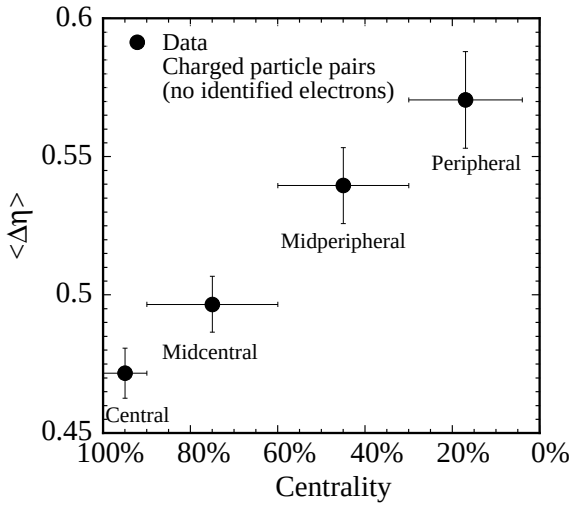

Figure 5.3: Summary of widths of charged particle pair balance functions for the four centrality bins of the data.

The calculation for impact parameter follows:

$$\frac{\int_0^{b'} 2\pi b db}{\pi b_{max}^2} = \text{central fraction.} \tag{5.5}$$

This equation relates the ratio of impact parameter (b) over the maximum impact parameter (b_{max}), to the fraction of centrality. The summary of balance function widths for charged particle pairs plotted with respect to the impact parameter is shown in Figure 5.4.

Another method to measure the width of the balance function is to use a Gaussian fit to the data. The balance functions shown in reference [47] appear to be of Gaussian shape. Exponential and power fits were tried, but the Gaussians appear to give the best fit to the data. To remove any extraneous electron contamination, the first bin of the charged particle pair balance function was removed for the Gaussian fit. The fits of the different events can be seen in Figure 5.5. The width, error of the width, and the χ^2 per degree of freedom of the fit are given on the figure for each statistical error bar weighted Gaussian fit. The summary of these Gaussian widths can be seen in Figure 5.6. For both the Gaussian and the weighted average widths shown in Figures 5.4 and

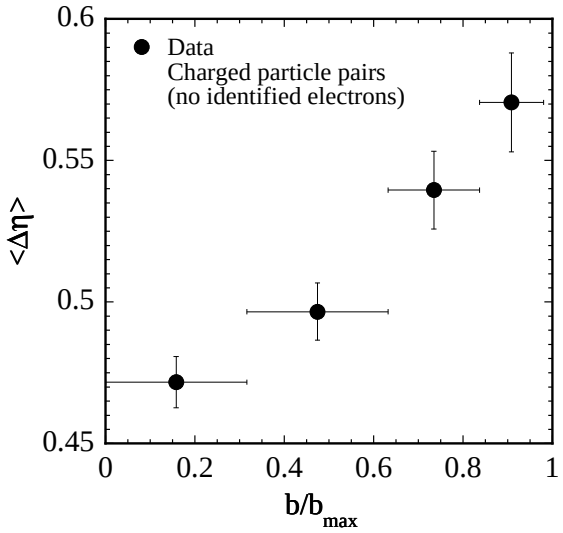

Figure 5.4: Summary of widths of charged particle pair balance functions for the four centrality bins of the data, plotted with respect to impact parameter.

5.6 respectively, it can be seen that the central events have a narrower balance function than the peripheral events. As centrality increases from peripheral to midperipheral towards central, the balance function narrows smoothly.

5.3 Pion Pairs

The pion pair balance function is calculated to obtain a measurement of the rapidity correlation between pions from the event's source. Using identified pions, the rapidity is calculated with mass of the pion = 0.13957018 GeV/c^2 [61], and can be used as the argument of the balance function. As the heavy ion events are expected to produce mostly pions, this measurement is the next logical measurement to extract the event's relative time information with sufficient statistics.

The pion pair balance function measured with respect to rapidity is shown in Figure 5.7. The central events are represented by circles, midcentral by squares, midperipheral by diamonds, and peripheral by triangles. As a comparison, the pion pair balance function measured as a function of pseudorapidity is shown in Figure 5.8 with the symbols following the same convention as in the previous figure.

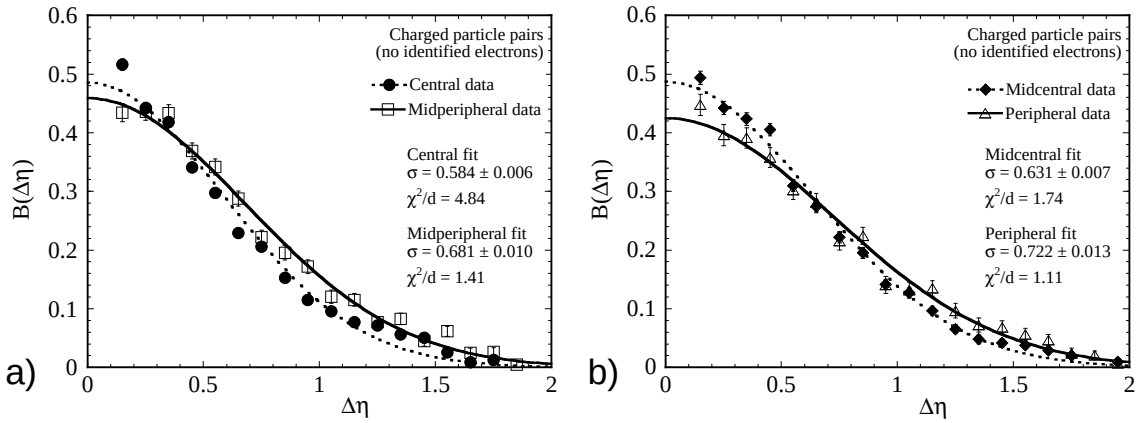

Figure 5.5: Charged particle balance function for a) central (circles), midperipheral (squares), b) midcentral (diamonds), and peripheral (triangles) events. The first bin is removed from the Gaussian fit which is shown by dotted (central, midcentral), or solid (midperipheral, peripheral) lines.

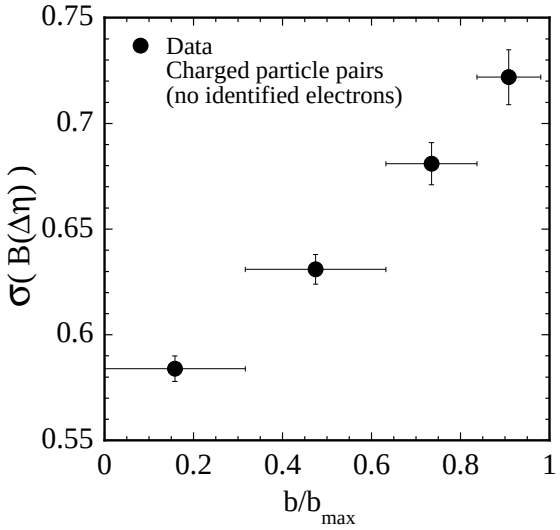

Figure 5.6: Summary of gaussian fit widths of charged particle pair balance functions for the four centrality bins of the data, plotted with respect to impact parameter.

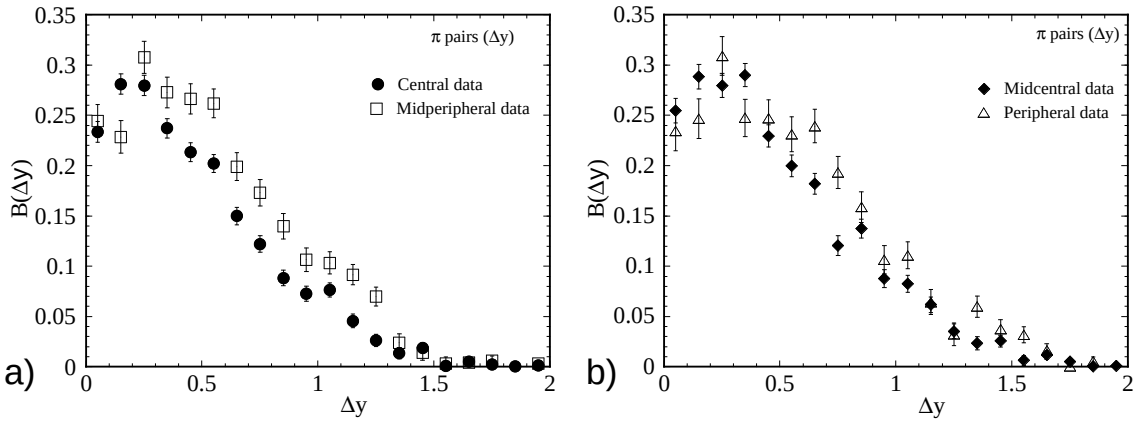

Figure 5.7: Pion pair balance function for a) central (circles), midperipheral (squares), b) midcentral (diamonds), and peripheral (triangles) events. This function is calculated with respect to Δy.

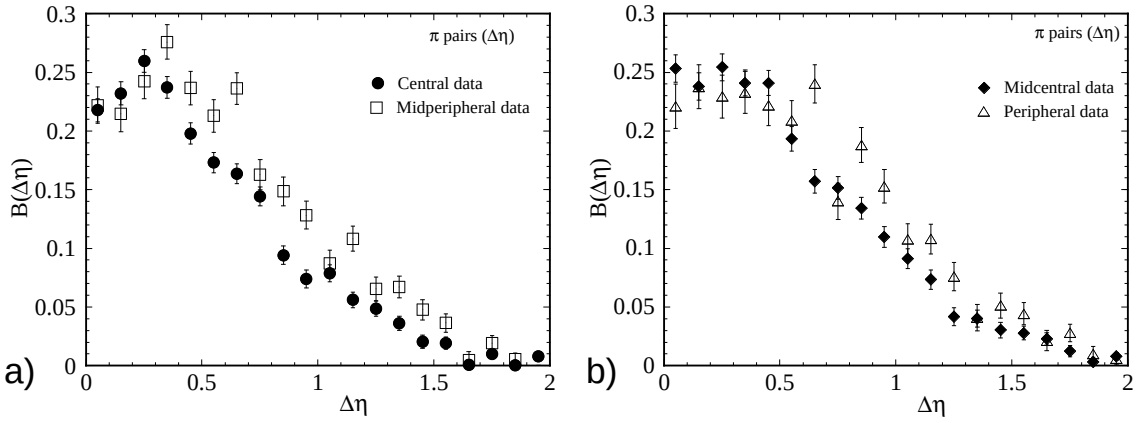

Figure 5.8: Pion pair balance function for a) central (circles), midperipheral (squares), b) midcentral (diamonds), and peripheral (triangles) events. This function is calculated with respect to $\Delta\eta$.

One feature that stands out is the dip near $\Delta y = 0$ in Figure 5.7. A similar, yet smaller feature is seen in Figure 5.8 near $\Delta\eta = 0$. This feature appears stronger in the balance function for pions measured with respect to rapidity, illustrating the effect of including the momentum in the observable. To understand this feature, the Hanbury-Brown-Twiss(HBT) [62] effect must be studied. HBT refers to a method of two-particle intensity interferometry. This method was originally applied to the measurement of the diameter of stars using photon correlations. In the fields of particle and nuclear physics, this type of technique has been used to study the size of the emitting source. With bosons, two-particle interferometry studies show an enhancement at a small momentum difference between identical particles. This HBT effect would enhance the probability that particles of like charge will have a small Δp. This enhancement then affects the rapidity difference, making a larger value for like-sign particle differences in low Δy. This enhancement for HBT creates a dip near small Δy in the balance function. This feature was modeled in reference [63] to include HBT and Coulomb corrections for like-sign particle repulsion. The result from [63] is shown in Figure 5.9. Qualitatively, Figure 5.7 shows the same sort of dip at low Δy, and with a similar relative magnitude to the amplitude of the function. It is also possible that other effects are manifest in this dip in the measurement. For example, electron contamination in the pion signal would give an enhancement at low Δy, thus the measured dip may not be as strong as a corrected balance function. Another possibility is that this dip is an effect of two-track merging, or even track splitting, which are estimated to be on the order of only 1% in a HBT-type correlation analysis, but may affect the balance function [31]. Figure 5.7 is from data, whereas Figure 5.9 does not include complete acceptance effects, and does not appear to die off at $\Delta y = 2$ as the balance function for data does. Overall, however, the HBT/Coulomb effect seems to be the major contributor to the local minimum in the pion rapidity balance function measured at low Δy.

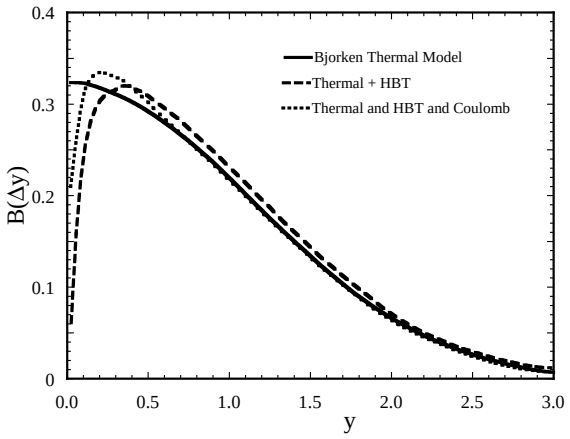

Figure 5.9: Pion pair balance function from Jeon & Pratt [63]. The balance function from the simple thermal Bjorken model (line) has been parameterized and filtered to roughly provide rough consistency with preliminary STAR measurements. The inclusion of HBT effects (triangles) gives a dip at small Δy, while the extra addition of Coulomb interactions (circles) modifies the dip.

To measure the width of the pion balance function measurement, both the weighted average as given by Equation. 5.3 and a Gaussian fit are used. In the case of the pion measurement, the first two bins are removed from both the width calculation and the Gaussian fit. This removes the HBT and other low Δy effects from the measured function, leaving a smooth curve to fit. A summary plot of all the pion widths from the weighted average is shown in Figure 5.10, plotted with respect to impact parameter. In contrast, Figure 5.11 shows the pion balance function widths calculated with respect to $\Delta\eta$.

The Gaussian fits and their χ^2 values are shown in Figure 5.12 for all four centrality bins. The summary of the data's Gaussian widths is shown in Figure 5.13. In the pion measurements, the general trend can still be seen, that of the peripheral data having the widest balance function. The width then narrows smoothly to the central events.

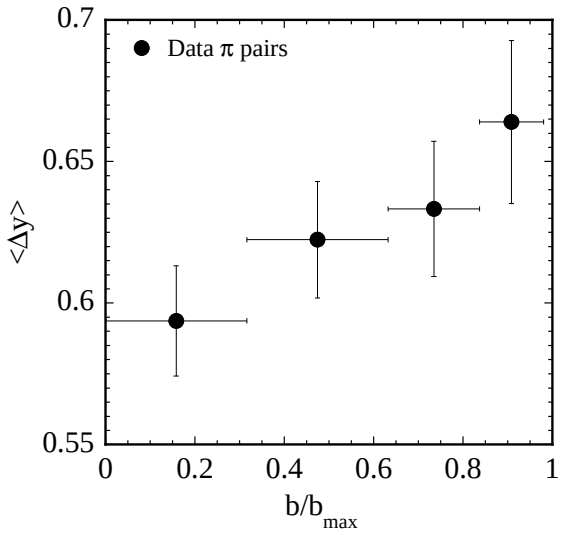

Figure 5.10: Summary of widths of the pion pair balance functions for the four centrality bins of the data, plotted with respect to impact parameter. The first two bins were removed from the data for the width calculation.

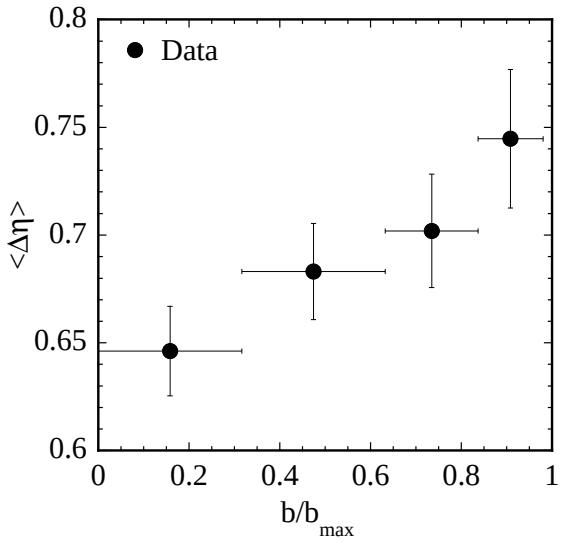

Figure 5.11: Summary of widths of the pion pair balance functions ($\Delta\eta$) for the four centrality bins of the data, plotted with respect to impact parameter. The first two bins were removed from the data for the width calculation.

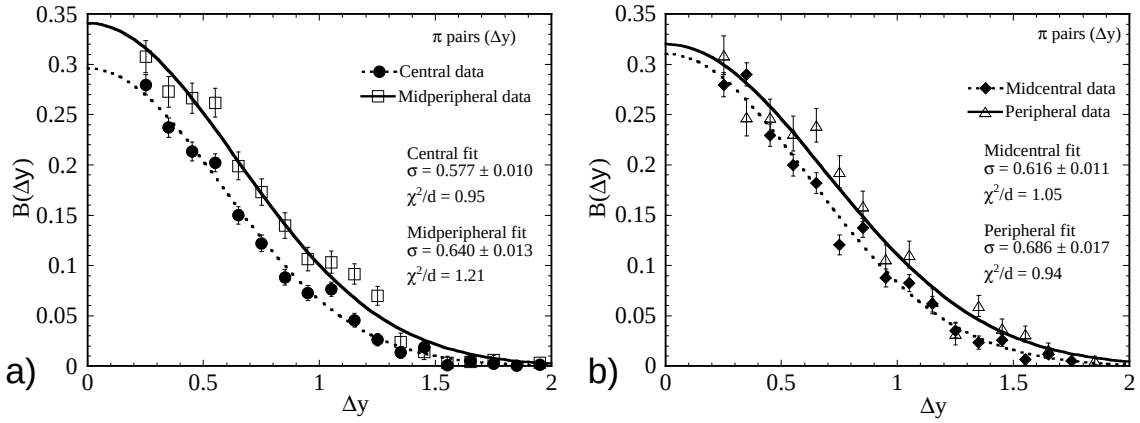

Figure 5.12: Pion pair balance function for a) central (circles), midperipheral (squares), b) midcentral (diamonds), and peripheral (triangles) events. This function is calculated with respect to Δy, and the first two bins are removed from the Gaussian fit (shown by dotted (central, midcentral), or solid (midperipheral, peripheral) lines.)

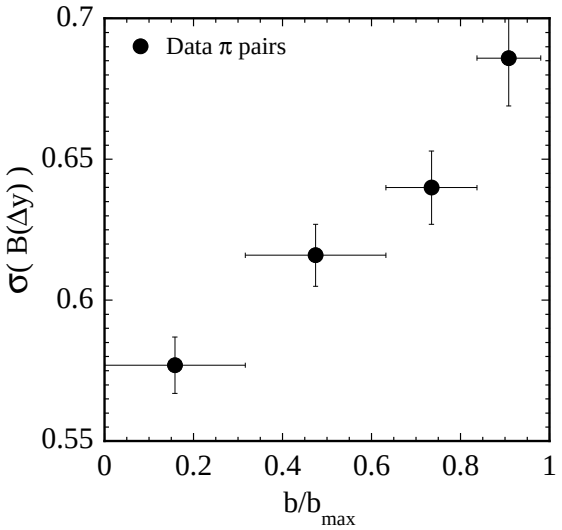

Figure 5.13: Summary of gaussian fit widths of pion pair balance functions for the four centrality bins of the data, plotted with respect to impact parameter. The first two bins were removed from the data for the fit.

5.4 Other Features of the Balance Function

The main comparison used in the balance function has been the width of the function. However, there are other features that are useful to understand the physics of the data set.

5.4.1 Integral

The integral of the balance function measurement may also give useful information. For a perfect detector, the balance function is constructed so that it normalizes to unity. However for a physical detector, the integral may show more information.

The possibility of measuring average fluctuations of charge to give a clear signal for the QGP [64], [65] was discussed in Chapter 3. In Jeon and Pratt [63], a relationship between the balance function and the fluctuation of charge is derived. This paper considers the case of a balance function which is measured with respect to rapidity difference (Δy), over a complete rapidity region Y. This is the same method that is used in the analysis in this dissertation. For $Q = N_+ - N_-$, and $N_{ch} = N_+ + N_-$ [63],

$$\frac{\langle (Q - \langle Q \rangle)^2 \rangle}{\langle N_{ch} \rangle} = 1 - \int_0^Y d\Delta y B(\Delta y) + O\left(\frac{\langle Q \rangle}{\langle N_{ch} \rangle}\right), \tag{5.6}$$

and O is the correction, which for electric charge in relativistic heavy ion collisions is usually less than 5%, as the amount of produced charges is much greater than the net charge. In the case of this dissertation, $Y = 2.6$ for the maximum rapidity difference. Reference [63] emphasizes the convenience that Equation 5.6 modifies the balance functions into one number that may give more information than just the width. However, they caution to not analyze charge fluctuations as a function of the varying rapidity window sizes. It is also possible to see trivially that the integral of the balance function depends upon the overall rapidity window Y. The changes in the balance function shape for different rapidity windows are discussed in Chapter 7.

Balance function integrals				
particle type	centrality	integral		error
pion(Δy)	central	0.208	$\pm$	0.003
pion(Δy)	midcentral	0.233	$\pm$	0.004
pion(Δy)	midperipheral	0.252	$\pm$	0.005
pion(Δy)	peripheral	0.257	$\pm$	0.006
charged particles($\Delta\eta$)	central	0.368	$\pm$	0.003
charged particles($\Delta\eta$)	midcentral	0.397	$\pm$	0.004
charged particles($\Delta\eta$)	midperipheral	0.399	$\pm$	0.005
charged particles($\Delta\eta$)	peripheral	0.384	$\pm$	0.006

Table 5.1: Table of the integral values for each of the balance function measurements shown.

The integral for each of the balance function measurements presented is given in Table 5.1. For both pions and charged particle pairs, the central events have a smaller integral than the peripheral events, with a smooth variation in between. Recalling the dN/dη histograms in Section 4.2.3, the central and peripheral events did not appear to differ as a function of the acceptance. However, there is a form [63] of Equation. 5.6, which corrects the balance function integral for a detector's acceptance:

$$\frac{\langle (Q - \langle Q \rangle)^2 \rangle}{\langle N_{ch} \rangle} = 1 - \int_0^Y d\Delta y B(\Delta y) * \left(1 - \frac{\Delta y}{Y}\right) + O\left(\frac{\langle Q \rangle}{\langle N_{ch} \rangle}\right). \qquad (5.7)$$

The left hand term of Equation. 5.7 is one-fourth of the D variable for measuring charge fluctuations which is discussed in Jeon and Koch [64]. Thus, a direct comparison to the predictions can be made. The integral with the acceptance corrections used to calculate $\frac{\langle (Q-\langle Q \rangle)^2 \rangle}{\langle N_{ch} \rangle}$ can be found in Table 5.2. Figure 5.14 shows that for all charged particle pairs, there does not appear to be a change in D over centrality. The predictions in reference [64] are that a QGP would have D $\approx$ 1, and a hadronic resonance gas would have a D $\approx$ 3. Measuring no effect with respect to centrality for the charged particle pairs seems to indicate that there is no QGP formed, however, that conclusion is dependent upon the theoretical model used in reference [64]. Understanding the detector acceptance dependency within the measured D is also not

Balance function acceptance corrected integrals				
particle type	centrality	integral		error
pion(Δy)	central	0.170	$\pm$	0.007
pion(Δy)	midcentral	0.188	$\pm$	0.008
pion(Δy)	midperipheral	0.200	$\pm$	0.011
pion(Δy)	peripheral	0.202	$\pm$	0.011
charged particles($\Delta\eta$)	central	0.301	$\pm$	0.007
charged particles($\Delta\eta$)	midcentral	0.322	$\pm$	0.008
charged particles($\Delta\eta$)	midperipheral	0.316	$\pm$	0.011
charged particles($\Delta\eta$)	peripheral	0.300	$\pm$	0.013

Table 5.2: Table of the acceptance corrected integral values for each of the balance function measurements shown.

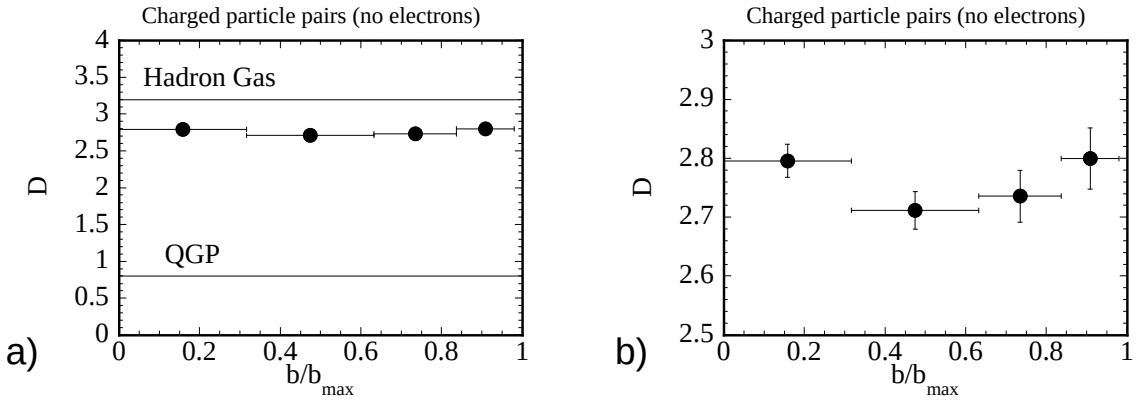

Figure 5.14: Plot of the values of D calculated from the balance function acceptance corrected integral for charged particle pairs. Plot a) is on a scale showing the QGP and hadronic gas predictions of reference [64], and b) is on a focused scale.

trivial. Results are shown here merely for illustration of the relationship between the balance function and other measurements. Given the large statistical errors in the D measurement, it appears that the width and shape of the balance function provide more information about the collision dynamics than the integral alone.

5.4.2 Particle Count

Table 5.3 summarizes the number of positive and negative particles of each type for the balance function analysis events. The column labeled "$\langle$ part per event$\rangle$" gives the number of particles per events that were used in the particle pairing for that

particle	cent-rality	total N+	total N-	events	⟨ part per event⟩	all events	⟨ part per event-all⟩
pi	c	20,197,232	20,335,228	95,089	426.26	95,204	425.74
pi	mc	9,690,679	9,753,709	71,976	270.15	72,311	268.90
pi	mp	1,559,441	1,562,546	44,858	69.60	45,164	69.13
pi	p	213,323	213,500	31,628	13.50	32,039	13.32
k	c	1,433,027	1,341,057	94,825	29.25	95,204	29.14
k	mc	669,546	626,425	71,201	18.20	72,311	17.92
k	mp	99,101	92,985	37,663	5.10	45,164	4.25
k	p	7,510	7,182	6,039	2.43	32,039	0.46
p	c	989,831	612,450	94,824	16.90	95,204	16.83
p	mc	468,434	297,696	71,003	10.79	72,311	10.59
p	mp	73,826	49,694	32,410	3.81	45,164	2.73
p	p	5,519	4,026	4,138	2.31	32,039	0.30
charged	c	39,422,376	38,271,168	95,204	816.07	95,204	816.07
charged	mc	18,202,012	17,708,452	72,311	496.61	72,311	496.61
charged	mp	2,699,237	2,633,753	45,164	118.08	45,164	118.08
charged	p	347,772	341,156	32,039	21.50	32,039	21.50
charged*	c	38,057,296	36,913,272	95,195	787.55	95,204	787.47
charged*	mc	17,589,620	17,096,200	72,287	479.83	72,311	479.68
charged*	mp	2,614,759	2,548,377	45,130	114.41	45,164	114.32
charged*	p	337,592	330,531	32,025	20.86	32,039	20.85

Table 5.3: Table of the number of positive and negative particles for each particle type used in balance function measurements. Centralities: c=central, mc=midcentral, mp=midperipheral, p=peripheral. Particle charged is all charged particles and charged* refers to all charged particles, no electrons. Ratios are calculated both for the average number of particles per event which had two or more of those particles "⟨ part per event⟩", and the average number of particles per event, covering all events used, "⟨ part per event-all⟩".

Ratios of (charged) to (pion) contributions to the balance function

centrality	N+-	d(N+-)	N++	d(N++)	N−−	d(N−−)
central	3.42399	0.00006	3.55447	0.00006	3.29857	0.00006
midcentral	3.21054	0.00010	3.32616	0.00010	3.09944	0.00009
midperipheral	2.76539	0.00040	2.84634	0.00041	2.68847	0.00039
peripheral	2.46190	0.00217	2.52195	0.00225	2.41134	0.00217

Table 5.4: Table of the ratio of the amount of particle pairs(charged/pion) used in balance function analysis for each term (N+-, etc.).

given particle. For particles such as kaons and protons, it can be seen that in the very peripheral events, the events used in the analysis had on average 2 of these particles per event. Considering all events used ("all events"), there is less than 1 proton or kaon per event on average for the most peripheral events. However, the more central events do have a larger number of both protons and kaons. These statistics will become significant for those particular particle's balance function measurements, addressed later in Section 5.5.

The contribution of the amount of particle pairs to the balance function measured is summarized in Table 5.4. Given are the ratios of charged particle pairs to pion pairs used for each centrality. It can be seen that there are more charged particle pairs to the pion pairs used in central events compared to peripheral events. This could be an indication of a changing number of non-pions in the central events, perhaps more kaons or protons. However, the particle identification cut is fixed based upon minimum bias events. It is more likely that there are merely more pions in the central events which are not identified with the fixed number of σ cut. With respect to the balance function width, it is expected that the more massive particles, such as kaons and protons, should display a strong centrality dependence [47]. The charged particle pair data set combines the pion, proton, and kaon signals, which could explain the larger relative difference between central and peripheral balance function widths in the combined all charged particle data set.

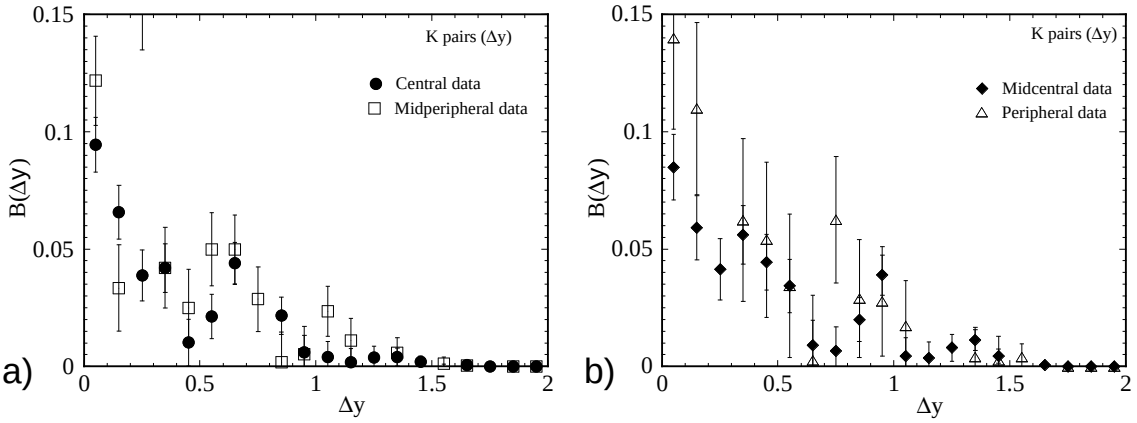

Figure 5.15: Kaon pair balance function for a) central (circles), midperipheral (squares), b) midcentral (diamonds), and peripheral (triangles) events. This function is calculated with respect to Δy.)

5.5 Kaon Pairs

The predictions of reference [47] indicate that the heavier particles in a collision, such as kaons or protons, would display a stronger balance function width difference than pion pairs when p+p collisions are compared with QGP-producing collisions. The kaon balance function, measured with respect to rapidity, can be seen in Figure 5.15. It is evident immediately that the statistics in this data set are too low to make conclusions about the Kaon balance function. The balance function for kaons measured as a function of $\Delta\eta$ is shown in Figure 5.16. Even having removed the additional measurement of momentum which is part of the rapidity calculation, the balance function does not appear any smoother. In the peripheral events, there are too few kaons to be of use, as can be seen in Table 5.3. The widths are not shown for these statistical reasons.

5.6 Systematic Error

The balance function measurements presented have only included the statistical error due to the number of particles used. However, an estimate of the systematic error is

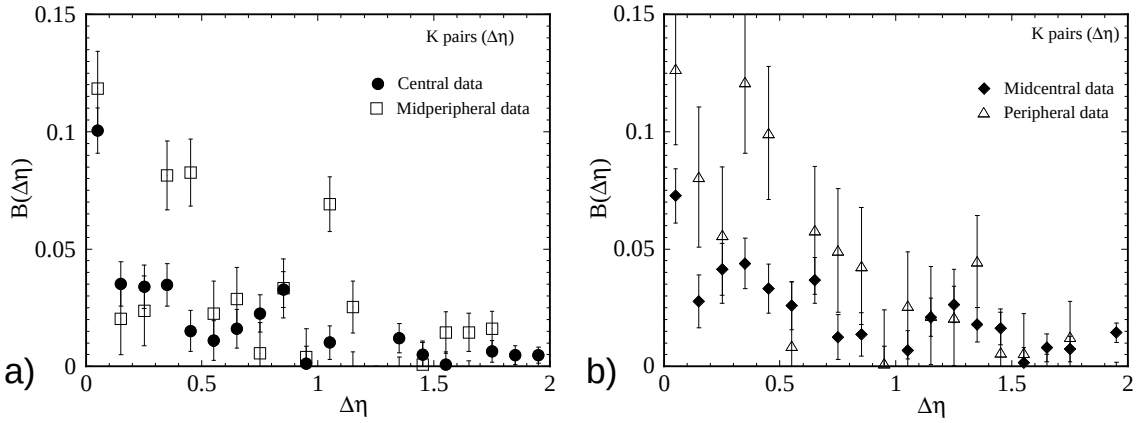

Figure 5.16: Kaon pair balance function for a) central (circles), midperipheral (squares), b) midcentral (diamonds), and peripheral (triangles) events. This function is calculated with respect to $\Delta\eta$.)

needed to properly understand the data results. Systematic error can come from a number of things. There is an expected uncertainty in tracking, where particles may be missed due to their track length. Also, it is possible that two tracks will merge, appearing to be one track with physical features that are no longer correct for either of the two tracks. Another possibility is that a track may split, when one particle's track will have a gap in it or some other feature that causes it to be identified as two separate particles instead of one. Both the split and merged track possibilities are reduced by the track cuts, covered in Section 2.6. To estimate the systematic error on calculating the balance function, an understanding of the tracking efficiency is needed.

The tracking efficiency was found through embedding events. Embedding is a method where simulated particles are inserted into real data events, and then identified through the usual track reconstruction routine. The simulated particles inserted are compared with the reconstructed data, and in this way the efficiency is estimated. This study was done by STAR collaborators, including M. Calderon, and covered in his dissertation [37]. For cuts which are similar to those used in this dissertation, the tracking efficiency was estimated to be about 85 to 90% in the region of $|\eta| < 1.0$,

with a drop to 75% at $|\eta| = 1.3$ [37].

Another source of error is the finding of the primary vertex of the event. For high multiplicity events, i.e. central and midcentral centrality, the vertex is estimated to have a resolution of 150 μm in the z-direction [37]. In the calculation of the balance function, the vertex position is not so important as the identification of particle tracks which point back towards the primary vertex. However, these two features are dependent upon each other, this dependence can be another source of systematic error, especially as the vertex finding efficiency is estimated to be 100% for events with more than 50 primary tracks, but decreases down to 60% for events with fewer than 5 primary tracks [37].

For the case of the pion pairs, systematic error can arise from both the use of particle identification and the calculation of rapidity which uses both pseudorapidity and momentum variables. For particle identification, the dE/dx and momentum measurements are used together to tag particles as discussed in Section 2.7. As reported in reference [37], the best achievable resolution for the dE/dx is 7.8%, for tracks which have 31 dE/dx points used in the measurement.

Examining the form of equation 3.2, and considering the implicit summations, it is not clearly evident where these errors should be included to obtain the systematic error. The statistical error for the balance function can be calculated:

$$\begin{aligned} \delta B &= \sqrt{\left(\frac{1}{2 * \text{binsize}}\right)^2 \left[\frac{(\delta N_{+-})^2 + (\delta N_{++})^2}{(N_+)^2} + \frac{(\delta N_{-+})^2 + (\delta N_{--})^2}{(N_-)^2}\right]}, \quad (5.8) \\ &= \frac{1}{2 * \text{binsize}} \sqrt{\frac{N_{+-} + N_{++}}{(N_+)^2} + \frac{N_{-+} + N_{--}}{(N_-)^2}}. \end{aligned}$$

Systematic error could be included for the N_{+-}, N_{++}, N_{-+}, and N_{--} measurements. It could also be included for $\Delta\eta$(or Δy), which would indirectly affect the balance function and directly affect the weighted average. Since N_{+-} and the three other similar terms represent a sum over possible pairs in a give $\Delta\eta$ or Δy, the combined

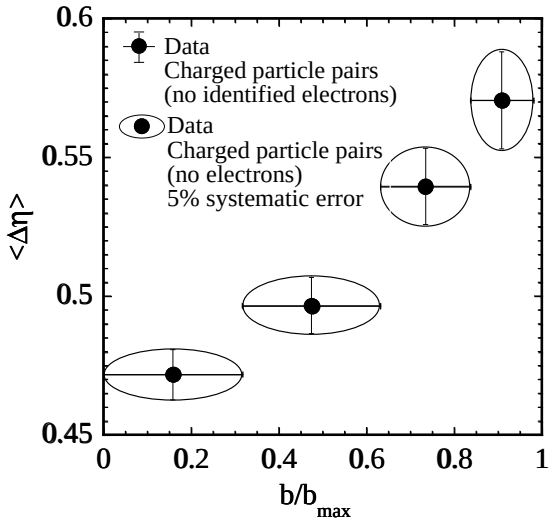

Figure 5.17: A summary of the balance function widths for charged particle pairs, comparing both with(errors indicated by ovals) and without(vertical error bars) a 5% systematic error in the N_{+-}-type terms.

systematic error in the count as well as the measurement of η or y would be needed. The systematic error can be estimated and the effect upon the balance function studied. For instance, if one estimates an additional 5% systematic error for the N_{+-}-type terms, then the systematic error corrected Equation. 5.9 will have an extra term that commutes to the front of the form of $(1 - 0.05)\times$ Equation. 5.9. When the balance function is plotted for the 5% error, the difference in the error bars with and without the systematic included can hardly be seen. The error bars change length by about 0.15%. Figure 5.17 shows the summary of the widths of charged particle pairs comparing statistical errors only (vertical bars) to statistical and systematic errors (height of ellipse). Figure 5.18 shows the same summary for pion pairs, again the difference between errors is small, about 0.22%.

For a more conservative error estimate, a systematic error of 10% is tried. Figure 5.19 shows the summary of error comparison for charged particle pairs with and without a 10% systematic error. Figure 5.20 shows the same for pion pairs. The charged particle error bar changes by at most 0.3%, and the pion error bar by 0.4%. Even with this more conservative, yet reasonable, error bar estimate, the overall behav-

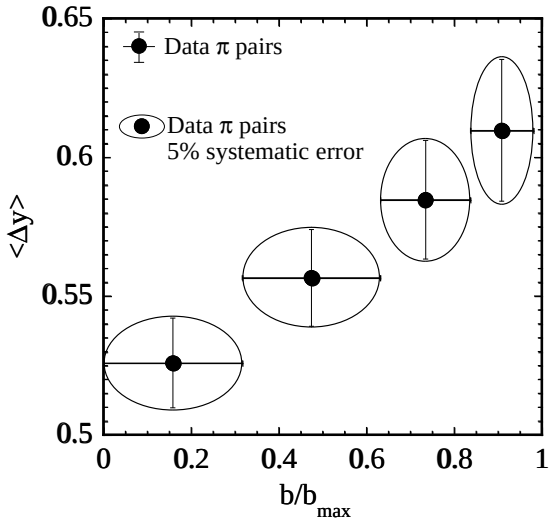

Figure 5.18: A summary of the balance function widths for pion pairs, comparing both with(errors indicated by ovals) and without(vertical error bars) a 5% systematic error in the N_{+-}-type terms.

ior of the balance function widths remains statistically significant. Thus, even for an over-estimate of the counting error in the N_{+-}-type terms, there is little contribution from the systematic error to the balance function width.

For the systematic error in measuring $\Delta\eta$ or Δy, the same technique can be used, estimating a 5% additional systematic error and studying the affect on the balance function widths. Figure 5.21 shows how that estimate affects the plot of the balance function for charged particle pairs. The actual error is estimated to be 2% on η measurements [37], giving an error of $\Delta\eta$= 2.8%, thus the 5% error estimate is a generous one. However, for rapidity, combining a 2% error in η and a 2% error in momentum measurement, an estimate of a 5% error on Δy is reasonable.

The greater effect of the error in $\Delta\eta$ or Δy on the width can be seen in Figure 5.21. To calculate the width, an adjustment on the weighted average error bar is needed. Returning to the width error calculation, in Equation. 5.4 a term for the Δy error is added on.

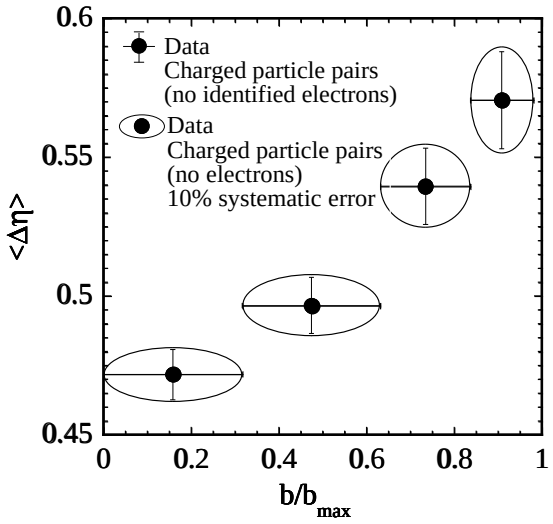

Figure 5.19: A summary of the balance function widths for charged particle pairs, comparing both with(errors indicated by ovals) and without(vertical error bars) a 10% systematic error in the N_{+-}-type terms.

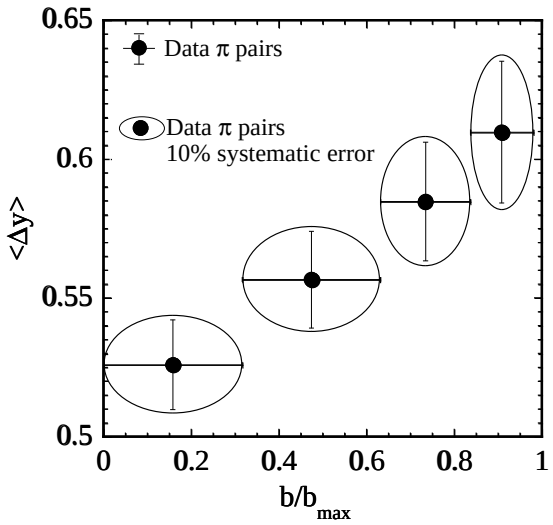

Figure 5.20: A summary of the balance function widths for pion pairs, comparing both with(errors indicated by ovals) and without(vertical error bars) a 10% systematic error in the N_{+-}-type terms..

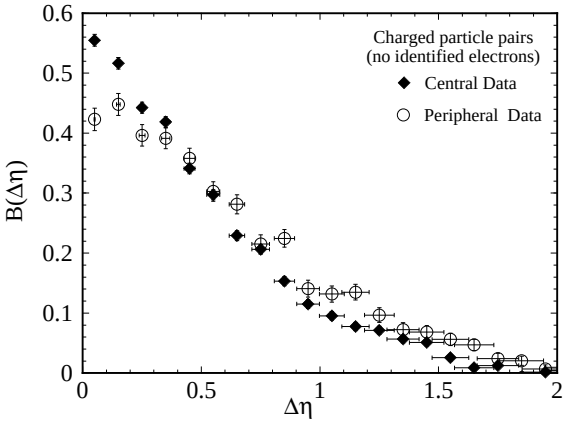

Figure 5.21: Charged particle pair balance function plotted with an estimated 5% systematic error on $\Delta\eta$ in addition to the statistical error.

$$\delta\langle\Delta\eta\rangle = \frac{\sum_i \Delta\eta_i B_i}{\sum_i B_i}\sqrt{\left[\frac{\sqrt{\sum_i \Delta\eta_i^2 \delta B_i^2}}{\sum_i \Delta\eta_i B_i}\right]^2 + \left[\frac{\sqrt{\sum_i (\delta\Delta\eta_i)^2 B_i^2}}{\sum_i \Delta\eta_i B_i}\right]^2 + \left[\frac{\sqrt{\sum_i \delta B_i^2}}{\sum_i B_i}\right]^2}. \tag{5.9}$$

Placing the additional error in the $\Delta\eta$ or Δy measurement gives the most effect, somewhat similar to the 10% systematic on the N_{+-}-type terms. A 5% systematic error in the measure of $\Delta\eta$ shows a difference from the widths calculated with only

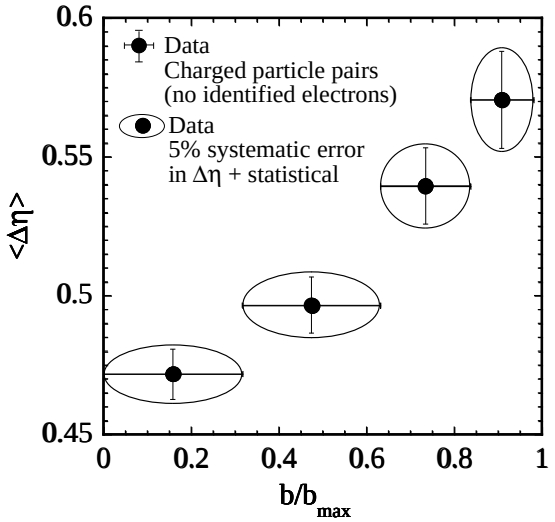

Figure 5.22: Charged particle pair balance function widths plotted with (ovals) and without (vertical error bars) an additional 5% systematic error on $\Delta\eta$.

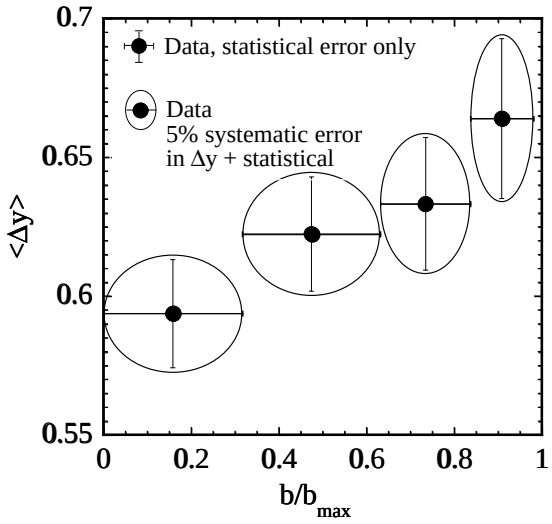

Figure 5.23: Pion pair balance function widths plotted with (ovals) and without (vertical error bars) an additional 5% systematic error on $\Delta\eta$.

the statistical error, as can be seen in Figure 5.22. In Figure 5.23, the 5% systematic error estimate is included in the pion pair balance function width calculation. The effect is again visible, with a change in error bars for charged particles of about 1.1%, and about 1.3% for pions. However, even with the inclusion of these systematic errors, the difference in balance function width between the central and peripheral data sets can still be seen.

The systematic errors discussed here come from a variety of sources. Tracking studies [37] show a known efficiency in track measurements, i.e. how many tracks are identified of those which enter the TPC. Single tracks can be split into two tracks, and two individual particle tracks can be merged into single tracks by the tracking reconstruction software. Each measurement of a particle track's η has an accuracy, which affects the $\Delta\eta$ and Δy calculations. These measurements have some multiplicity dependence. For high multiplicity events, merged tracks are more likely than in low multiplicity events. However, low multiplicity events have a lower efficiency in primary collision vertex identification. These factors may combine, and even cancel each other out. A conservative estimate of systematic error would be 10% in the N_{+-}-type

terms, combined with 5% in the $\Delta\eta$ measurement. The addition of these systematic errors to the statistical errors does not overshadow the difference between central and peripheral balance function widths.

5.7 Balance Function Calculation Checks

Checking the calculation of the balance function is as important as checking the quality of the data. As mentioned in Section 4.2.4, during the programming stage of the balance function analysis the subroutine calculations were checked for accuracy with known input and output. This together with ensuring that the same analysis code was used for each separate balance function analysis which is compared ensures that the calculations which give the measurements shown are accurate. However, the shape and behavior of the balance function could have aspects which are not apparent with the bin size chosen. Also, the symmetry of the measurement can be checked by removing the absolute value in the $\Delta\eta$ or Δy part of the measurement.

5.7.1 Bin Size Variation

It is important to verify that the balance function measurements do not have a dependence on bin size. To check this, balance function measurements were made with 65 bins in the measurement range instead of 26. The range of measurements used is from 0 to 2.6 in both $\Delta\eta$ and Δy. The majority of measurements shown use the 26 bins which have a binsize of 0.1. The 65 bin balance function has a binsize of 0.04, with both the binsize and amount of bins chosen to be significantly different than the 26 bin method. In this analysis, event files from the P00hm library were used. This analysis was performed before some of the runs with bad or suspect trigger were removed. However, both the 26 and 65 bin balance functions for this data set are shown for comparison.

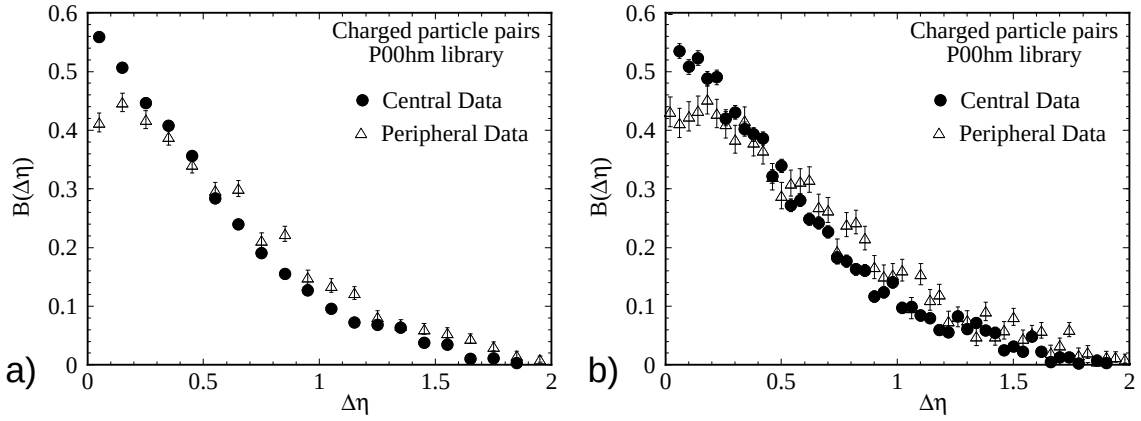

Figure 5.24: Charged particle pair balance function for central (circles), and peripheral (triangles) events of the P00hm data set. Measurements are shown for both a) 20 bins and b) 50 bins in the $\Delta\eta$ region of 0 to 2.

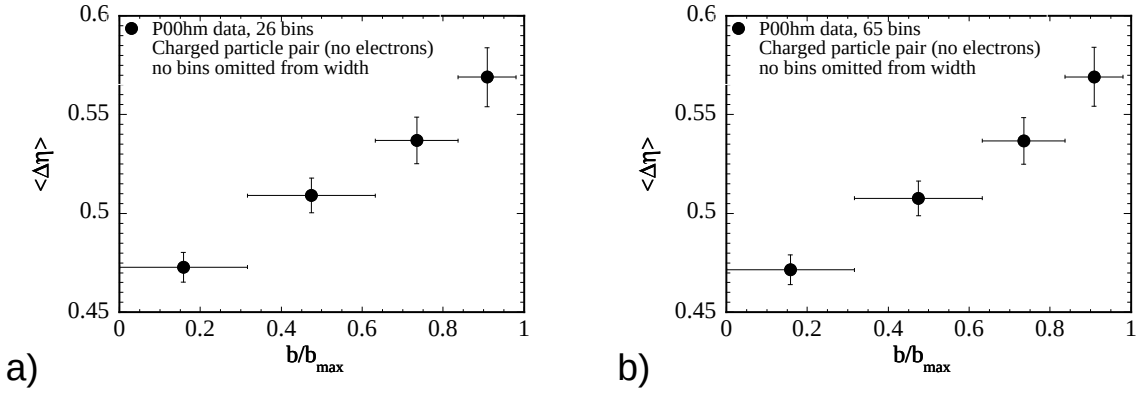

Figure 5.25: Charged particle pair balance function widths for the P00hm data set. Widths calculated with all bins are shown for both a) 26 bins and b) 65 bins in the $\Delta\eta$ region of 0 to 2.6.

The charged particle pair balance function for central and peripheral P00hm events is shown in Figure 5.24. The same behavior in the balance function can be seen for the different bin sizes, considering statistical variation. It appears that for the charged particle pair balance function measurement is not dependent on bin size. This comparison can be seen more clearly using the weighted average width calculation. These widths are shown in Figure 5.25 for charged particle pairs. There is very little difference between the results for different bin sizes.

Figure 5.26 compares different bin sizes for the pion pair balance function meas-

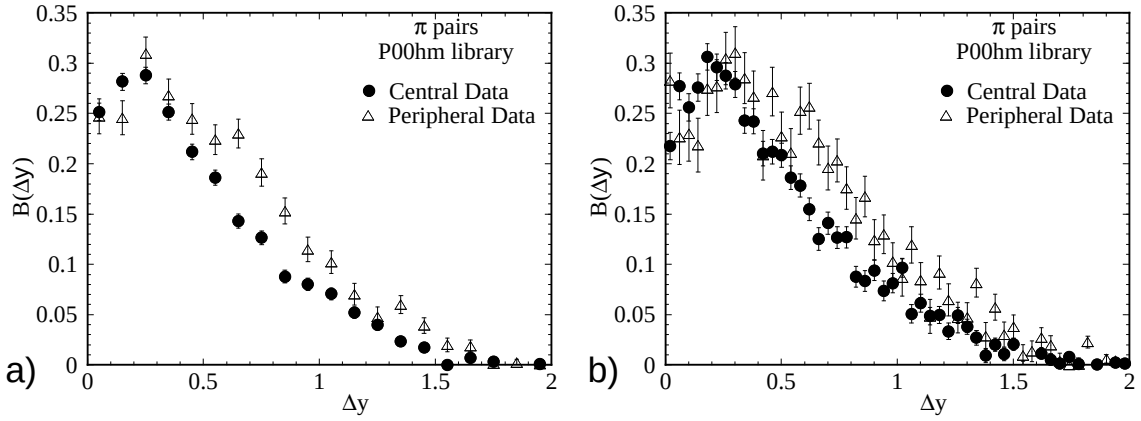

Figure 5.26: Pion pair balance function for central (circles), and peripheral (triangles) events of the P00hm data set. Measurements are shown for both a) 20 bins and b) 50 bins in the Δy region of 0 to 2.

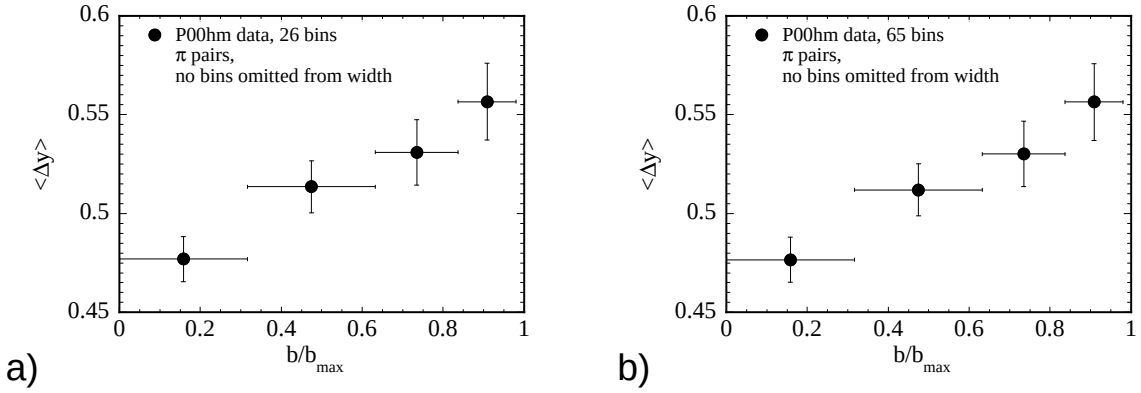

Figure 5.27: Pion pair balance function widths for the P00hm data set. Widths calculated with all bins are shown for both a) 26 bins and b) 65 bins in the Δy region of 0 to 2.6.

ured for P00hm events. As with the charged particle pairs, there is little difference in the overall shape and width of the balance function for bin sizes of 0.1 shown in Figure 5.26 a), and 0.04 shown in Figure 5.26 b). The pion pair widths for the different number of bins is shown in Figure 5.27. Similar to the charged particle pairs, there is little change between the two different bin size balance function widths for each centrality. Note that the low Δy HBT effects have not been removed from the calculation in Figure 5.27.

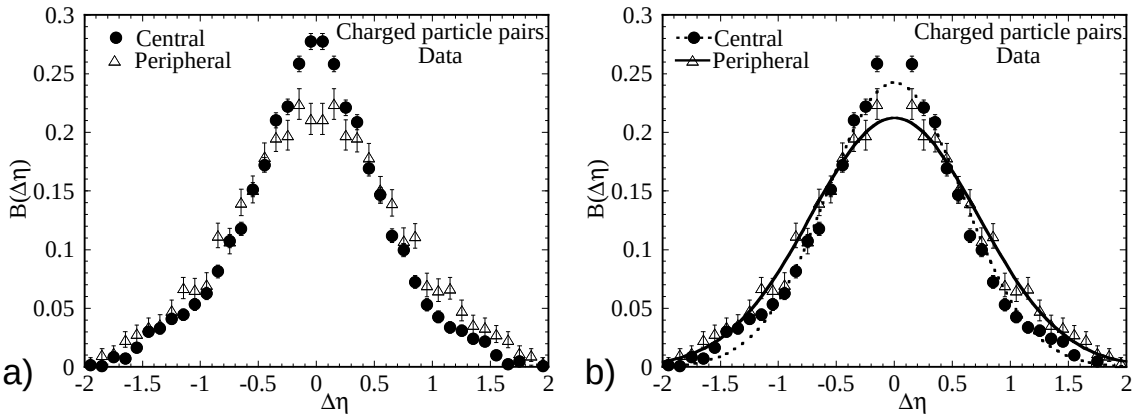

Figure 5.28: Charged particle pair balance function for central (circles), and peripheral (triangles) events of the complete data set. Measurements are shown both a) with all bins and b) omitting two middle bins with the dashed line showing the central Gaussian fit, and the solid line showing the peripheral Gaussian fit.

5.7.2 No Absolute Value

The balance function described by Equation 5.1 can be modified by removing the absolute value in the N_{+-}-like terms, making them the number of particle pairs in a given $\Delta\eta$ bin, i.e. $N_{+-} \equiv \eta(\text{particle}^{+} - \text{particle}^{-})$. In this case, $N_{+-} \neq N_{-+}$. For charged particle pairs the balance function for the final data set without absolute value is shown in Figure 5.28. The measurements are shown both with and without the Gaussian fit. The height of the balance function is reduced by half as expected from the balance function with absolute value, and the integrals for the two measurements are close. The integral for the central data charged particle balance function is 0.368 ± 0.003 with absolute value, and 0.370 ± 0.003 without absolute value. It can also be seen that the central data set has a narrower balance function than the peripheral data set. It is also evident that the measurement is symmetric in $\Delta\eta$. The balance function shown here has a total of 52 bins from $-2.6 < \Delta\eta < 2.6$, with a binsize of 0.1.

The balance function calculated without absolute value for pion pairs is shown in Figure 5.29. The Gaussian fit is shown without the four middle bins, corresponding to the two bins removed from previous pion analysis to leave out the HBT effect. The

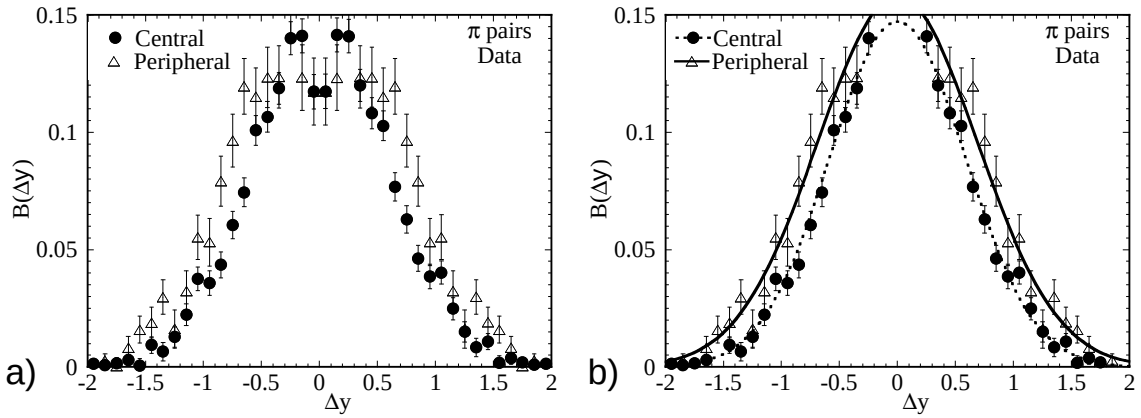

Figure 5.29: Pion pair balance function for central (circles), and peripheral (triangles) events of the complete data set. Measurements are shown both a) with all bins and b) omitting four middle bins with the dashed line showing the central Gaussian fit, and the solid line showing the peripheral Gaussian fit.

central data has a narrower balance function than the peripheral data, just as with the absolute value balance function. Also, the function shown is symmetric about $\Delta y = 0$. There is structure seen in the balance function measurement without absolute value, in particular, a regular bump in the peripheral events at $|\Delta\eta| = 1.2$, this is the other regular systematics are most likely due to detector effects. For instance, these could include more tracks which cross the central membrane, or a change in track efficiency between the inner and outer sectors. However, the effects seen are within the estimated statistical and systematic error bars. Thus it appears that the measurements shown here are correct, and do not contain any obvious calculation flaws.

5.8 Data Summary

It is clear from Figures 5.6 and 5.13 that there is a common trend to the charged particle and pion balance function measurements. The 10% most central events have a balance function which is significantly narrower than the peripheral events. As the event type becomes more peripheral, the balance function width increases. From the

predictions which are covered in Chapter 3, this could be evidence of late hadronization in the most central of the Au+Au 130 GeV collisions. Also, it can be seen that the D variable can be calculated from the integral of the balance function, and it does not appear to show any strong change with respect to centrality. To have a complete understanding of the meaning of these data measurements, other aspects of the balance function must be studied. Chapters 6 and 7 will provide insight into the balance function with simulations, mixed events, and cuts on the data sets.

Chapter 6

Simulations

To understand the detector response or the behavior of an observable in a physics analysis, simulations are often used. A simulator program is usually based upon particle interaction models, which include as much physics as possible. Where aspects of the physics are not known or proven, parameters are derived from experimental measurements.

Two particle simulators were used, HIJING and the Bjorken thermal simulator. These simulators were processed through two STAR detector simulators for comparison with data. The output of the simulators was also used to study the behavior of the balance function in a perfect detector.

6.1 HIJING

HIJING includes the successful implementation of perturbative-QCD (PQCD) processes in the PYTHIA model for hadronic interactions. HIJING with default settings has been shown to match a number of observables of standard p+p and heavy ion collisions. It is used widely in the heavy ion physics community. In this dissertation, HIJING is used for modeling superposition of nucleon-nucleon collisions, both of p+p as well as Au+Au collisions.

HIJING is a fairly complete model, and with respect to the balance function, only lacks the modeling of final state interactions. However, as discussed in reference [47], the final state interactions would only broaden the measured balance function. Thus, HIJING balance function measurements can be compared meaningfully with data, with the understanding that a real measurement of a hadron gas may have a wider balance function than what HIJING shows.

6.1.1 GEANT

GEANT is another standard in high energy and heavy ion physics [66]. It is a software detector response simulator with which the user may input all the physical characteristics of the detector: material, placement, magnetic field, etc. Particles from an event simulator HIJING(in this case) are input into GEANT, and it then calculates the probable interactions of those particles with the given detector structure. GEANT has been designed to accurately predict the behavior of detectors. GEANT was implemented for the STAR detector. This software is termed GSTAR [59]. GSTAR was used with STAR's 2000 detector configuration, with the magnetic field at half strength. After events are analyzed through GSTAR, they are run through the TPC Response Simulator (TRS), where the GEANT tracks are converted into signals which are of the same type as the real data from the TPC [58].

6.1.2 TRS

The TRS models four modes of the TPC operation, the ionization transport, the charge collection, analog signal generation, and digital signal generation. Each of these modes is carefully modeled to take into account realistic aspects of diffusion, signal shape which is analyzed by the electronics, design details, and material specifics of the TPC [58] [67]. Analyses within TRS were written taking into account lessons from past detector simulators. TRS was checked through embedding, where GEANT-

produced particles are run through GSTAR and TRS and then placed within real data sets. Tags are included in the embedded events to allow the labeling of these embedded tracks. The TRS version used in P00hi and P00hm libraries was found to reproduce the data in the geometrical variables in tests by the STAR collaboration [60].

Thus, by running simulated events through GSTAR and TRS, they closely resemble what events with that particular simulator model would look like when measured with the STAR TPC. HIJING events which have been run through GSTAR and TRS will be referred to hereafter as HIJING-GEANT, with the STAR geometry and TPC reconstruction being implicit.

6.1.3 Charged Particle Pair Balance Function

These HIJING-GEANT events are used as a reference for the result of a collision which can be understood as a superposition of nucleon-nucleon collisions. First the accuracy of HIJING as a nucleon-nucleon model must be tested. In the balance function paper, the simulation shown was PYTHIA generated p+p collisions at 200 GeV. To be assured that the balance function for HIJING Au+Au collisions is consistent with that of HIJING p+p, simulations were done with the assumption of a perfect detector. Shown in Figure 6.1 is the balance function calculated for HIJING Au+Au $\sqrt{s_{NN}} = 130\ GeV$ events and HIJING p+p $\sqrt{s_{NN}} = 130\ GeV$ events.

The two types of events have the same balance function shape and width within statistical error bars. In this case and all other HIJING events discussed in this dissertation unless otherwise specified, HIJING was run with the default settings. This means that there is no jet quenching turned on, there is no enhanced high p_t jet production, and there is no nucleon shadowing [57].

Thus, we can use the HIJING through GSTAR and TRS events as a valid comparison to the measured data. The charged particle pair balance function for these detector-simulated HIJING events is shown in Figures 6.2 a) and b). The charged

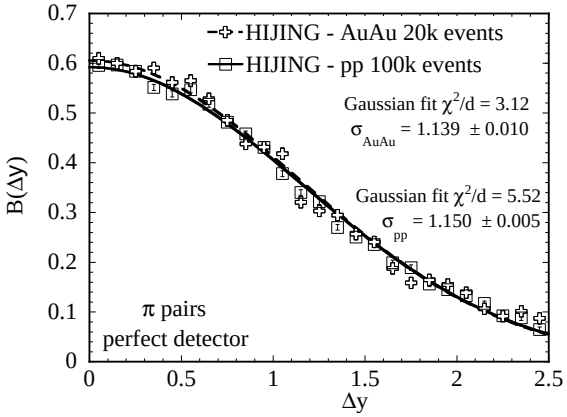

Figure 6.1: Pion pair balance function for HIJING Au+Au (plusses) and p+p (squares) events. This balance function is calculated for a perfect detector.

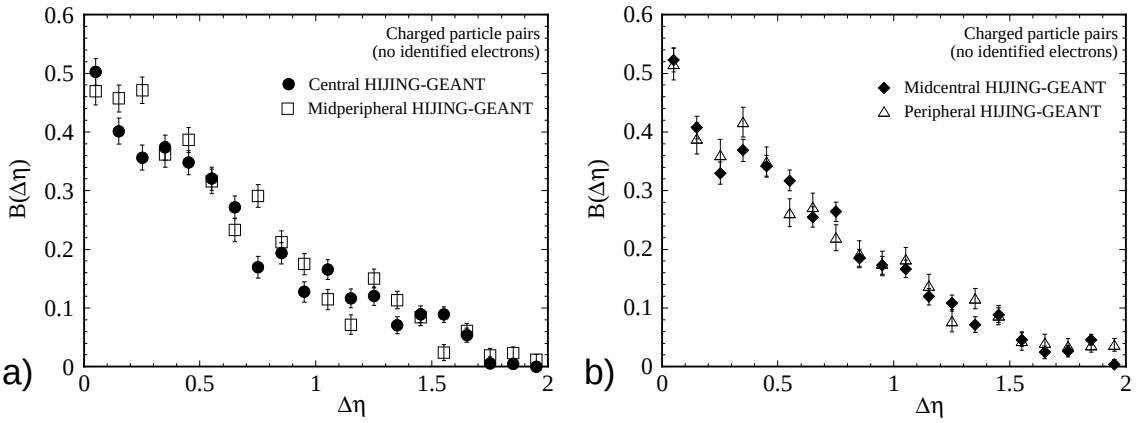

Figure 6.2: a) HIJING-GEANT central (circles) and midperipheral (squares) charged particle balance function, b) midcentral (diamonds), and peripheral (triangles) charged particle balance function.

particle pairs exclude identified electrons. The same four centralities are plotted with Gaussian fits, excluding the first bin in Figures 6.3 a) and b). The balance functions for different centralities have the same shape and width within the statistical error bars of the HIJING-GEANT data set. This reflects the hadron gas properties of the HIJING model, in that the balance function has the same shape and width for simulations at different impact parameters. This can be clearly seen in Figure 6.4 which plots the width of the HIJING-GEANT balance function with respect to the four centrality bins. Figure 6.5 shows the same non-centrality dependence in the Gaussian fit widths for HIJING-GEANT simulated events.

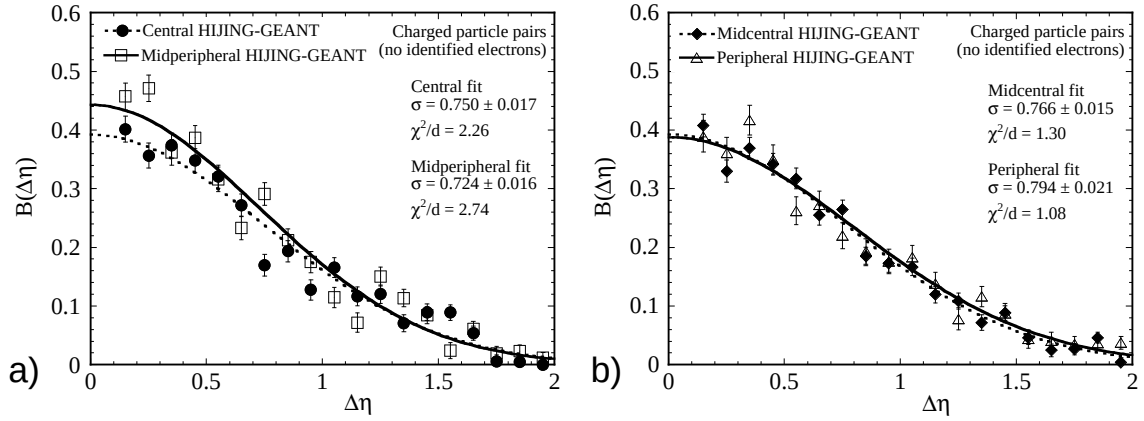

Figure 6.3: a) HIJING-GEANT central (circles) and midperipheral (squares) charged particle balance function, b) midcentral (diamonds), and peripheral (triangles) charged particle balance function. Gaussian fits are shown excluding the first bin from the fit.

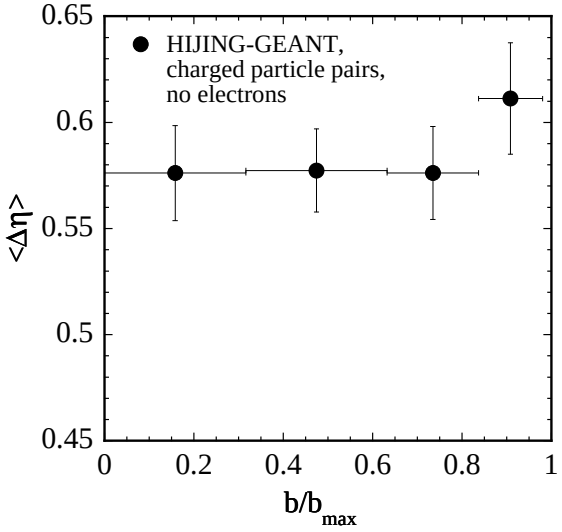

Figure 6.4: Summary of widths of charged particle pair balance functions for the four centrality bins of HIJING-GEANT, plotted with respect to impact parameter.

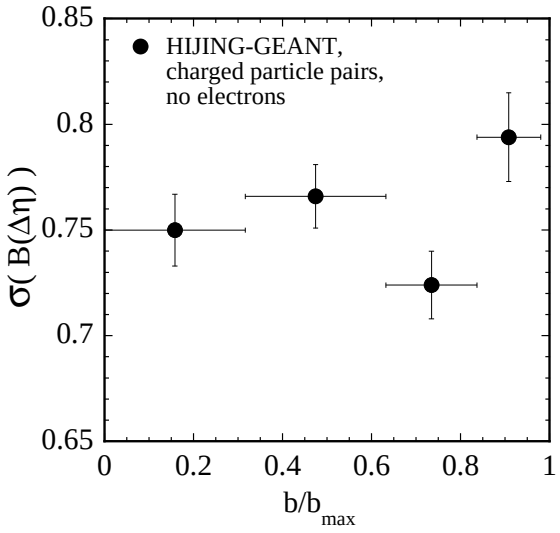

Figure 6.5: Summary of Gaussian fit widths of charged particle balance functions for the four centrality bins of HIJING-GEANT, plotted with respect to impact parameter. Gaussian fits omit the first bin.

The physics which changes the width of the real data with respect to centrality appears not to exist in the HIJING-modeled data. There may be concern that perhaps the width change in the data could be due to change in centrality of the data. However, the HIJING-GEANT events have a wide range of centralities and impact parameters and have the same balance function shape and width. The GEANT + TRS simulator for STAR has shown to be accurate as discussed in Section 6.1.2. In a purely physical way, different multiplicities can be studied by simulating events with specific number of particles, and compare the balance functions, which is done in Section 6.3, with the Bjorken Thermal model.

As the four centralities of HIJING-GEANT simulated events have the same balance function shape and width, they can be combined together and represent one measurement. This increases the statistics for the HIJING-GEANT measurement, as can be seen in Figure 6.6 a), which shows the charged particle pair balance function for all HIJING-GEANT events. Figure 6.6 b) shows the Gaussian fit for this balance function omitting the first bin.

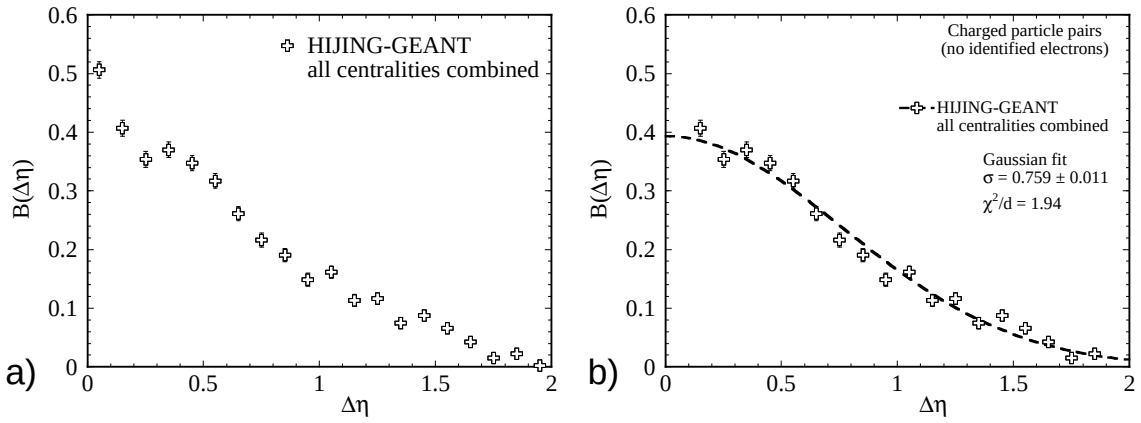

Figure 6.6: a) HIJING-GEANT all centralities combined charged particle balance function. b) The same with a Gaussian fit excluding the first bin.

6.1.4 Pion Pairs

Before using all HIJING-GEANT centralities combined into one, the pion pair balance function must be checked. The balance function for pion pairs with all centralities for HIJING-GEANT simulations is shown in Figures 6.7 a) and b). The same balance function with a Gaussian fit excluding the first two bins, and the fit widths is shown in Figures 6.8 a) and b). The weighted average widths are shown in Figure 6.9. Figure 6.10 shows the Gaussian fit widths, with both the Gaussian and weighted average widths calculated omitting the first two bins. From examining these plots, it can be seen that the pion pair balance function calculated from HIJING-GEANT simulations at different centralities have the same shape and width within statistical error bars. Thus, the method of combining all the centralities may again be used for HIJING-GEANT analysis.

The pion pair balance function for all HIJING-GEANT events as a function of Δy is shown in Figure 6.11 a), with the Gaussian fit excluding the first two bins as in the data analysis in Figure 6.11 b). The dip near $\Delta y = 0$ is not seen in these events. The HIJING simulator does not include the HBT like-charge interactions. Thus, the omission of the first two bins for the balance function width calculation is essential to compare the simulated calculations with the real data.

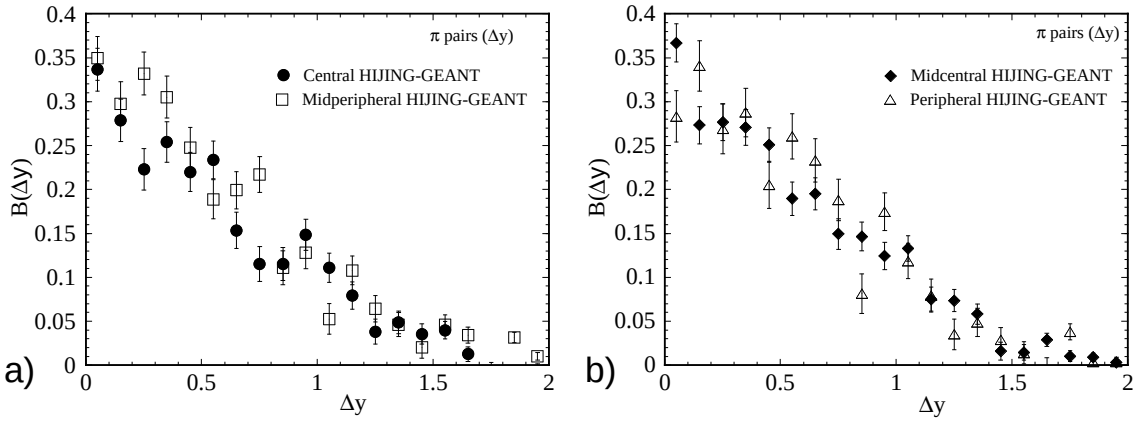

Figure 6.7: a) HIJING-GEANT central (circles) and midperipheral (squares) pion pair balance function, b) midcentral (diamonds), and peripheral (triangles) pion pair balance function.

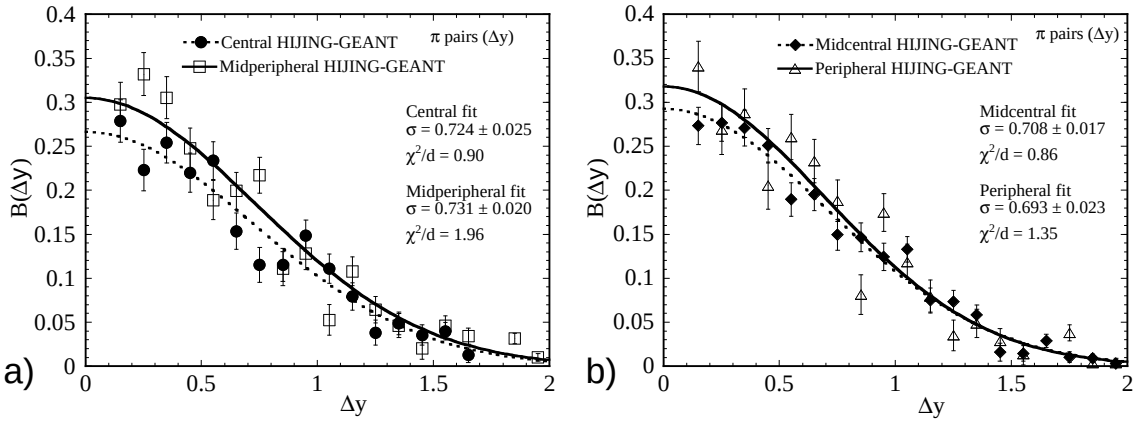

Figure 6.8: a) HIJING-GEANT central (circles) and midperipheral (squares) charged particle balance function, b) midcentral (diamonds), and peripheral (triangles) charged particle balance function. Gaussian fits are shown excluding the first two bins from the fit.

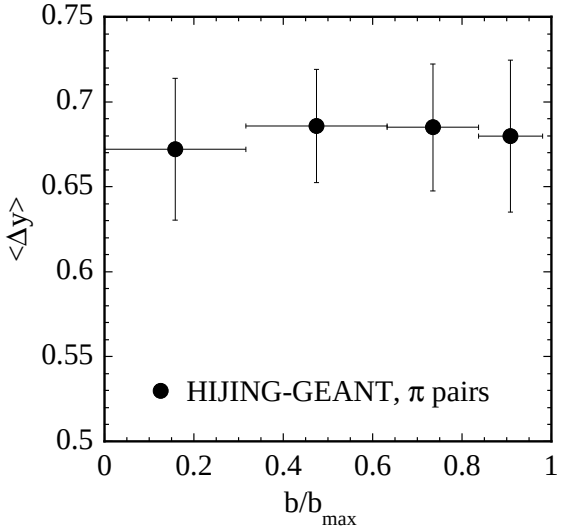

Figure 6.9: Summary of widths of pion pair balance functions for the four centrality bins of HIJING-GEANT, plotted with respect to impact parameter.

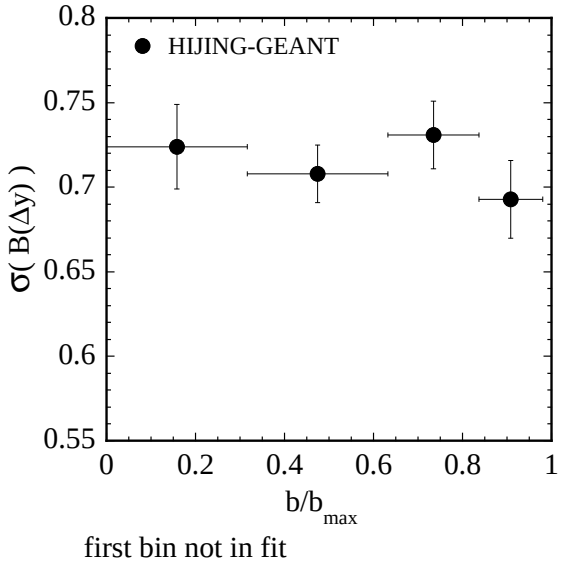

Figure 6.10: Summary of Gaussian fit widths of pion pair balance functions for the four centrality bins of HIJING-GEANT, plotted with respect to impact parameter. Gaussian fits omit the first two bins.

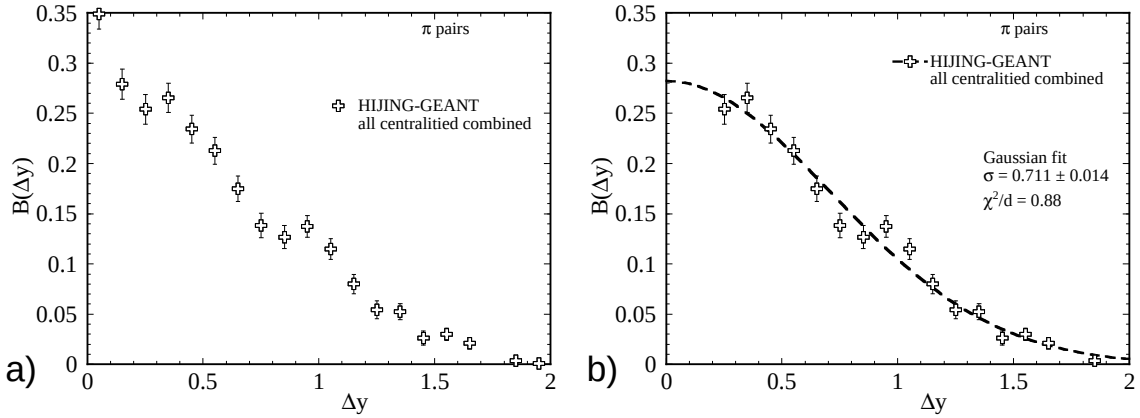

Figure 6.11: a) HIJING-GEANT all centralities combined pion pair balance function. b) The same with a Gaussian fit excluding the first two bins.

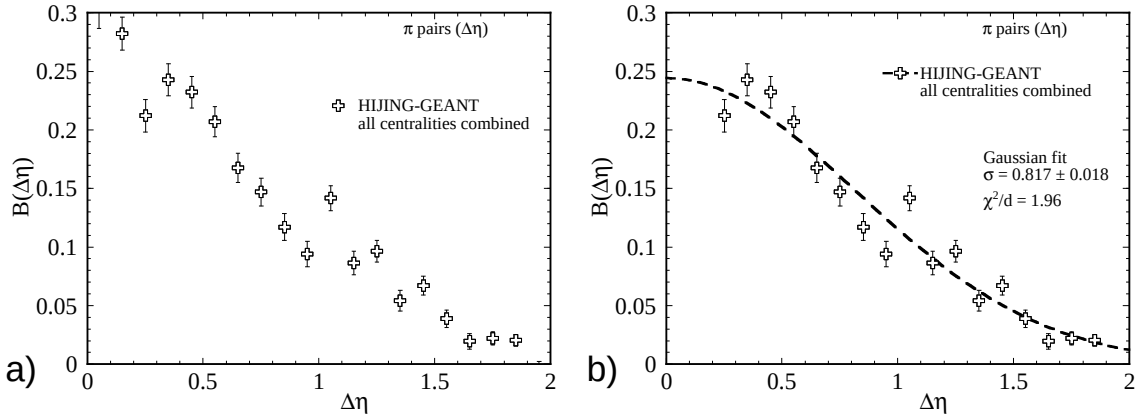

Figure 6.12: a) HIJING-GEANT all centralities combined pion pair ($\Delta\eta$) balance function. b) The same with a Gaussian fit excluding the first two bins.

The pion pair balance function measured with respect to $\Delta\eta$ for HIJING-GEANT simulated data is shown in Figure 6.12 a), with a Gaussian fit omitting the first two bins in Figure 6.12 b). The low statistics in the HIJING-GEANT set is more evident in the $\Delta\eta$ pion pair balance function than the Δy. This measurement will be a useful comparison to similar data measurements, although it appears that the pion pair balance function measured with respect to Δy gives smoother results for these simulated events.

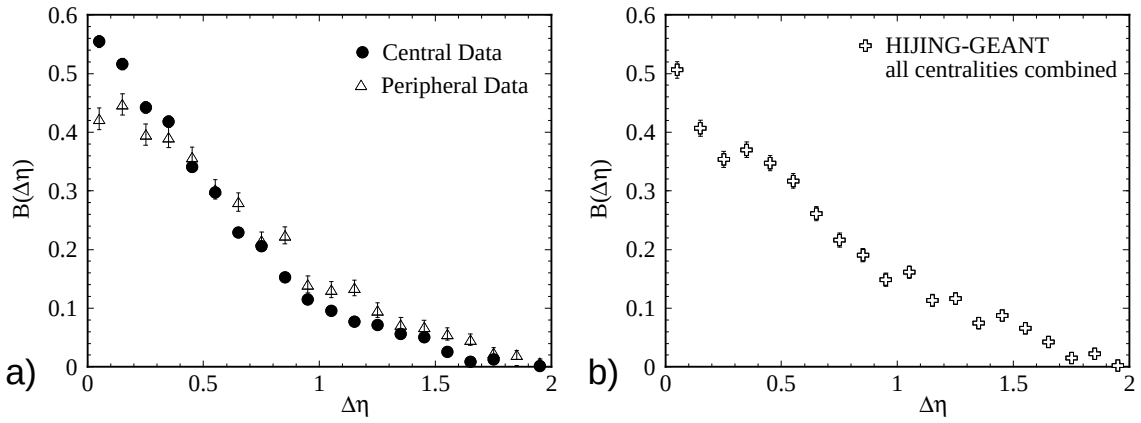

Figure 6.13: Charged particle pair balance function for a) central(circles) and peripheral(triangles) data, as well as b) HIJING-GEANT (plusses) simulated events.

6.1.5 Comparison With Data

In comparing HIJING-GEANT events with the real data, some features about the physics underlying the collisions may be evident. Recall that HIJING does not include final state interactions. However, those interactions would broaden the balance function, so that HIJING-GEANT simulations shown represent the narrowest broadening. Other factors include that HIJING does not have HBT and the GEANT/TRS combination of software does not include track splitting and merging which exist in the real data. However, these effects would only affect the balance function at small $\Delta\eta$ or Δy. By omitting the low $\Delta\eta$ or Δy bins in the balance function analysis, these effects can be left out. Other concerns involve that HIJING over-estimates the multiplicity of the event, however it has been shown that the balance function shape and width depends upon the underlying physics of the particle model rather than the multiplicity as will be discussed in Section 6.3.

For the charged particle pair balance function, Figures 5.2 and 6.6 can be qualitatively compared, they are reproduced in Figure 6.13 a), and b) respectively. Figure 6.13 b) shows that the simulated events have a lower initial balance function ignoring the electron contamination remaining in the first bin, and fall off less rapidly at higher Δy than the data.

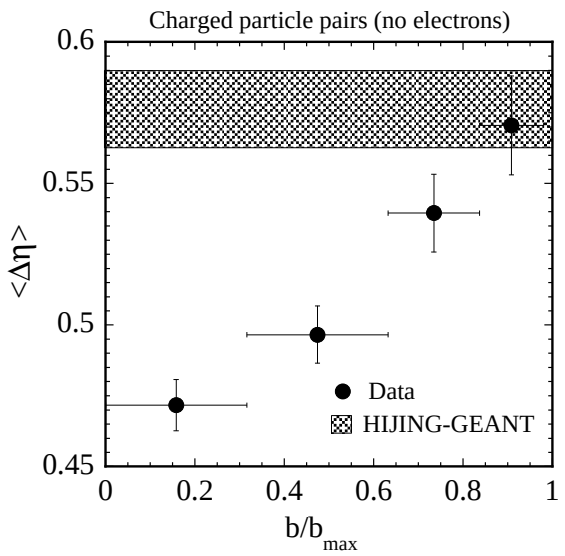

Figure 6.14: Summary of widths of the charged particle balance functions for the four centrality bins of data (circles), with HIJING-GEANT represented by the shaded band.

For a quantitative comparison, the widths of the balance functions may be plotted. Figure 6.14 shows an overlay of the weighted average width of the balance function for data at the four centralities and for HIJING-GEANT. The simulated HIJING-GEANT events and their statistical error are represented by the shaded bar, which matches the prediction that this hadron gas model would have the same balance function for all possible centralities. Figure 6.15 shows the Gaussian fit widths from the balance functions of data and HIJING-GSTAR.

In studying Figures 6.14 and 6.15, it seems that the peripheral data set has a balance function width which is near, if not consistent to that of HIJING-GEANT simulated events. This, combined with the observation of balance function width narrowing with more central events suggests that the peripheral data contains hadron gas-type events, whereas the central data is made up of QGP events. Note that this conclusion is dependent upon the assumptions of the models discussed in reference [47]. However, even the centrality-dependent widths in the data does indicate some sort of interesting difference between peripheral and central data sets. Whether or not the events are QGP, the measurements indicate a delayed hadronization. This means

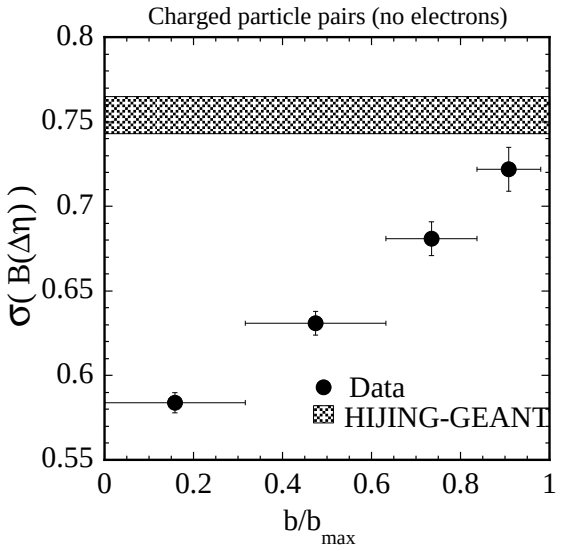

Figure 6.15: Summary of Gaussian fit widths of the charged particle balance functions for the four centrality bins of data (circles), with HIJING-GEANT represented by the shaded band. Gaussian fits are done omitting the first bin.

that there is a period of time after the collision before the charges are created, with this time being longer than the hadron gas hadronization time of 1fm/c.

Moving onto the pion pair balance function, the weighted average widths are shown in Figure 6.16. The actual balance function shapes when compared do not show that HIJING-GEANT events are lower than data near $\Delta y = 0$, however this is not unexpected in consideration of the dip in the data in that region due to HBT, which HIJING does not have.

The Gaussian fit widths for HIJING-GEANT and the data are shown in Figure 6.17. For the pion pair balance function calculated with respect to Δy, the peripheral events have a width consistent/near to that of HIJING-GEANT simulations. Again, the central events have a narrower balance function compared to the peripheral, with the width changing smoothly with respect to centrality. This agrees with the predictions in reference [47] for hadron gas peripheral events and central events having delayed hadronization as in a QGP model.

The pion pair balance function measured with respect to $\Delta\eta$ instead of Δy widths

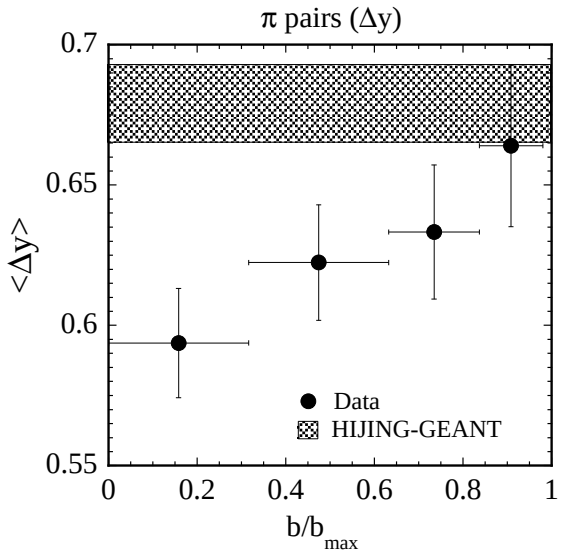

Figure 6.16: Summary of widths of the pion pair balance functions for the four centrality bins of data (circles), with HIJING-GEANT represented by the shaded band. Weighted average widths are calculated excluding the first two bins.

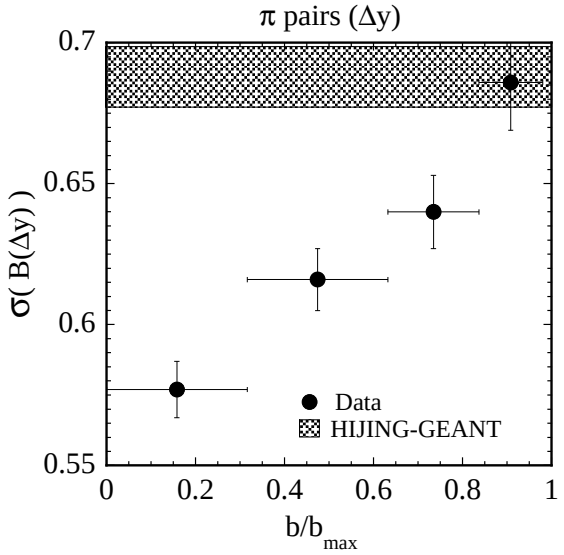

Figure 6.17: Summary of Gaussian fit widths of the pion pair balance functions for the four centrality bins of data (circles), with HIJING-GEANT represented by the shaded band. Gaussian fits are done omitting the first two bins.

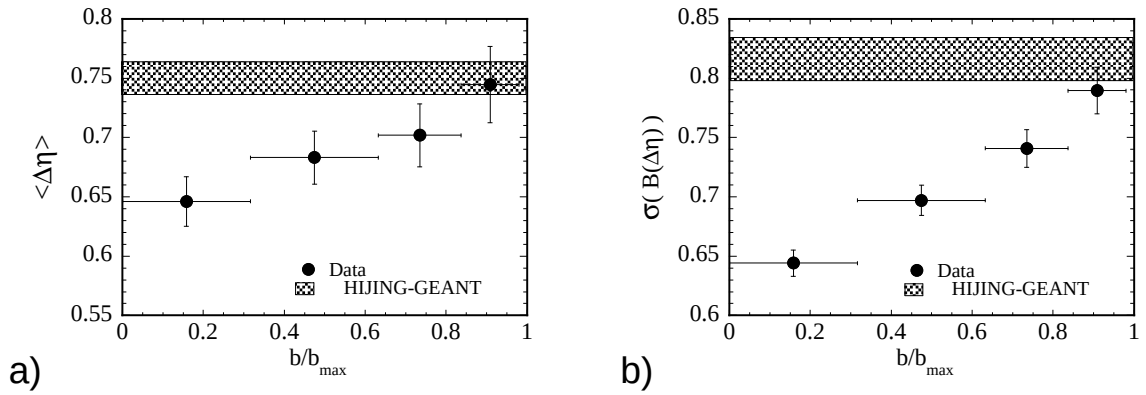

Figure 6.18: Summary of widths of the pion pair ($\Delta\eta$) balance functions for the four centrality bins of data (circles), with HIJING-GEANT represented by the shaded band. a) Weighted average widths are calculated excluding the first two bins. b) Gaussian fit widths are shown, with the first two bins omitted from the fit.

are shown in Figure 6.18 a). The Gaussian fit widths are shown in Figure 6.18 b). Even when the momentum dependence in the rapidity is removed, the same behavior of the balance function widths is evident.

6.2 Fast Pseudorapidity Simulator

The second simulator used was a fast STAR pseudorapidity acceptance filter. This filter, written for the purpose of this dissertation, uses the pseudorapidity, dN/dη, distribution of actual STAR data. This distribution was found for 40 different types of events, in four centralities discussed in Section 2.4, and 10 vertex bins. The vertex bins divided up the possible z vertices from -75 cm to 75 cm, centered around the $z = 0$ vertex. These different event types were necessary to reflect the different dN/dη distribution profiles for a variety of possible events measured. Given the known efficiency of STAR for the data set used as 85% within $|\eta| < 0.5$ [37], these dN/dη distributions are normalized to be efficiency distributions for particles accepted in the detector. Events from a simulator (HIJING or Bjorken thermal) are randomly assigned a vertex based upon actual central data vertex probability, as seen in Figure 4.4 a). The particles of those events are assigned a random number which is checked

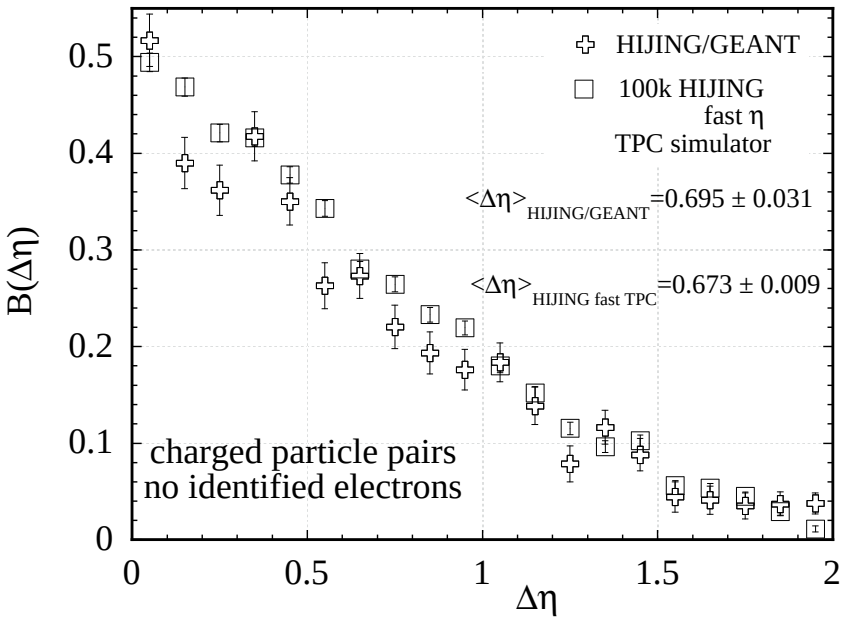

Figure 6.19: Charged particle pair balance function plotted for HIJING-GEANT (plusses), and HIJING events with the fast η-dependent TPC simulator(squares).

against the probability of the particle surviving, given its pseudorapidity.

6.2.1 Comparison With HIJING Through GEANT

To check that the fast pseudorapidity simulator is effective for the balance function, it can be compared with HIJING events with the same parameters which have been run through the STAR detector simulation of GEANT (GSTAR + TRS). The balance function for the fast η and the GEANT detector simulators is shown in Figure 6.19. It can be seen that the balance functions have the same width within the statistical error bars. As another check, the p, p_t, and dN/dη distributions for the two types of events were compared. These were also compared to the data to check quality. The distributions had the same overall shape and behavior as expected. The fast simulator correctly reproduces the shape of each dN/dη distribution for a specific vertex bin.

As GEANT and TPC reconstruction take a large amount of disk space and time to run, having this fast pseudorapidity-based TPC simulator allowed for quick analysis of the effects of the detector on various simulation models. The detector acceptance

effects are also studied with analysis done on the real data, as covered in Chapter 7. Other than HIJING, the Bjorken thermal model was used to attempt an understanding of the balance function measurements on the STAR year 2000 data.

6.3 Bjorken Thermal Model

The Bjorken thermal model, introduced in Section 3.1, was also used as a theoretical comparison to the measured data. This model is intended as a simple picture of a QGP creation, useful in balance function measurements. The model creates only pion pairs and is not intended as a generalized event generator. Other QGP simulators [26] exist to model before, during, or after heavy-ion collisions. These models produce predictions for many of the common observables in heavy-ion collisions. However, there is no simulator that models the complete collision from start to finish, with the output of observed particles in an event-by-event format [26]. The Relativistic Quantum Molecular Dynamics (RQMD) [68] model is popular in heavy ion physics for modeling a hadron gas. RQMD simulations show a hadronic gas balance function width that is significantly wider than other models, which is the opposite behavior than what is measured [69].

Thus, the Bjorken simulator is the best model at hand for this balance function study. In comparisons to data, it is important to remember that the Bjorken model does not contain much of the physics that occurs in a heavy ion collisions. Rather, this model can be used as a limit on the balance function width, representing all the charge made at breakup. Modifications and variations to this Bjorken model are discussed in the following sections.

The physics quality of the Bjorken simulator can be seen with the typical η and momentum histograms. Figure 6.20 shows a comparison of the pseudorapidity histogram a) with a perfect detector before, and b) after the fast TPC simulator. The shape of the η histogram from the simulator is similar to that of the central data set,

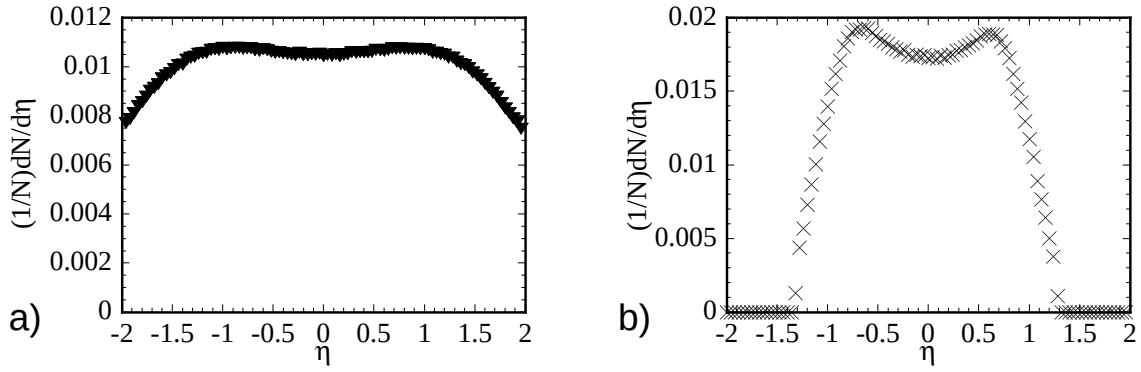

Figure 6.20: Pseudorapidity histogram of Bjorken thermal model simulations a) with a perfect detector before and b) after the fast η TPC simulator.

and the histogram before the simulator is smooth and reasonable. However, when the balance function for the Bjorken model is compared to data, the peak and integral will be much higher for the Bjorken model. This reflects the all-pion nature of the balancing charge the model produces. The width of the function remains meaningful for comparison, as can be understood if a fraction of the charge produced were to be randomly removed. This is similar to the fast TPC simulator randomly removing tracks based on η. The overall effect is to reduce the height and integral of the Bjorken balance function, but the width relative to HIJING remains the same. For a comparison using a perfect detector, Figure 6.21 shows the pion pair balance function for Bjorken and HIJING events, with and without Gaussian fits. It is clear that the Bjorken balance function is narrower than HIJING, even limiting the Gaussian fit to Δy of 2.0. Here, all bins are used in the Gaussian fit as neither model contains HBT interactions.

6.3.1 Bjorken Model Parameters

The Bjorken thermal model has a few variables that the user can control to simulate specific physical conditions of the particle hadronization. The default parameters are $\tau_i = 9fm/c$, $T_i = 225MeV$, $T_f = 120MeV$, and number of collisions is 3. The first parameter, τ_i is the time at which the particles begin to hadronize. This model as-

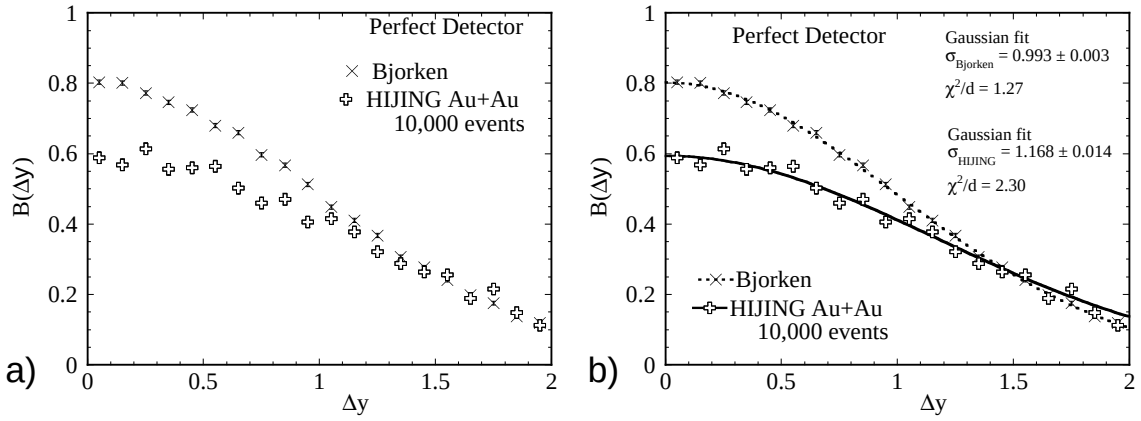

Figure 6.21: a) Pion pair balance function (Δy) for Bjorken (x's) and HIJING (plusses) simulations in a perfect detector. b) is the same with Gaussian fits.

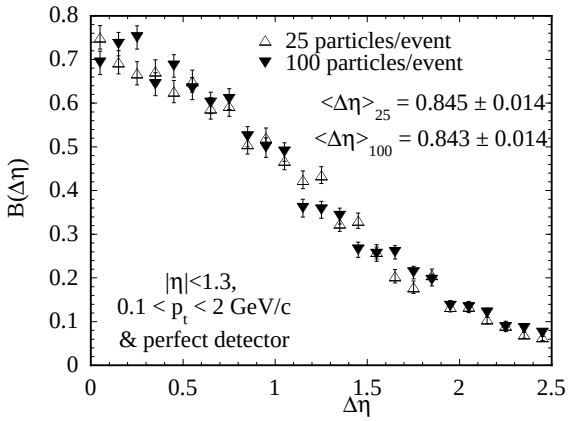

Figure 6.22: Charged particle pair balance function plotted for Bjorken simulated pion pair events with a perfect detector and physical cuts. Open triangles represent 25 particles per event and closed triangles are 100 particles per event.

sumes that the pions were creates with local charge conservation at the time τ_i and a temperature of T_i. Over a period of time, specified by T_f and a cooling rate of 7.5 MeV/(fm/c) [47], the hadronized particles have a chance to interact with other hadrons in the expanding, cooling cylinder. This interaction is controlled by 3 collisions per particle on average. The 3 collisions per particle is another option which was not varied in these studies. The final time, after which the particles no longer interact is τ_f, which is calculated by $1 + (T_i - T_f)$/cooling rate. For the default parameters given, this gives a τ_f of 15 fm/c.

Bjorken simulations shown below have 100,000 events. Each set of events has

100 particles per event in the data set. It was found that the shape and width of the balance function did not depend on the number of particles per event used in construction. Figure 6.22 shows the charged particle balance function for Bjorken simulated events in a perfect detector with the addition of two geometry cuts similar to those placed upon data. The two different multiplicity data sets have the same balance function. In the following sections, if a parameter value is not defined, it can be assumed to have the default settings, as described previously.

6.3.2 Varying Temperature

The first parameter varied in comparison to data was the temperature. In reference [47], temperatures of 165 and 225 MeV are used, producing slightly different balance functions. Here, the fast η TPC simulator was used to enable a comparison of the balance function width to the data. Figure 6.23 shows the widths of the Bjorken balance function for varying temperatures. The x-axis has arbitrary placement, with the Bjorken measurements staggered to display the results. Here, only the first bin was omitted from the weighted average. Since the initial time and final time remain the same ($\tau_i = 15, \tau_f = 9 fm/c$), as well as the cooling rate of 7.5, both final and initial temperatures are modified. It can be seen that a set of temperatures which is unreasonably low would have a balance function width similar to the data.

6.3.3 Varying Time

The next variation was of the initial time, τ_i. The varying temperature was covered in reference [47], while variations on the initial time were not. In some ways, the "initial time variation" is built into the model, as it models a QGP. A hadron gas is theorized to hadronize at an initial time of 1 fm/c after the collision. A QGP is theorized to hadronize at a later time after existing in plasma state for some time. The length of that plasma state is unknown, as is the length of time during which the particles

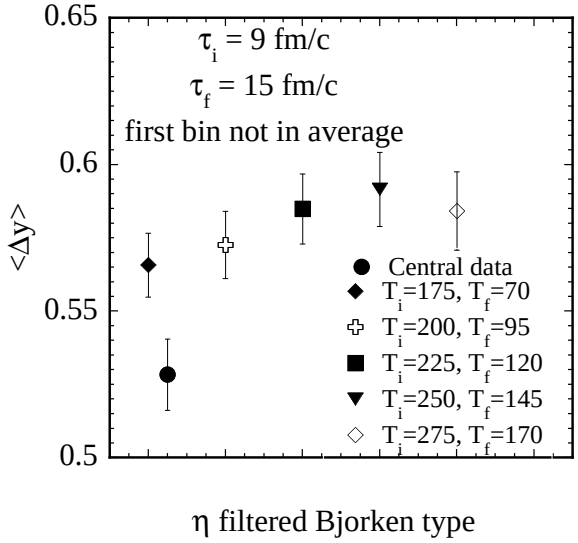

Figure 6.23: Pion pair balance function widths plotted for Bjorken events processed through the fast η simulator with varying temperatures. The central data width (circles) calculated without first bin is shown for comparison.

hadronize and interact. If τ_i is early, there is more time for particles to diffuse in the medium. An early τ_i also means that there is a larger velocity gradient. The balance function widths calculated with all bins for varying times in a perfect detector are shown in Figure 6.24. It can be seen that with later initial times and thus, shorter hadronization times before τ_f of 15 fm/c, the balance function width narrows.

The balance function widths for Bjorken thermal simulations with varying times were also calculated for the fast η TPC simulator. The pion pair balance function widths are shown in Figure 6.25, with a shaded band representing the central data width. Widths shown are calculated with the first bin omitted. As with the perfect detector, the later initial times show balance function widths which approach the narrowness of the data. However, the data still shows a narrower width than the Bjorken model simulated with the η TPC filter.

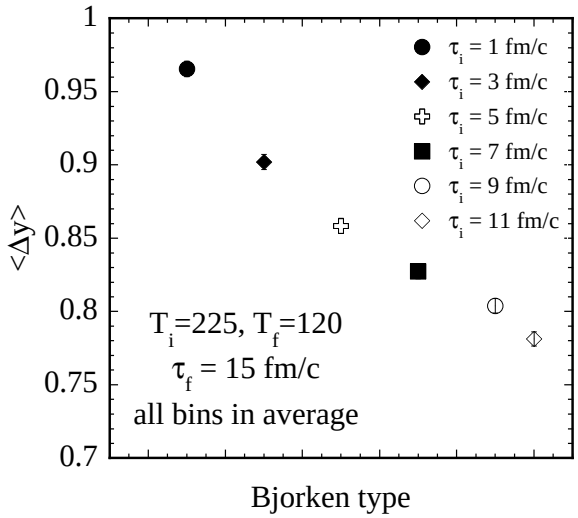

Figure 6.24: Pion pair balance function widths plotted for Bjorken simulated for a perfect detector with varying initial times. The widths are calculated with all bins of the balance function.

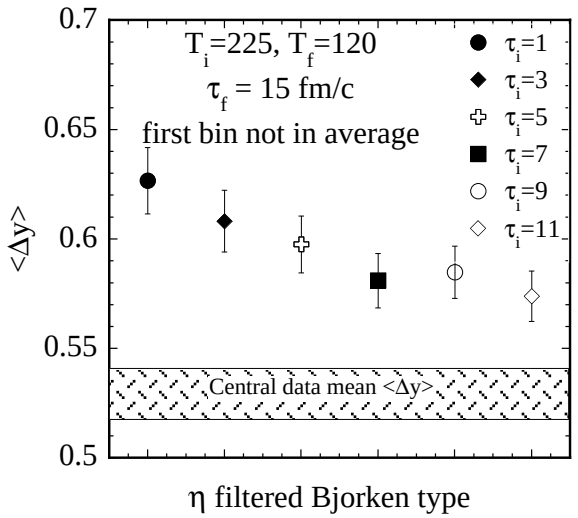

Figure 6.25: Pion pair balance function widths plotted for Bjorken events processed through the fast η simulator with varying initial times. The central data width (shaded bar) calculated without first bin is shown for comparison.

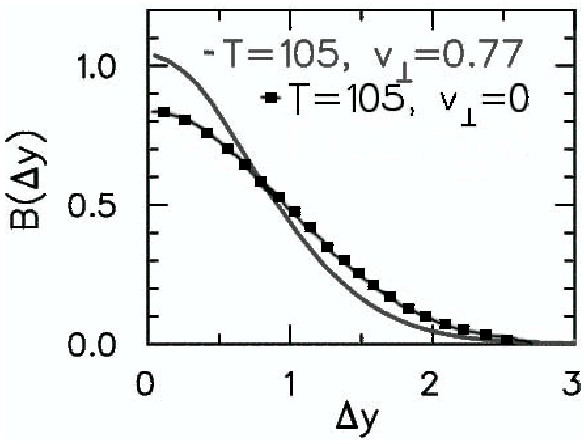

Figure 6.26: Pion pair Bjorken thermal model balance function calculated by Pratt with (line), and without (box and line) flow [70].

6.3.4 Flow

It was a concern that the data showed too strong of an effect with the central data being more narrow than any reasonable Bjorken thermal model calculations. Pratt [70] showed that the inclusion of radial flow into the Bjorken model narrows the balance function for pion pairs significantly. Flow is a term for both a measurement and a behavior of the system after the collision. It describes the collective motion of the particles. Figure 6.26 shows the calculations for the pion pair balance function of the Bjorken thermal model both with and without flow. The line curve includes an extra boost of radial flow, indicated by the transverse velocity given in the figure.

These calculations show that a model incorporating radial flow and a constraint that the particles are emitted from the same point in space-time can reproduce the observed narrow widths in central collisions. This type of calculation represents the narrowest possible balance function.

6.4 Simulations Summary

The simulations shown here provide a useful comparison to the data. The HIJING-GEANT balance functions for both charged particles and pions have widths which are

consistent with the most peripheral of the measured data from 2000. This supports the notion that the peripheral events contain events which are like a superposition of nucleon-nucleon interactions. The most central events which are narrower than both HIJING-GEANT and the peripheral data appear to indicate late hadronization.

In comparison with the Bjorken thermal model, there are a number of features which arise. Primarily, there are many parameters within the Bjorken model which can be changed to widen or narrow the balance function. However, with parameters similar to HIJING ($\tau_i = 1 fm/c$), the balance function has a width that is close to that of HIJING when comparing analysis with a perfect detector. Reasonable sets of parameters for the Bjorken model narrow its balance function prediction. However, the data remain narrower than these predictions.

Preliminary studies indicate that the addition of flow in the Bjorken thermal model narrows the balance function to a width which is consistent with the central data. This comparison shows that the data results are not physically unreasonable. The behavior of flow and the Bjorken model indicates that flow without the formation of a quark-gluon plasma would not provide the narrowing of the balance function seen in the central data compared to the peripheral data. More simulations are needed together with analysis of other signatures for the QGP to fully explain these balance function measurements, as discussed in Chapter 8.

Chapter 7

Understanding the Detector Acceptance in the Measurement

Model calculations cannot be compared directly to STAR experimental results without taking into account the acceptance of STAR. One could also attempt to correct the measurements for the known acceptance and compare directly to the theoretical model. The approach used in this dissertation is to present the experimental results without correction and to filter the model calculations through the acceptance of STAR.

7.1 Mixed Events

A method to determine the background of an observable in analysis is to use mixed experimental events and compare these to the real events [71]. In reference [71], aspects of event-by-event analysis are discussed. For example, when studying momentum fluctuations of an event sample, events are compared with mixed events. The mixing of the events in this case would be drawing independent samples from a set of events and make a comparison to those events. In this and other observables, the mixed event measurement represents a sort of background to compare to the data. It is not

immediately clear in balance function analysis for heavy ion physics what the mixed events would represent, or even if there is a background that can be obtained. All the mixed event analyses to be discussed in Section 7.1 were done with a smaller subset of the complete analyzed data, that of the P00hi production library data. Charged particle analysis is done excluding identified electrons, as in Section 5.2.

7.1.1 The Traditional Method

The usual method in event-by-event analyses is to create mixed events which are comprised of tracks from real events. The necessity of these events to be of similar type has been documented [72]. The method used here was to divide the data into 40 event subsets. Of those, there are four possible centrality bins, and ten possible vertex bins, with the middle vertex bin being centered at zero. For these mixed events, the top 10% central events were used, and events were mixed within vertex bins. New mixed events were created by taking ten tracks randomly from each of one hundred events. The new events have 1000 tracks. The centrality cut specifies that these would normally be tagged as midcentral events, however the centrality cut is based upon total good primary tracks detected and not merely those which survive the more stringent analysis track selection. In general, events with 1000 or more primary tracks that survive cuts are tagged as central events. Figure 7.1 shows the charged particle balance function without electrons for 10,000 of these traditional mixed events. The balance function of mixed events is statistically consistent with zero.

For the pion pair balance function, the mixed events is shown in Figure 7.2. The pion pair traditional mixed events data appear to have a balance function varying near zero, however, the behavior at low Δy may signify a background that affects the balance function measurements. To check this, these mixed event balance function values can be subtracted from the measured balance function for pion pairs. The data balance function minus mixed events balance function for central and peripheral

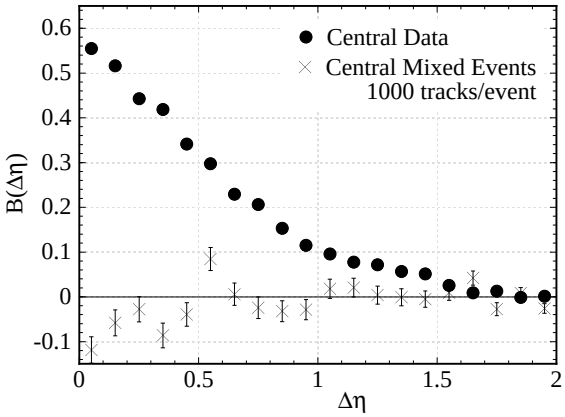

Figure 7.1: Charged particle balance function. Central data are dots, traditional mixed events are represented by x's.

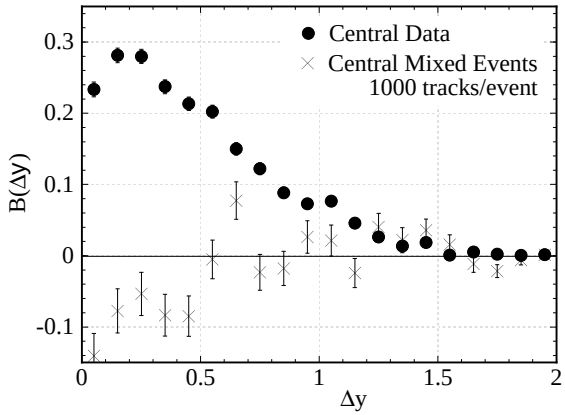

Figure 7.2: Pion pair balance function. Central data are dots, traditional mixed events are represented by x's.

pion pairs is shown in Figure 7.3.

The widths of the balance function for different centralities of pion pair balance functions minus mixed event is shown in Figure 7.4. The relative increase in the balance function widths is similar to that seen from the systematic error estimate. Thus, considering the systematic and statistical error bars, there is a near zero value of the balance function for mixed events. Thus the traditional mixed events gives a balance function of zero for both charged particle and pion pairs.

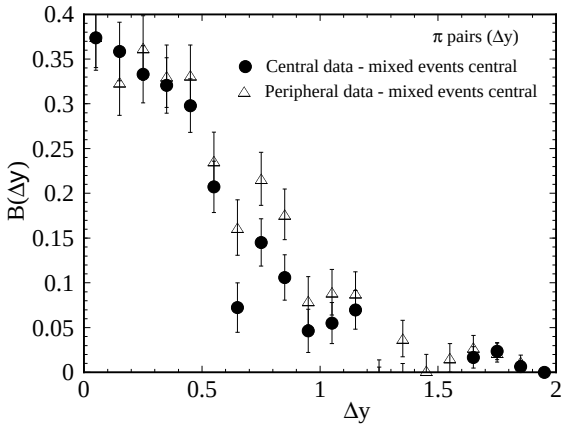

Figure 7.3: Pion pair mixed event balance function subtracted from the pion pair balance function. Central data are dots, peripheral events are triangles.

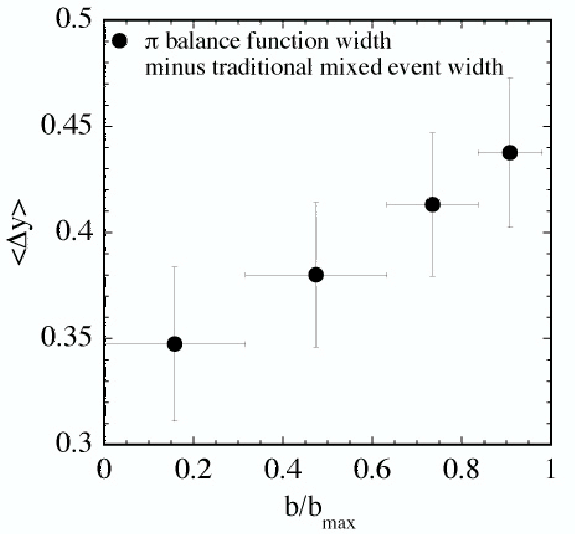

Figure 7.4: Pion pair mixed event balance function subtracted from the pion pair balance function. Widths of data are plotted with circles.

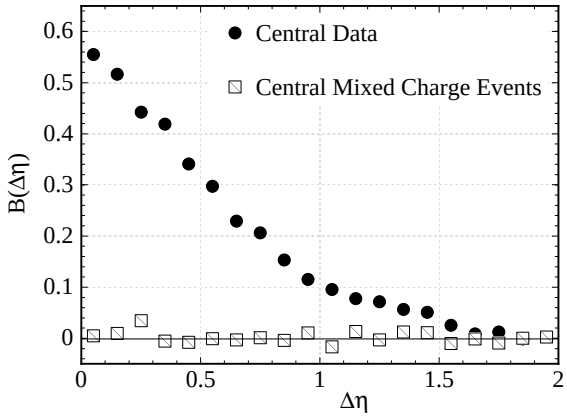

Figure 7.5: Charged particle balance function. Central data are dots, mixed charge events are represented by squares with slashes.

7.1.2 Mixing Charges

Given that the balance function measures the relation of co-created particle pairs in terms of their electric charge, the next mixing method used was to randomize the charge in the events. For this method, new data sets were created based upon the measured data, where the particle type, momentum, and pseudorapidity were all kept. However the charge of the particle was randomized, with a small weight towards positive charge, reflecting the measurement of 2.8% more positive than negative charges. The charged particle balance function for all central events with randomized charge is shown in Figure 7.5. Again, the balance function of mixed charge events is statistically zero. With the charge information removed from the tracks, the balancing pair information is completely destroyed.

7.1.3 Mixing Pseudorapidity

The other main variable used in the charged particle balance function is pseudorapidity. The next mixed event method attempted was to mix the pseudorapidity of the detected particle tracks. The pseudorapidity was mixed by randomizing it over all particles in a given event. The particles were read in by the program, storing each of the recorded particle features in a one-dimensional array. Particle information is then

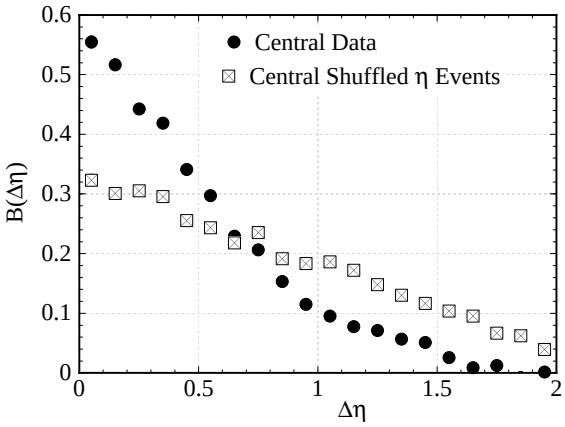

Figure 7.6: Charged particle balance function. Central data are dots, shuffled η events are represented by squares with x's.

written to file with the same particle identification, charge, and momentum. However, the pseudorapidity is written from a randomly selected track, with no two randomly selected ηs being from the same track. In this way, the pseudorapidity of the tracks within an event are shuffled. The charged particle balance function for central shuffled pseudorapidity events is shown in Figure 7.6.

This balance function has a shape and width. Its height at $\Delta\eta = 0$ is much lower than both the data and HIJING-GEANT measurements. The width of this shuffled η balance function is much wider than both data and HIJING-GEANT balance functions. This comparison shows that the balance function measurements are indeed a clear physical signal. The summary of the widths of these different balance functions can be seen in Figure 7.7. For the mixed pseudorapidity, there is no statistical difference in the width over the different centralities. This reaffirms the observation, covered in Section 6.3, that the balance function measurement differences seen in the data are not multiplicity dependent.

Shuffled events using HIJING-GEANT simulated data were also created. The charged particle balance function for HIJING-GEANT events, both regular and shuffled η is shown in Figure 7.8. The mixed η HIJING-GEANT balance function shape is similar to that of the shuffled η data, and the width is consistent within statistical

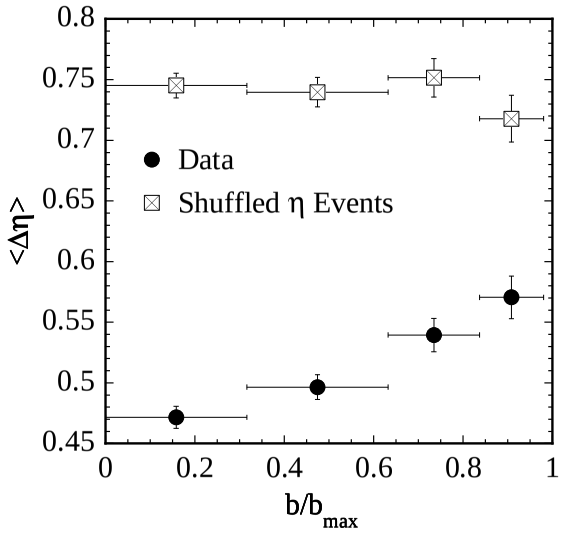

Figure 7.7: Charged particle balance function widths. Unmixed data are dots, shuffled η events are represented by squares with x's.

error bars.

The mixed pseudorapidity events show the effect of the detector acceptance on the balance function measurements. This can be illustrated in two possible ways. The first method is that of analyzing shuffled pseudorapidity events with the new or acceptance-removing normalization. The first method will be covered in Section 7.3. The second method is to analyze mixed η events for a perfect detector. This was achieved by taking pure HIJING simulated events and shuffling the ηs within them.

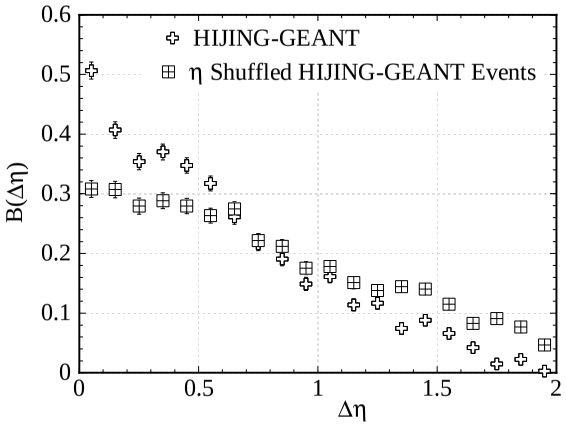

Figure 7.8: Charged particle balance function. HIJING-GEANT events are plusses, shuffled η events are represented by squares with +'s.

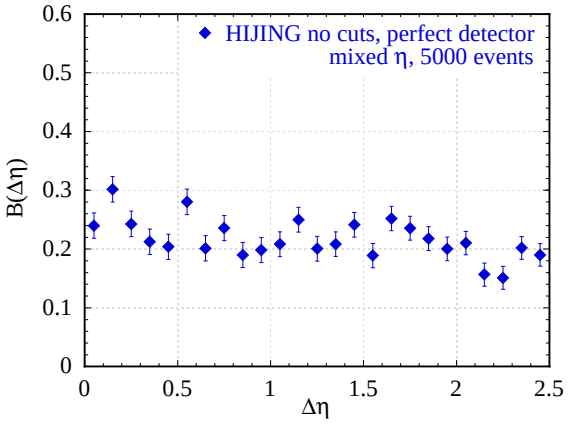

Figure 7.9: Charged particle balance function for HIJING events analyzed with a perfect detector, with shuffled η.

The mixed pseudorapidity events for HIJING in a perfect detector are shown in Figure 7.9. These perfect detector mixed η events should not be compared directly with those of the measured data or the simulated HIJING-GEANT events. However, the mixed pseudorapidity events for a perfect detector have a nearly flat shape over the region measured for the data. This balance function does reach zero at a large $\Delta\eta$, and it does normalize to one, as expected for a perfect detector. Thus, the contribution of a perfect acceptance is nearly flat in the $\Delta\eta$ region of this analysis.

The shape and slope of the shuffled η events illustrate the effect of the detector acceptance on the measured balance function. The balance function signal measured for both data and simulation is clearly different than this acceptance background.

7.2 Pseudorapidity Cuts

Pseudorapidity cuts are a useful technique to study the effects of the acceptance of the detector. This method involves measuring the balance function for different regions of symmetric η, while maintaining a full 2π coverage azimuthally. Due to the statistics of the 2000 data set, other cuts such as comparing two regions of transverse momentum space are not carried out. However, the pseudorapidity cut does illustrate the effect

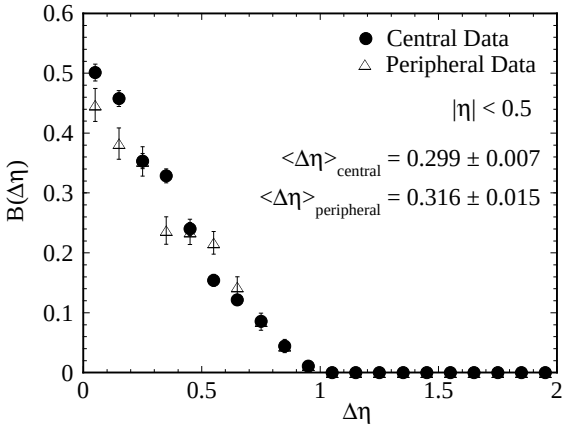

Figure 7.10: Charged particle balance function for central (circles) and midperipheral(squares) data, analyzed with particles that have $|\eta| < 0.5$.

of measuring the balance function in a physically smaller detector.

Figure 7.10 shows how the charged particle balance function for central and peripheral events is modified by using only charged particles with $|\eta| < 0.5$. The first bin was omitted from the calculation of the width. It is not possible in this case to have any $\Delta\eta$ greater than 1.0. However, it can also be seen that the central and midperipheral events are not statistically different in width for this region of detection. Theoretically, it is believed that to identify the fluctuations of a quark-gluon plasma, a region covering at least two units of rapidity or pseudorapidity is needed [44]. The lack of difference of the balance function width with respect to centrality is in contrast to the measurement shown in Figure 5.2. The balance function measured at different centralities with $|\eta| < 1.3$ shows a clear difference in width for different centralities.

The pion pair balance function for a detector covering $|\eta| < 0.5$ is shown in Figure 7.11. As in the charged particle plot, the widths, calculated without the first two bins, are the same for central and midperipheral events.

Comparing analyses with different pseudorapidity cuts, changes in the shape and width of the balance function are observed. To summarize the effect of the size in pseudorapidity on the balance function, the balance function widths will be shown. HIJING events are also shown for the different η cuts, these are the HIJING events

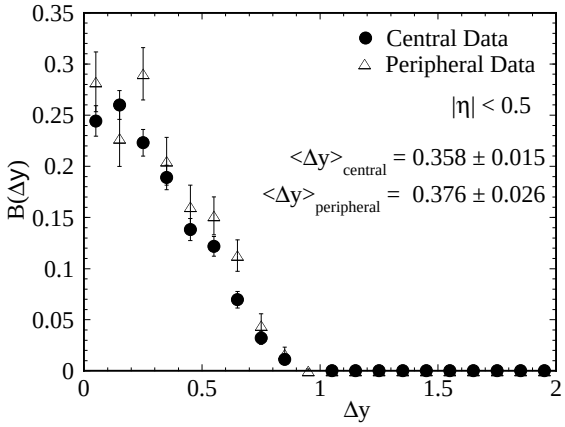

Figure 7.11: Pion pair balance function for central (circles) and midperipheral(squares) data, analyzed with pions that have $|\eta| < 0.5$.

which have been analyzed with both GEANT and TRS as discussed in Section 6.1. The balance function for these STAR-simulated HIJING events has a similar width change over pseudorapidity as the data, and as in Section 6.1.3, the HIJING events shown are analyzed including all four centralities in one simulated data set.

The charged particle balance function widths for data (circles), and HIJING-GEANT (shaded bar) in a TPC cut down to $|\eta| < 0.25$ is shown in Figure 7.12 a). Figure 7.12 b) shows the same information, except for a detector with a cut of $|\eta| < 0.5$. These plots are shown on the same scale to enable direct comparisons between different detector cuts, illustrating the change on all the balance function widths. The widths for $|\eta| < 0.75$ and $|\eta| < 1.0$ are shown in Figure 7.13 a) and b). Figure 7.14 shows the charged particle balance function widths for $|\eta| < 1.25$. These different pseudorapidity cuts cover five possible regions for balance function cuts in the STAR TPC. It can be seen, in comparing the widths on the same scale, that the balance function widens with larger acceptance. Also, acceptances larger than or equal to $|\eta| < 1.0$ show a significant difference in the charged particle balance function width between central and peripheral events.

The pion pair widths for data (circles), and HIJING-GEANT (shaded bar) in TPC cut to $|\eta| < 0.25$ is shown in Figure 7.15 a). Similarly, Figure 7.15 b) shows the

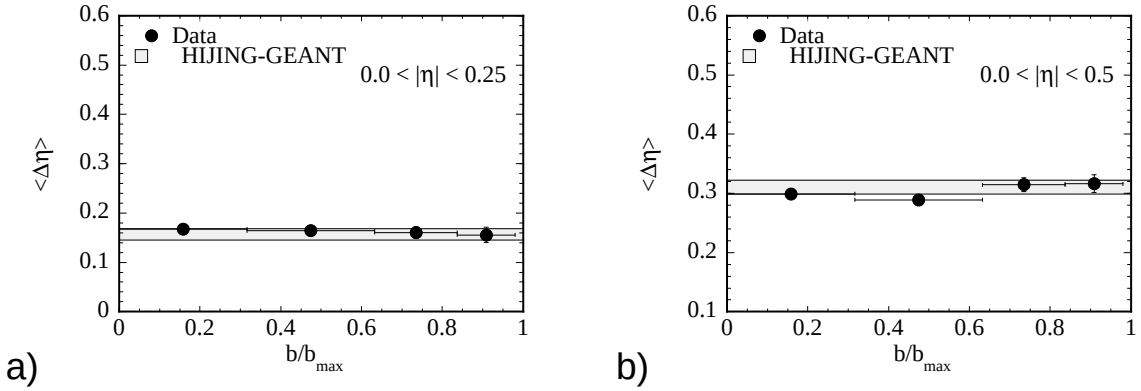

Figure 7.12: Charged particle balance function widths. Data (circles), and HIJING-GEANT (shaded bar) events are analyzed for particles with a) $|\eta| < 0.25$, and b) $|\eta| < 0.5$.

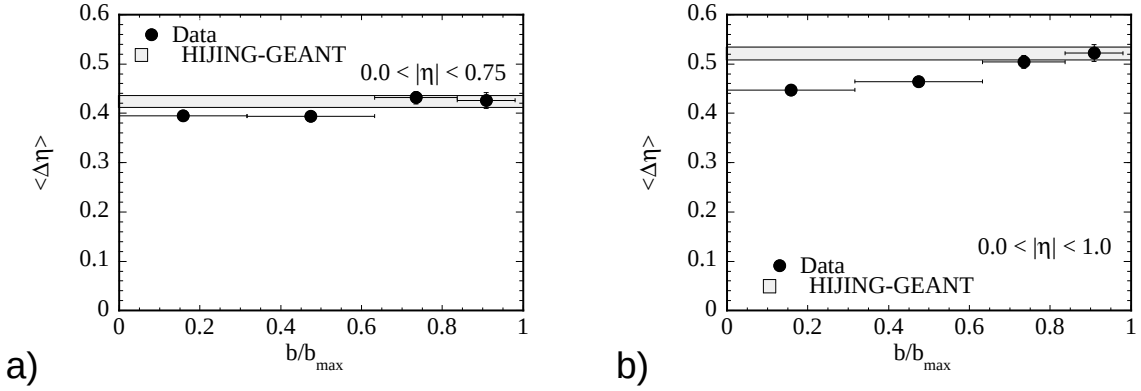

Figure 7.13: Charged particle balance function widths. Data (circles), and HIJING-GEANT (shaded bar) events are analyzed for particles with a) $|\eta| < 0.75$, and b) $|\eta| < 1.0$.

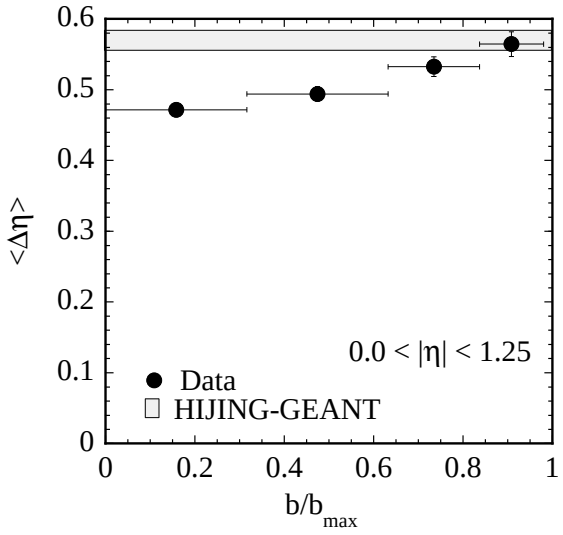

Figure 7.14: Charged particle balance function widths. Data (circles), and HIJING-GEANT (shaded bar) events are analyzed for particles with $|\eta| < 1.25$.

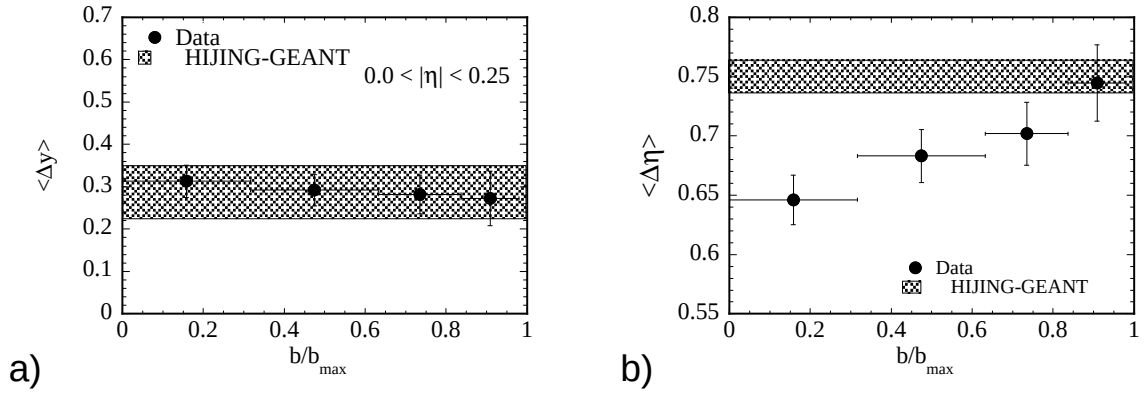

Figure 7.15: Pion pair balance function widths. Data (circles), and HIJING-GEANT (shaded bar) events are analyzed for particles with a) $|\eta| < 0.25$, and b) $|\eta| < 0.5$.

widths for $|\eta| < 0.5$, and 7.16 a) and b) show $|\eta| < 0.75$ and $|\eta| < 1.0$. The pion pair balance function widths are shown in Figure 7.17. Comparing the widths on the same $< \Delta y >$ scale, an effect similar to that seen in charged particle pairs is observed. The significant difference between central and peripheral pion balance function widths can be seen in a detector of $|\eta| < 1.0$ or larger.

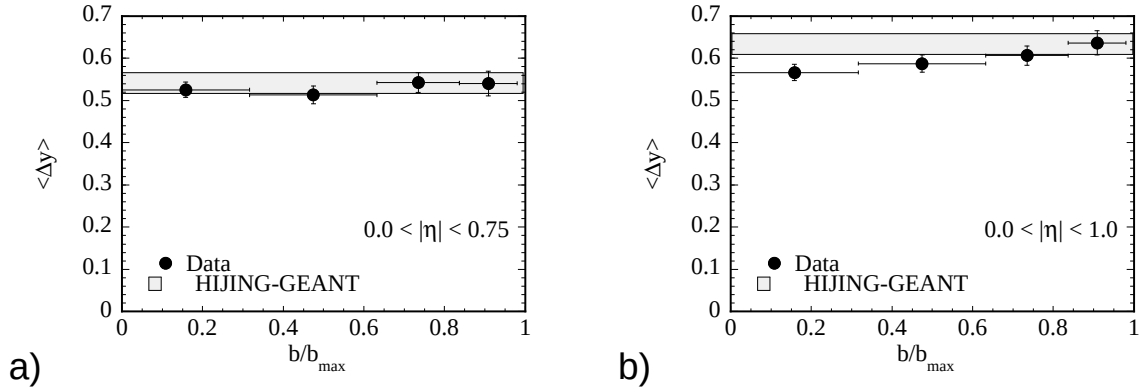

Figure 7.16: Pion pair balance function widths. Data (circles), and HIJING-GEANT (shaded bar) events are analyzed for particles with a) $|\eta| < 0.75$, and b) $|\eta| < 1.0$.

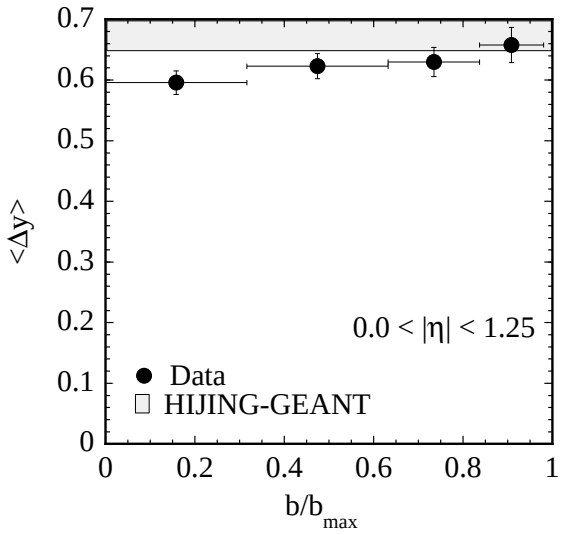

Figure 7.17: Pion pair balance function widths. Data (circles), and HIJING-GEANT (shaded bar) events are analyzed for particles with $|\eta| < 1.25$.

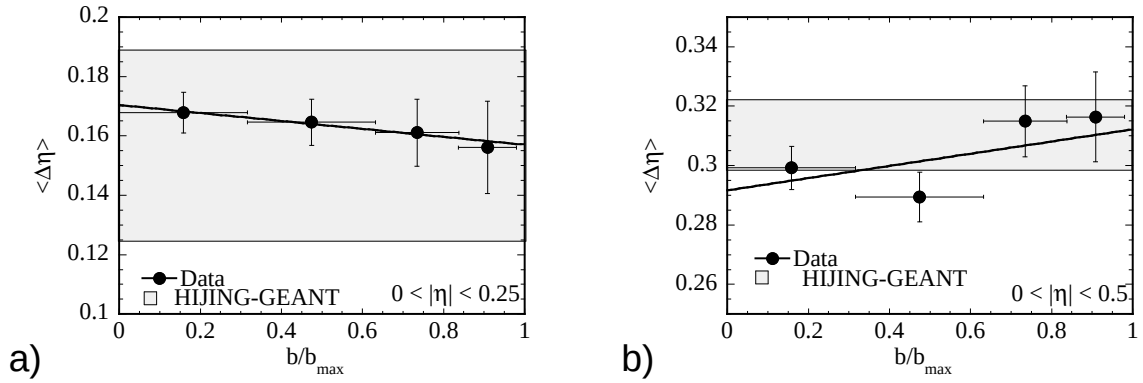

Figure 7.18: Charged particle balance function widths with a linear fit over centrality. Data (circles), and HIJING-GEANT (shaded bar) events are analyzed for particles with a) $|\eta| < 0.25$, and b) $|\eta| < 0.5$.

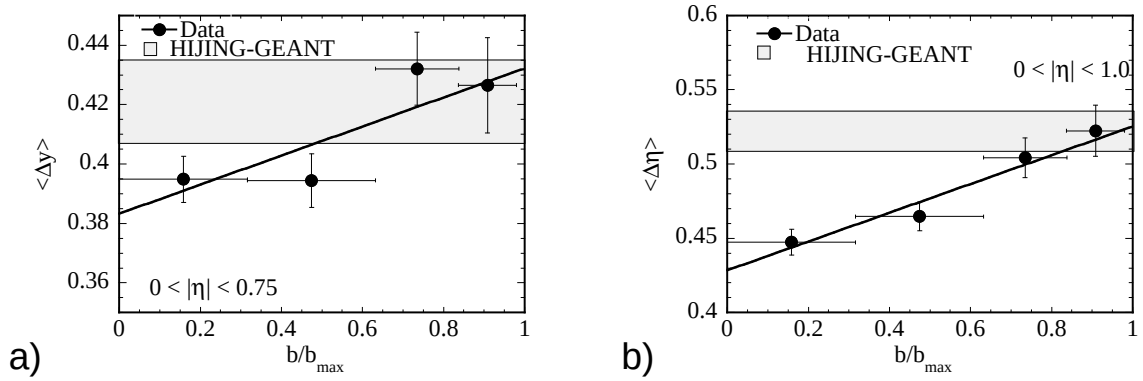

Figure 7.19: Charged particle balance function widths with a linear fit over centrality. Data (circles), and HIJING-GEANT (shaded bar) events are analyzed for particles with a) $|\eta| < 0.75$, and b) $|\eta| < 1.0$.

7.2.1 Pseudorapidity Cuts Quantified

As can be seen in Figures 7.12 to 7.14, the amount of difference in the width of the charged particle balance functions for different centralities changes smoothly. To quantify this, a linear fit can be made to the centrality-dependent widths for each of the different pseudorapidity windows. Figures 7.18 through 7.20 show these linear fits for charged particle balance functions, each on its own scale to show the details. The shaded band representing the HIJING-GEANT balance function width is shown for reference.

Figures 7.21 through 7.23 show the differing widths for pion balance functions

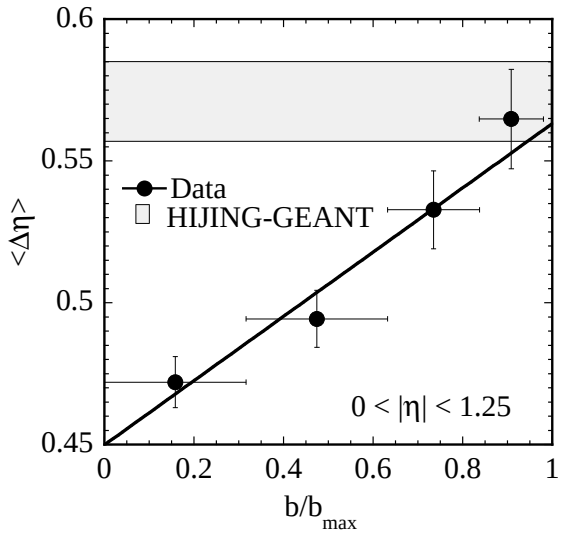

Figure 7.20: Charged particle balance function widths with a linear fit over centrality. Data (circles), and HIJING-GEANT (shaded bar) events are analyzed for particles with $|\eta| < 1.25$.

in pseudorapidity windows from $|\eta| < 0.25$ through $|\eta| < 1.25$. Here the pion pair widths are calculated without the first two bins. The same behavior of how the widths change that was seen in the charged particle pairs is evident again in the pion pair measurements. However, the effect of lower statistics in the pion signal in smaller pseudorapidity windows is more evident. The pion pair measurements reinforce the concept that a rapidity window of two units or larger is necessary to observe a clear centrality dependent effect.

The summary of the changing slopes from the linear fits for both charged particle (closed circles) and pion (open circles) balance function widths can be seen in Figure 7.24. Both slopes change smoothly over the different rapidity windows. The error bars are estimated from the standard error. In the STAR TPC, particles detected within $|\eta| < 0.5$ are known to have a 90% detection efficiency [37]. The efficiency at $|\eta| < 1.0$ is estimated to be about 85%, with the efficiency dropping off faster than linearly towards higher pseudorapidities. The smooth variation of the widths over the region detected indicates a smooth effect of the changing acceptance on the balance function. Most of the effect appears to be the reduction in available $\Delta\eta$ (i.e. one cannot get

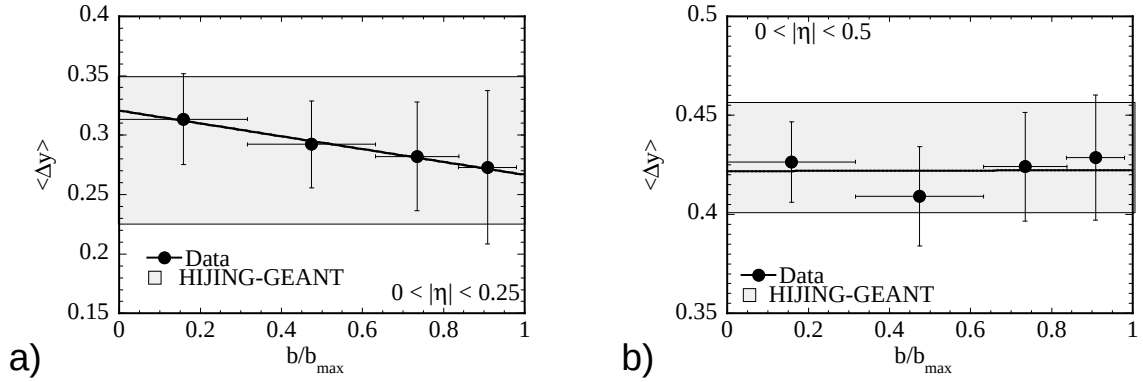

Figure 7.21: Pion pair balance function widths with a linear fit over centrality. Data (circles), and HIJING-GEANT (shaded bar) events are analyzed for particles with a) $|\eta| < 0.25$, and b) $|\eta| < 0.5$.

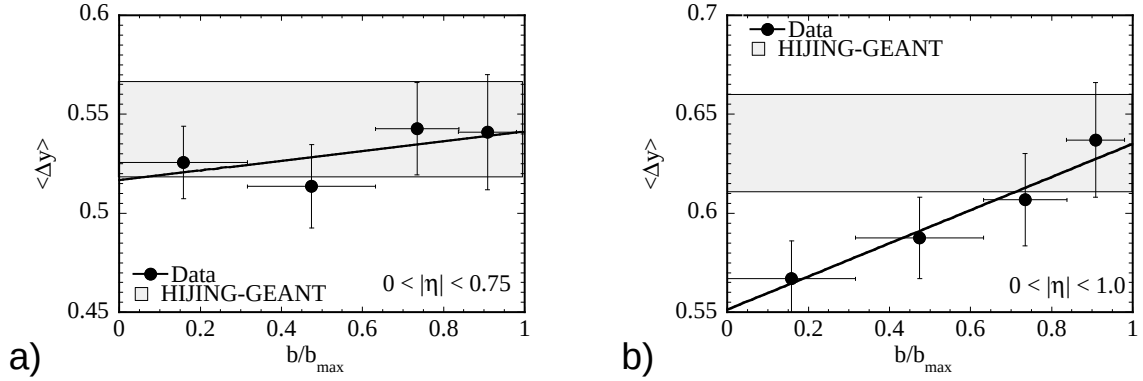

Figure 7.22: Pion pair balance function widths with a linear fit over centrality. Data (circles), and HIJING-GEANT (shaded bar) events are analyzed for particles with a) $|\eta| < 0.75$, and b) $|\eta| < 1.0$.

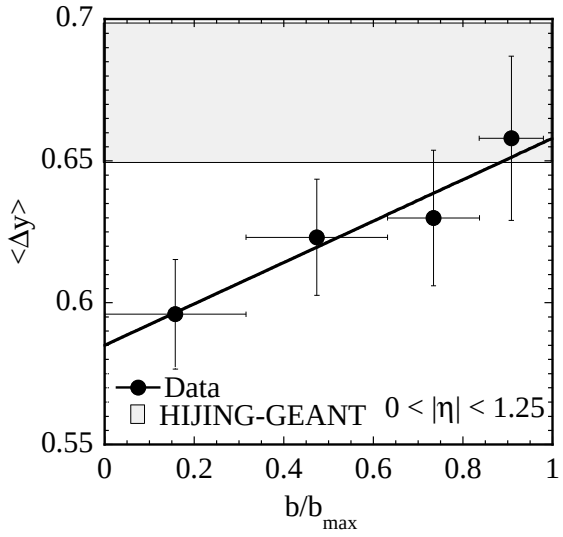

Figure 7.23: Pion pair function widths with a linear fit over centrality. Data (circles), and HIJING-GEANT (shaded bar) events are analyzed for particles with $|\eta| < 1.25$.

$\Delta\eta > 1$ for $|\eta| < 0.5$, and so forth). If the difference in balance function width with centrality is due to the QGP signature occurring over a specific rapidity window, one might expect the balance function widths to plateau at a given pseudorapidity. Considering that the efficiency of STAR deteriorates rapidly above $|\eta| = 1.5$, it may not be possible to see this effect with the STAR TPC alone. Also, the large collision diamond with its large variation of vertices in the year 2000 data affects the detection efficiency strongly. With later data of higher statistics and a more focused collision region, the acceptance dependence of the balance function may be more understood. The addition of the Forward TPCs (FTPCs) will dramatically aid this analysis.

7.3 New Normalization

Another method to remove the acceptance of the detector in a balance function measurement is the new normalization. This method, proposed by Jeon & Pratt [63], involves a balance function which has the denominator of the N_{+-}-type terms modified by the acceptance of the detector. The balance function equation, Equation

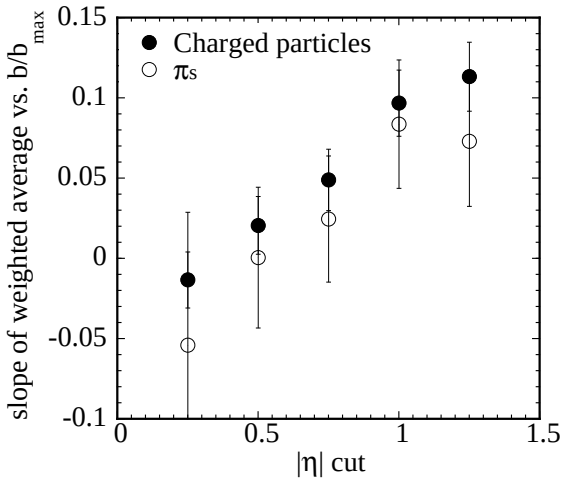

Figure 7.24: Slopes from the linear fits of balance function widths for the various pseudorapidity cuts on the data. Charged particle pairs are closed circles, and pion pairs are open circles.

3.2, is modified to be of the form:

$$B(\Delta y) = \frac{1}{2 * binsize}\left\{\frac{N_{+-}(\Delta y) - N_{++}(\Delta y)}{N_{+}(\Delta y)} + \frac{N_{-+}(\Delta y) - N_{--}(\Delta y)}{N_{-}(\Delta y)}\right\}. \quad (7.1)$$

Here, instead of the N_+ and N_- terms being the same for all possible Δy bins, they are given a dependence on each Δy. For each particle used in the balance function, and each possible Δy, there is a probability of detecting another particle to make a pair in the detector. That probability is between zero and one. For this analysis, only charged particle pair balance functions are calculated, and $\Delta\eta$ bins used instead of Δy. There are 2 approximations that can be made for the probability of detection, the first is that of a sharp cutoff for the detector, in which all pseudorapidities within the $|\eta|$ region used in analysis are a probability of one, and all of those outside of the η region have a probability of zero, as in a step function. With this sharp cutoff, the particle pairs which have a $\Delta\eta$ bin range which has the edges of the detector fall within that range has a probability of $\frac{1}{binsize}$ ($\eta_{\text{(largest } \eta \text{ of detector)}}$ - $\eta_{\text{(low edge of bin)}}$) for a high $\Delta\eta$. The acceptance correction used can be thought of as a line falling from one to zero depending on the pseudorapidity of the particle under consideration. For

instance, for a positive particle of $\eta = 1.25$, the term $N_+(\Delta\eta)$ for the first $\Delta\eta = 0$ bin with binsize =0.1 would be increased by a value of $\frac{1}{2}$. $N_+(\Delta\eta)$ would be increased by one for all bins up to the $\Delta\eta = 2.45$ bin with the following bin (that centered at $\Delta\eta = 2.55$) having an increase of $\frac{1}{2}$. With this method, an extra term of $\frac{1}{2}$ would be needed in the denominator to approximate the amount of particles which are removed by the momentum cut. The calculation method of the denominator is similar to that described for the second probability, where each particle is used as the center of possible $\Delta\eta$ bins of the same size, going up and down in $\Delta\eta$ to the edges of the detector.

The second probability profile of the detector is more complex, as it uses the pseudorapidity distribution of the data itself to get the probability for a given $\Delta\eta$. The probability of a particle being measured in the detector in a given pseudorapidity was found for the fast TPC η simulator as discussed in Section 6.2. The forty histograms of $dN/d\eta$ for different centralities and vertices were normalized such that there is an 85% efficiency of detecting a charged particle entering the region of $|\eta| < 0.5$. The program works as follows. For each charged particle read for balance function analysis, the probability of finding another particle in all possible $\Delta\eta$ bins is added on to $N_+(\Delta\eta)$ or $N_-(\Delta\eta)$. Starting from the η of the particle, and adding the binsize, the first bin centered at $\Delta\eta = 0.05$ is created. This η bin in question contains one possible η middle-of-the-bin value that is used in the $dN/d\eta$ histogram. The probability of survival corresponding to that particular η value considering vertex and centrality is added onto the $N_+(\Delta\eta)$ or $N_-(\Delta\eta)$ term. The next possible $\Delta\eta$ bin is checked, until the edge of the acceptance is reached. Then the negative η region is covered by starting from the η of the particle and subtracting the binsize, and again comparing to the η middle-of-the-bin values for the $dN/d\eta$ histogram for increasing the denominator term.

Computationally, both methods are fairly simple. Separate files with only the

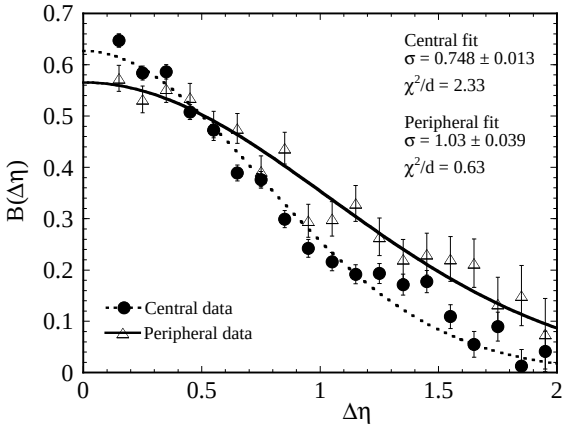

Figure 7.25: Charged particle pair balance function for central (circles) and peripheral (open triangles) events, analyzed with the new, η-dependent normalization. Gaussian fits are applied omitting the first bin.

acceptance-dependent $N_+(\Delta\eta)$ and $N_-(\Delta\eta)$ can be generated. These new denominators can be used with the already calculated numerators, and the new normalization balance function measured. Jeon and Pratt [63] warn that this method may not be feasible to utilize in sufficiently small acceptance bins due to statistics. Instead, the method of applying the acceptance to simulations of theory and doing a comparison minimizes the statistical and systematic error. However, this new normalization method allows for a removal of the acceptance, which reference [63] claims will allow for a clear physical interpretation of the balance function measurement. The amount of error is due to the level of understanding the acceptance is not simple to calculate. For the measurements shown here, the simple statistical error bars are used.

7.3.1 Data

The complete final data set is analyzed using this new normalization method. The balance function for charged particle pairs is shown in Figure 7.25. A Gaussian fit is shown for both sets of centrality. It is clear from the Gaussian fits that the central data has a narrower balance function than the peripheral data. As in the analysis in Section 5.2, the charged particle pairs have identified electrons removed.

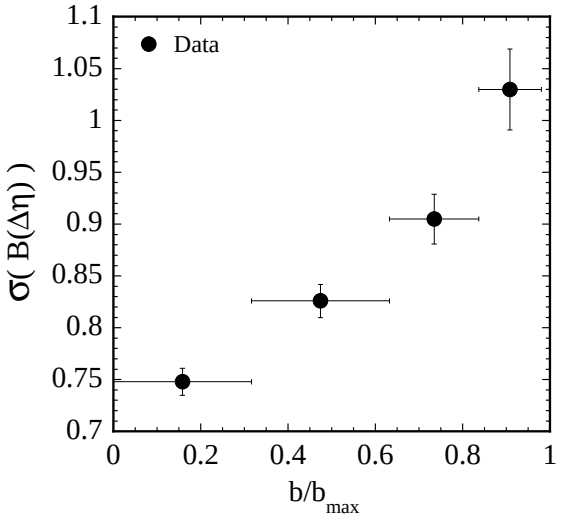

Figure 7.26: Charged particle pair balance function Gaussian fit widths for data (circles), analyzed with the new, η-dependent normalization.

The summary for Gaussian widths of the charged particle pair balance function is shown in Figure 7.26. The behavior of these widths with respect to centrality is the same as the behavior in the original normalization method described in Chapter 5.

Turning to the pion pairs, Figure 7.27 shows the balance function measured with new normalization for pion pairs. The difference between central and peripheral events evident. The HBT effect in the region near Δy=0 can be seen. The widths of the pion pair balance function are shown in Figure 7.28. The Gaussians shown are calculated without the first two bins to reduce the HBT effect. The trend can again be seen of the central events having a narrower width pion pair balance function than the peripheral events.

The pion pair balance function with this new normalization measured with respect to $\Delta\eta$ and its Gaussian fit are shown in Figure 7.29. The central data is narrower than the peripheral data. The weighted average widths are calculated omitting the first two bins to exclude the HBT effect. These widths are shown in Figure 7.30.

The error bars shown for this new normalization method have only been statistical. A systematic error bar which is larger than those shown for the old normalization

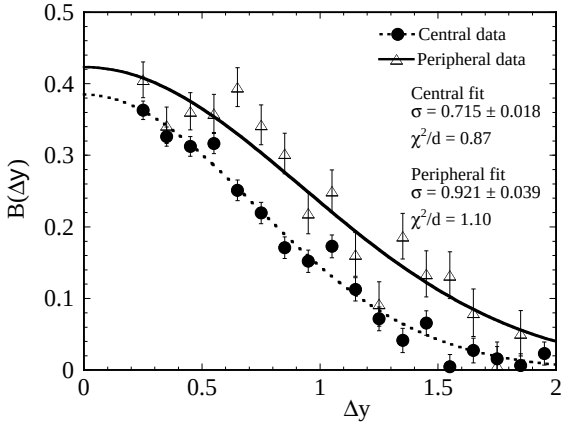

Figure 7.27: Pion pair balance function for central (circles) and peripheral (open triangles) events, analyzed with the new, η-dependent normalization. Gaussian fits are applied omitting the first two bins.

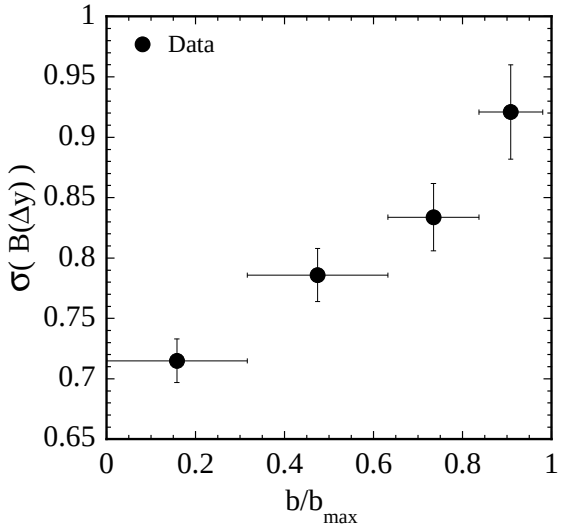

Figure 7.28: Pion particle pair balance function Gaussian fit widths for data (circles), analyzed with the new, η-dependent normalization. Gaussian fits omit the first two bins.

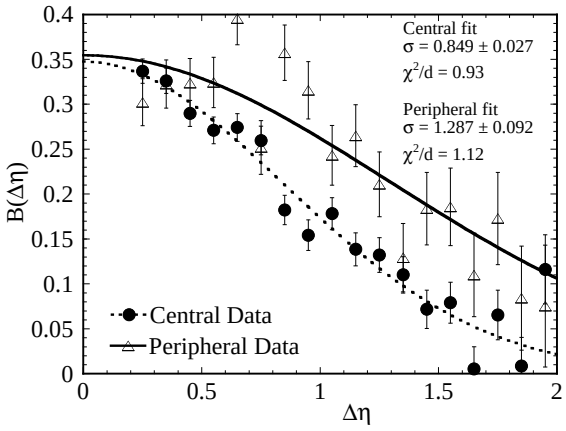

Figure 7.29: Pion pair balance function ($\Delta\eta$) for central (circles) and peripheral (open triangles) events, analyzed with the new, η-dependent normalization. Gaussian fits are applied omitting the first two bins.

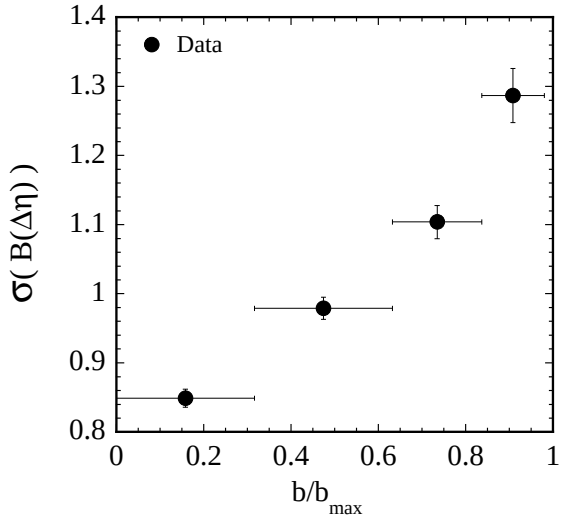

Figure 7.30: Pion particle pair balance function ($\Delta\eta$) Gaussian fit widths for data (circles), analyzed with the new, η-dependent normalization. Gaussian fits omit the first two bins.

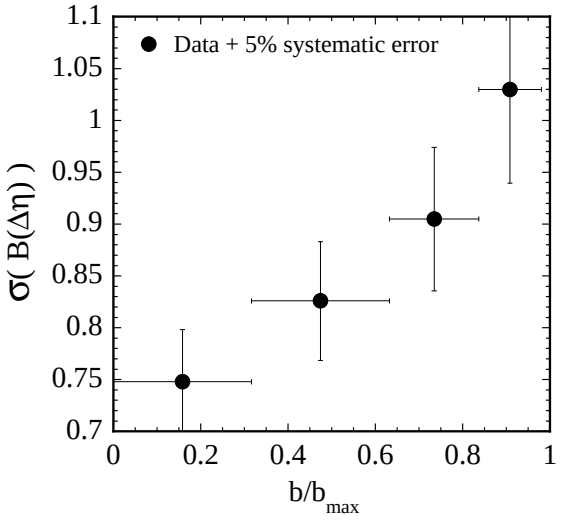

Figure 7.31: Charged particle pair balance function Gaussian fit widths for data (circles), analyzed with the new, η-dependent normalization. Width error bars have an additional 5% systematic error.

is expected. The size of that error bar depends on how well the probability of a particle's survival is known. The change in the charged particle error bar adding a systematic 5% to the Δy was about 1.1% of the original width value shown in Figure 5.17. A rough estimate would place the new normalization change in the error bar sizes to be about 5% of the original width value. The charged particle widths still shows different widths between central and peripheral. However, there is considerable overlap between neighbor centralities, as seen in Figure 7.31.

7.3.2 Simulations

It is also possible to study the effect of the new normalization on simulated events. Shown in Figure 7.32 a) is the charged particle pair balance function for HIJING-GEANT events analyzed with the new normalization version of the balance function. Figure 7.32 b) shows in comparison the charged particle pair balance function for simulated HIJING p+p events which are analyzed in a perfect detector. As the detector is perfect, the old and new normalization give the same result, since the probability of detecting particles is one everywhere. The simulated HIJING-GEANT events have

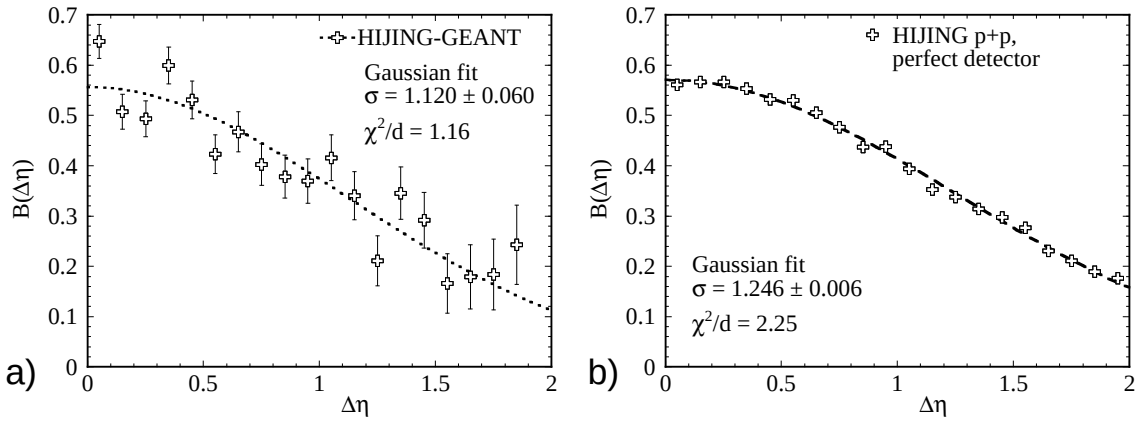

Figure 7.32: a) Charged particle pair balance function for HIJING-GEANT simulated events, analyzed with the new, η-dependent normalization. b) Charged particle pair balance function for HIJING p+p events in a perfect detector, analyzed with the old normalization.

a new normalized balance function which looks more like the theoretical prediction in Figure 7.32 b). It appears that more statistics for the HIJING-GEANT events is needed for a more accurate comparison.

The widths of the two HIJING sets with and without a detector can be compared to the data charged particle Gaussian fit width. This comparison is shown in Figure 7.33. The peripheral data has a width which is close to that of HIJING, whereas the central data has a width much narrower. More statistics and a more accurate estimate of the detector's acceptance could improve these measurements greatly. It does appear that the new normalization can reduce the dependence on the acceptance of the detector. This can also be illustrated with the mixed events, as discussed next.

7.3.3 Mixed Pseudorapidity

The charged particle pair balance function calculated with this new normalization method is shown in Figure 7.34. The central shuffled η data analyzed with the new normalization is represented by squares with x's, and the non-mixed data by closed circles. Here it can be seen that the mixed events with the acceptance correction applied has a flat balance function. This appears to reinforce the concept that the

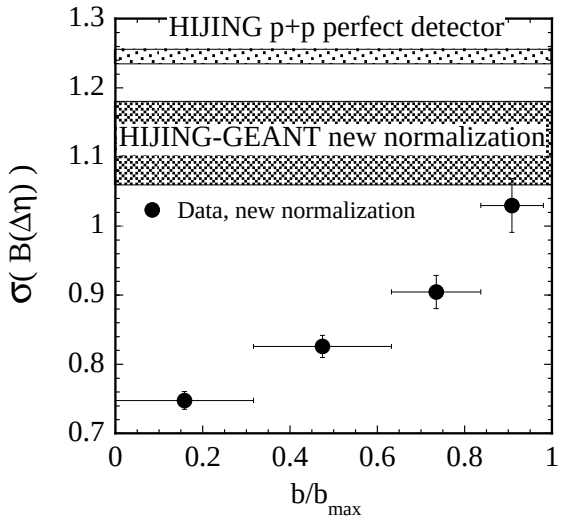

Figure 7.33: Charged particle particle pair balance function Gaussian fit widths for data (circles), analyzed with the new, η-dependent normalization. The top shaded bar shows old normalization HIJING p+p events Gaussian width. The lower shaded bar shows the Gaussian width for HIJING-GEANT events analyzed with the new normalization.

mixed pseudorapidity events are a reasonable measure of the background to the balance function. Also, this indicates that the new normalization reduces effects of the detector acceptance on the balance function measurement.

7.4 Vertex Asymmetry

For a number of different STAR data analyses in the year 2000, an asymmetry between events with positive and negative vertices in the z-direction was observed. Most of these analyses were able to include this effect into the systematic error bar of the measurement. One possible reason for this asymmetry was the effect due to tracks crossing the central membrane. That can be removed by analyzing tracks in one half of the TPC or analyzing tracks with a narrow region around midrapidity missing. Both halves of the TPC are needed for balance function analysis and, as previously stated, large statistics are required to observe a reasonable signal. Thus, the method used to test the vertex asymmetry was to calculate the balance function for those events which

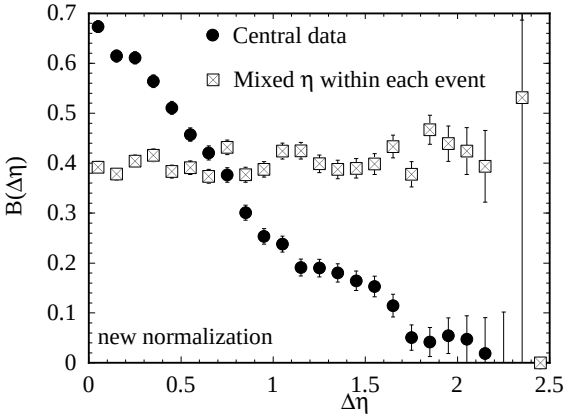

Figure 7.34: Charged particle pair balance function, analyzed with the new η-dependent normalization. Central data is represented by closed circles, and mixed η central data is represented by squares with x's.

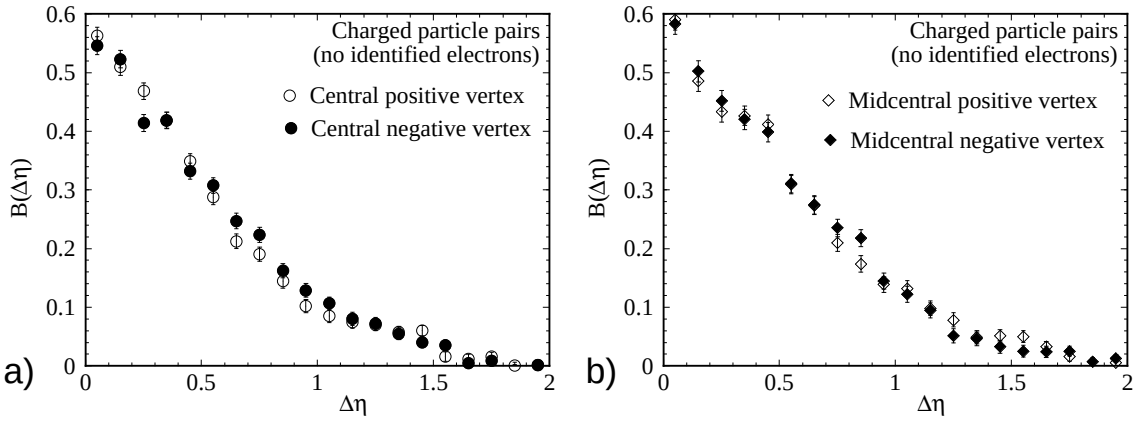

Figure 7.35: Charged particle balance function for a) central positive (open circles) and negative (closed circles), and b) midcentral positive (open diamonds) and negative (closed diamonds) vertex events.

have a vertex on the negative half of the TPC and compare the balance function to events which have a positive vertex. Figures 7.35 and 7.36 show the difference between balance functions measured with positive and negative vertex events.

The effect of the vertex asymmetry appears to be the strongest in the peripheral events, with weakening effect as centrality increases. An alternative is that this could be due to the lower statistics of the peripheral data set. The summary of charged particle balance function widths for the positive and negative vertex events is shown in Figure 7.37. These widths are calculated omitting the first bin of the charged

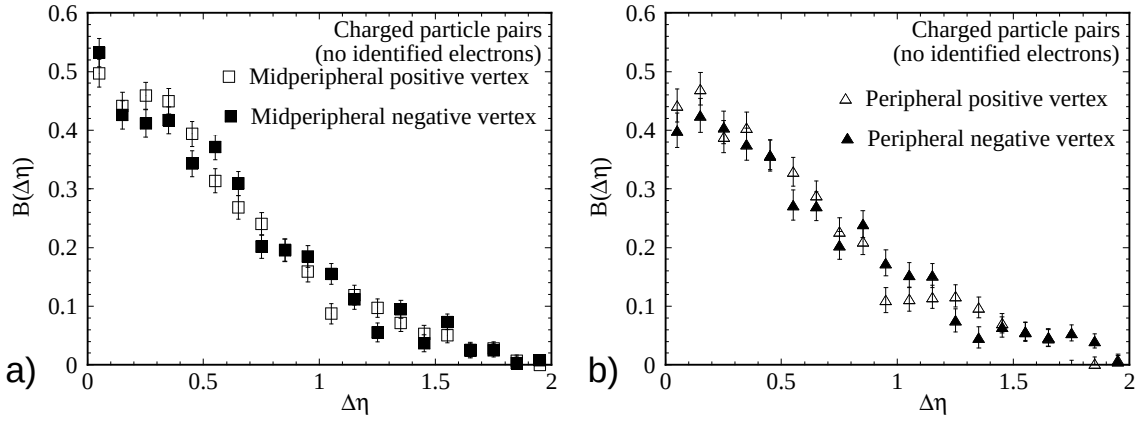

Figure 7.36: Charged particle balance function for a) midperipheral positive (open squares) and negative (closed squares), and b) peripheral positive (open triangles) and negative (closed triangles) vertex events.

particle balance function.

In contrast, the pion balance function is measured as a function of rapidity. The possible momentum dependence of the vertex measurement is included in this subset of the balance function comparison. The comparison of positive and negative vertex pion balance function widths is shown in Figure 7.38. These widths are calculated omitting the first two bins, as in Chapter 5.3.

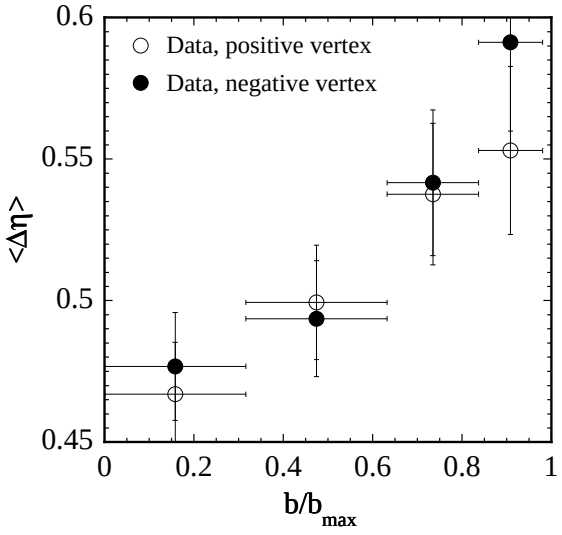

Figure 7.37: Summary of charged particle balance function widths for data with positive (open circles), and negative (closed circles) vertices in the z direction.

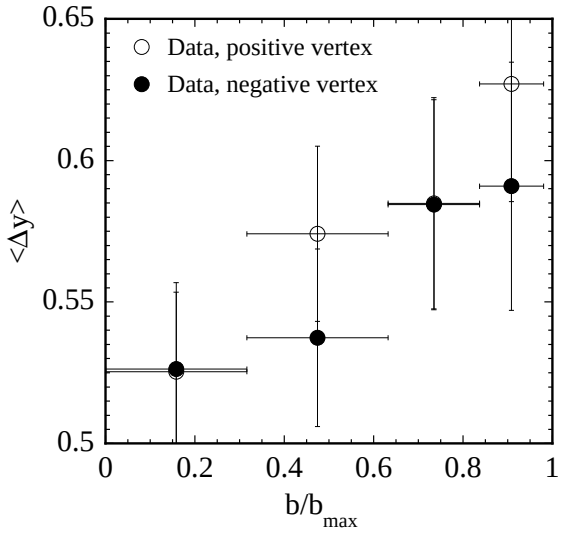

Figure 7.38: Summary of pion balance function widths for data with positive (open circles), and negative (closed circles) vertices in the z direction.

For the HIJING-GEANT simulated events, the same procedure can be done. These are the HIJING simulated events, processed through a STAR simulator and analyzed in the same fashion as the data, discussed in Chapter 6. Figure 7.39 shows the charged particle and pion pair balance functions for these simulated events. The effect of the different vertex events appears to be in the simulated events as well. This could be due to an asymmetry in GEANT, or TRS, the TPC reconstruction code. This could also merely be the effect of cutting the statistics in half.

7.4.1 Two Randomly Assigned Sub-Events

To find the cause of the differences in positive and negative vertex events, an exercise can be done in which the data set is randomly split in half. In this case the data was analyzed with each event placed with equal random possibility in either the 1st or 2nd new data set. Each of these data sets was used to measure the balance function, and the results can be compared to those of the positive and negative vertex events.

For charged particle pairs, the difference in the two random halves can be seen for the four centrality bins in Figures 7.40 and 7.41. It appears that the difference in the

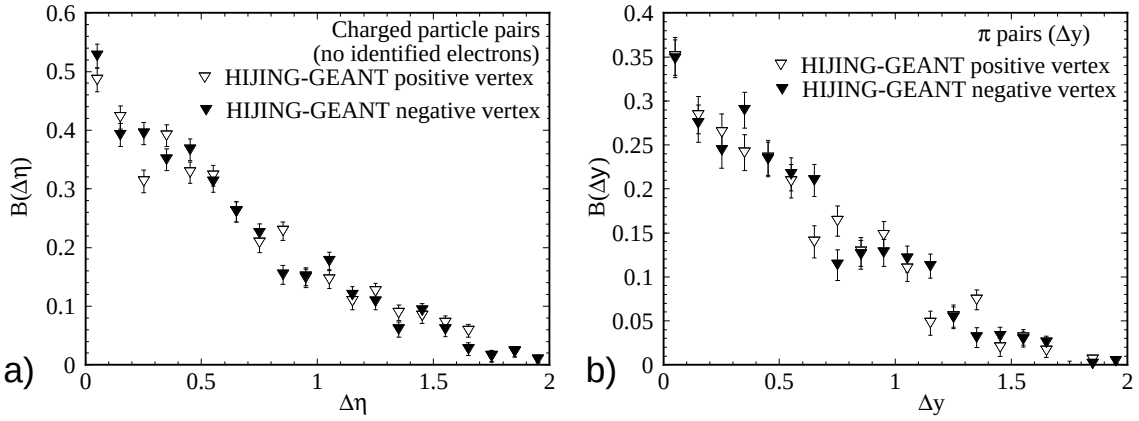

Figure 7.39: a) Charged particle balance function for simulated HIJING-GEANT positive (open inverted triangles) and negative (closed inverted triangles) vertex events. b) Pion pair balance function for HIJING-GEANT positive (open inverted triangles) and negative (closed inverted triangles) vertex events.

data sets is due to statistics, with the peripheral data set having the largest overall difference between the two random sub-event sets.

The widths of the charged particle balance function for the two sub-event sets are shown in Figure 7.42. These widths are calculated without the first bin. The difference between widths appears similar to that between the two positive and negative vertex event sets. The pion pair balance function widths are shown in Figure 7.43. Again, the difference observed in the two random sub-events affirms that the supposed vertex

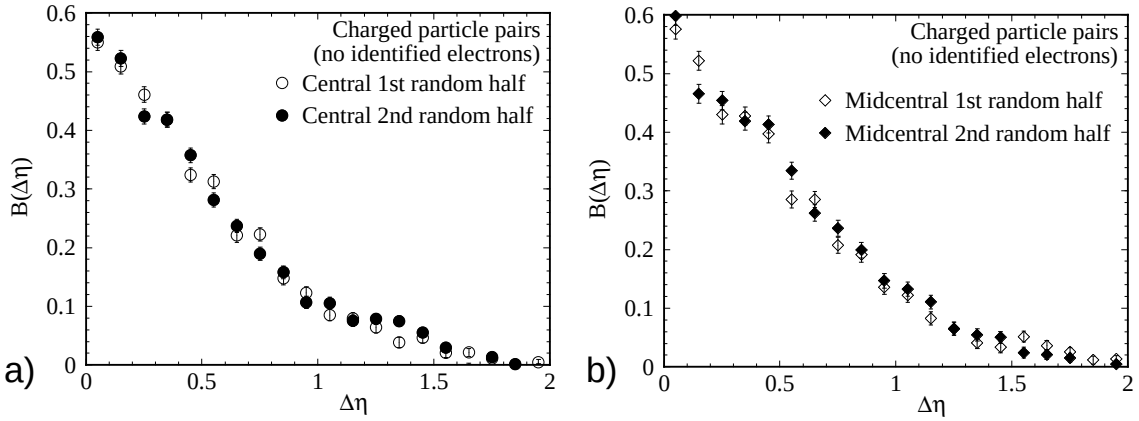

Figure 7.40: Charged particle balance function for a) central 1st (open circles) and 2nd (closed circles), and b) midcentral 1st (open diamonds) and 2nd (closed diamonds) half of the data set.

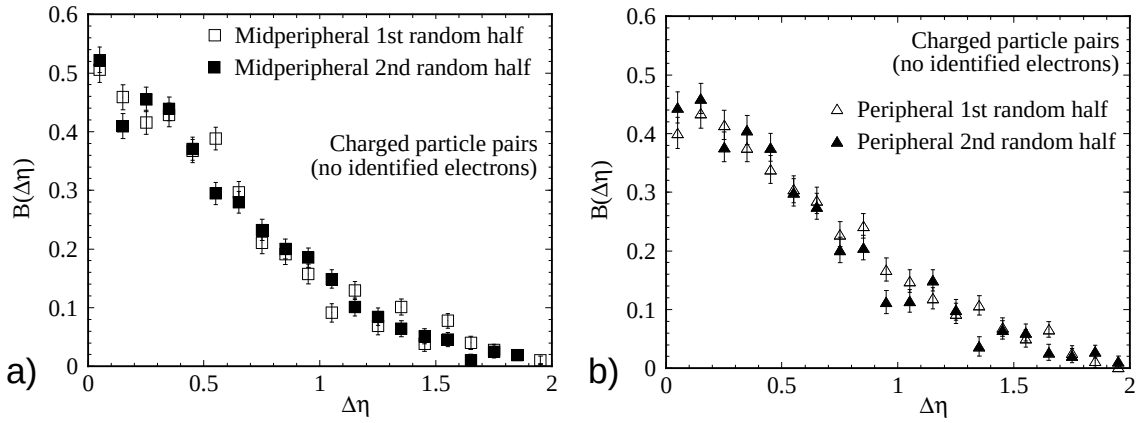

Figure 7.41: Charged particle balance function for a) midperipheral 1st (open squares) and 2nd (closed squares), and b) peripheral 1st (open triangles) and 2nd (closed triangles) half of the data set.

asymmetry is not observable with the statistics of the year 2000 event set. The effect seen can be attributed to statistics and not merely a vertex asymmetry.

7.5 Acceptance Summary

The balance function as measured is affected both by the geometry of the detector and the statistics of the data set used. However, in studying these dependencies, the

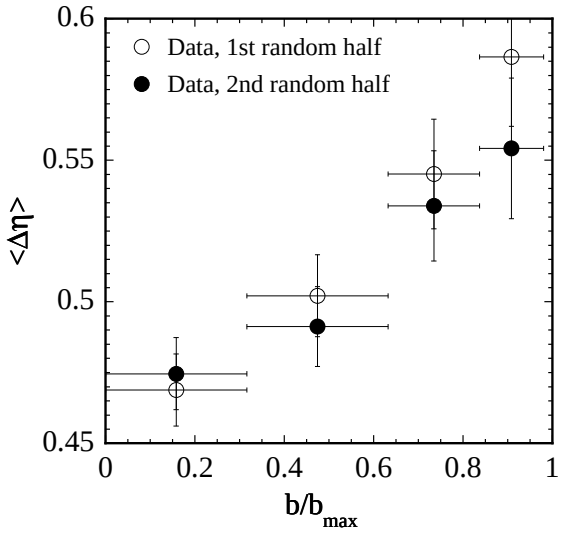

Figure 7.42: Summary of charged particle balance function widths for data with the 1st (open circles), and 2nd (closed circles) half of the data set.

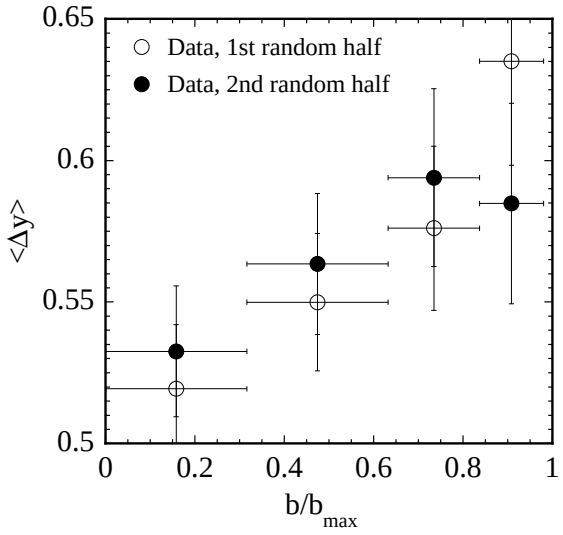

Figure 7.43: Summary of pion pair balance function widths for data with the 1st (open circles), and 2nd (closed circles) half of the data set.

measurement can be further understood. Mixing events in the traditional fashion, as well as randomizing charge gives a balance function of zero. Events which have the pseudorapidity of the detected particle mixed within the event have a measurable balance function. The charged particle and pion pair balance functions for both data and simulations have widths narrower than events with shuffled η, showing a physical signal above this acceptance background. The estimations of the systematic error bar by a 5% contribution in $\Delta\eta$ or Δy in Section 5.6 appear to be low when compared to the measurements of two different sets of sub-events in Section 7.4. A systematic error bar combining the 5% error in $\Delta\eta$ or Δy with the 10% error in the N_{+-}-type terms would agree with these results.

Chapter 8

Future of the Balance Function

The balance function is a rich observable that provides many possibilities for measurements to probe the dynamics of a relativistic heavy ion collision. This dissertation has only scratched the surface of what types of analyses are possible using the balance function as a tool.

8.1 Modifications of Pion and Charged Particle Measurements

Currently, the balance function, as given by Equation 3.2, does not remove the effects of the detector acceptance from the measurement. Several methods to eliminate these effects were employed. The new normalization, discussed in reference [63] and shown in Section 7.3, appears to remove the detector acceptance. However, that method includes a modification to the denominator which is detector-dependent, including all its systematic errors. Alternatively, simulations were processed through GEANT and TRS, and compared with the data. This method, while functional, is cumbersome. A third possibility is the fast η-dependent TPC simulator. Although it is fast, it also depends on the amount and quality of data. Also, the fast simulator does not include

all physical aspects of the detector's efficiency, only that of pseudorapidity.

An alternate method for comparison of data with theory might be based upon the idea of extracting the image of the original source from a measured "fuzzy" image [73]. Perhaps the shape of the measured balance function for both charged particles($\Delta\eta$) and pion pairs($\Delta\eta$ & Δy) could be expressed mathematically as it changes from perfect to real detector. Such a relation would simply allow translation from the measured balance function to obtain a shape which can be compared with theoretical predictions using a perfect detector.

With the year 2000 data, there were only sufficient statistics to perform balance function measurements on charged particle pairs and pion pairs in the momentum and pseudorapidity region used in Chapter 5. Future data sets will be obtained with RHIC in full operational capacity, with higher beam luminosity, and thus, more data. Some of these measurements were already measured in 2001 at $\sqrt{s_{NN}} = 200\ GeV$. With higher statistics, the statistical error bars will reduce, and the efficiency of the detector can be better understood, which may reduce the systematic error bars as well.

Once a higher statistics data set is obtained, cuts can be made upon the balance function measurement to study different effects. Centrality could be divided into more than four bins and the kaon balance function could be measured. There may be sufficient statistics to measure the proton balance function, although this requires care to remove the background from the proton signal. Another possibility would be to perform transverse momentum cuts on the balance function analysis. With the addition of the FTPCs in STAR, the possible pseudorapidity measurement region is greatly increased, providing for measurements of the balance function over a larger η than shown here. If the QGP has a characteristic size in η, a stabilization of the balance function width at larger $\Delta\eta$ may show that.

Many simulations are possible to understand the measurements. An ideal simula-

tor would use all the physics features within a quark-gluon plasma creating collision, and produce predictions which can be compared with measurements. Perhaps experimenting with different modifications to the existing simulators may also shed light on the cause of the balance function narrowing. It has been suggested that the effect of resonance decays on the balance function should be studied. The cuts used in this analysis remove most of the particles from secondary decays. However, a worst-case model could be constructed of only resonance particles decaying, with a given amount superimposed with conservation of charge upon both the Bjorken and HIJING simulations. To have the current balance function measurement be an indication of only a large difference in the amount of resonance particles created would indicate a pathological case. Alternately, indication of a big change in resonance particles would show that something interesting and not understood by current models is occurring. Flow, as well as HBT could be included in both the HIJING and Bjorken models to study their effects, and compare after detector simulation with the data's balance function. Also, the Bjorken model can be improved to incorporate more aspects of physics, and multiple particle creation. Note that RQMD does include both resonances and flow and measures the incorrect centrality dependence for the balance function.

Care must be taken with each data set to ensure that events which are combined have the same detector acceptance. The effect of having a portion of the TPC inactive was not studied here. Although the balance function does not show dependency upon multiplicity, a complete study of the detector response as a function of multiplicity will improve the understanding of the effects of the detector. Of most importance, the measurements here should be considered together with the other measurements made by STAR, PHOBOS, PHENIX, and BRAHMS. By considering what effect these measurements have on theory, together with the effect of the balance function measurements, a coherent picture of the dynamics of the relativistic heavy ion collision could be formed. The fascinating results of the HBT physics group in STAR appear to

indicate that emission is fast and happens over a small period of time [31], [74]. Taken together with the late hadronization that the balance function indicates, there could be a QGP formed, existing for some time, then it hadronizes at a late time, finishing the hadronic interactions quickly before the particles emerge into the detector.

8.2 Event-By-Event Balance Function

It has been suggested that the balance function measured for each *single* event could be used instead of centrality as an indication of interesting events [75]. Perhaps the weighted average width could be quickly calculated and events with widths below a given value could be tagged as interesting with both the balance function and other observables measured for those events in comparison with peripheral data.

A preliminary look at the effectiveness of this type of measurement is shown with the charged particle balance function widths and statistical error on the widths for single events, given in Table 8.1. The overall balance function for a single event is given in Figure 8.1. It can be seen both from the scale and error bars in the overall balance function as well as the statistical error of the widths that this type of measurement needs work. The balance function calculated for each event can be useful once the errors are better understood, and a threshold width for interesting events set once a large data set is studied.

8.3 Other Collision Measurements

Of prime importance is the analysis of the balance function for p+p collisions. As the balance function is new to heavy ion physics, there is no existing CERN SPS data with which to compare the current measurement. A comparison is needed of events measured with the STAR detector which have known physical behavior, and known not to form the quark-gluon plasma. In 2001, STAR did record p+p collisions at

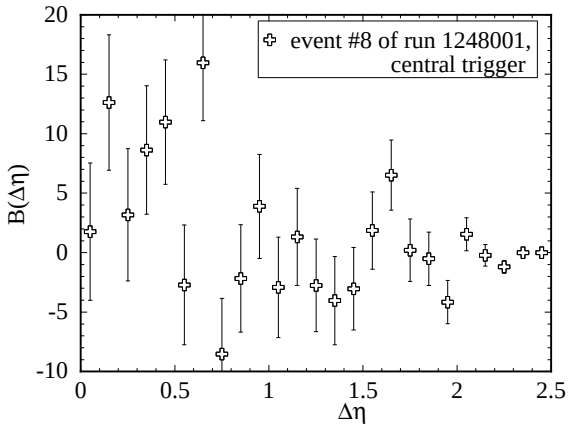

Figure 8.1: Charged particle balance function for one event from a central trigger data set. Charged particles do not include identified electrons. Note the scale.

trigger	run	event number	number centrality tracks	number balance function tracks	charged particle $< \Delta\eta >$	error
minbias	1237025	2520	389	376	0.4126	0.1335
minbias	1237025	2521	235	236	0.3667	0.1259
minbias	1237025	2522	146	135	0.5624	0.0618
minbias	1237025	2523	330	320	0.4816	0.0870
minbias	1237025	2524	176	147	0.6352	0.0381
minbias	1237025	2525	76	83	0.5692	0.0977
minbias	1237025	2526	24	23	0.6134	0.0764
minbias	1237025	2527	271	263	0.4796	0.0876
minbias	1237025	2528	67	71	0.5807	0.0914
minbias	1237025	2529	13	19	0.6032	0.1058
minbias	1237025	2530	333	312	0.5197	0.0938
central	1238009	1	433	403	0.4504	0.9033
central	1238009	2	394	392	-0.0326	-1.3035
central	1238009	3	406	414	0.4308	0.9921
central	1238009	4	454	419	0.6455	0.4761
central	1238009	5	440	446	0.8200	1.0250
central	1238009	6	341	327	0.7710	0.5036
central	1238009	7	350	382	0.8780	2.4572
central	1238009	8	413	375	0.5548	0.4646
central	1238009	9	428	390	0.4700	0.4246

Table 8.1: Charged particle balance function weighted average widths, and statistical error bars for single events from both minimum bias (top) and central (bottom) triggers.

$\sqrt{s_{NN}} = 200\ GeV$. These events should have the balance function measured. This would be a more conclusive check to ensure that the peripheral data from the Au+Au collisions does have a balance function consistent with p+p collisions, meaning that it is, in fact, behaving like a superposition of nucleon-nucleon scattering. It is expected that the p+p collisions would have no variation over centrality for the balance function as measured both with charged particles and pion pairs.

Collisions at higher energies might have a QGP that lives for a longer time, or other interesting features which the balance function could provide. A study of temperature or time (recalling the parameters used in the Bjorken thermal model, Section 6.3.1) could be done, observing variations with respect to beam energy. The balance function has a rich and interesting future in relativistic heavy ion physics.

Chapter 9

Conclusions

In this thesis, balance functions have been measured for collisions of Au+Au ions at a center of mass energy of 130 GeV. The balance function measured for both pion pairs and charged particle pairs in peripheral collisions has a width which is similar to that predicted by HIJING, which incorporates a superposition of nucleon-nucleon scattering to describe Au+Au collisions. As collisions become more central, the measured balance function width becomes more narrow. Central collisions produce a width of the pion pair balance function which is similar to a model including Bjorken expansion, strong radial flow, and emission of balancing particle pairs close at the same point in space-time. It appears that this narrow balance function width for central events indicates hadronization at a late time, which can mean that the quark-gluon plasma was formed in the central collisions.

Simulations of varying model interactions show the behavior of the balance function for different types of collisions, whether they are only hadronic gas (HIJING - nucleon-nucleon scattering), or the quark-gluon plasma (Bjorken). HIJING events at different impact parameters from 0 to 15 fm all show the same balance function shape and width as is expected for nucleon-nucleon scattering events. Bjorken simulations also show that the shape and width of the balance function does not change with respect to multiplicity. A fast simulator of the STAR TPC was created which uses

the measured efficiency of the detector to predict a particle's survival as a function of its η. This fast simulator gives balance function measurements for HIJING which are consistent with a balance function measured with HIJING analyzed through GEANT and the full detector reconstruction.

The acceptance dependence of the balance function measured in STAR has also been studied. Creating mixed events by shuffling the pseudorapidities of detected charged particles is the mixed event technique which gives a non-zero balance function. The balance functions for the data at all centralities, as well as for HIJING events processed through a STAR detector simulation, have a clear shape above these mixed η events, as well as widths which are all narrower than the mixed η balance function width. In addition, the balance function must be measured over a large enough η range to observe the width differences that are dependent upon particle hadronization and movement over time and space. It appears that a pseudorapidity window of 2 units or more is necessary to measure late hadronization with the balance function. The acceptance-dependent new normalization of the balance function removes the detector acceptance of the shuffled η events, giving an almost flat balance function. The new normalization balance functions measured also show the same centrality dependent width behavior as the regularly normalized data.

The balance function is an interesting and useful measurement for relativistic heavy ion physics. In this dissertation, it has been shown that the measurements here may indicate the formation of a quark-gluon plasma at the most central RHIC collisions of Au+Au at $\sqrt{s_{NN}} = 130\ GeV$.

APPENDIX

Appendix A

Tables: STAR 2000 Data Quality

date	run number	number events in DAQ file	number which passed event cuts	kind of trigger used	analysis library
7/25/00	1207002	5427	2045	minbias	P00hi
7/25/00	1207004	2654	798	minbias	P00hi
7/25/00	1207006	7954	41	minbias	P00hi
7/25/00	1207009	1016	151	minbias	P00hi
7/25/00	1207010	1049	148	minbias	P00hi
7/25/00	1207013	1966	294	minbias	P00hi
7/25/00	1207014	220	45	minbias	P00hi
7/25/00	1207015	2556	433	minbias	P00hi
7/26/00	1208001	4071	1625	minbias	P00hi
7/26/00	1208002	1095	401	minbias	P00hi
7/26/00	1208003	6195	2035	minbias	P00hi
7/30/00	1212010	40	2	minbias	P00hi
8/6/00	1219003	24	6	minbias	P00hm
8/6/00	1219006	261	84	minbias	P00hm
8/6/00	1219022	3241	937	minbias	P00hm
8/8/00	1221015	1377	460	minbias	P00hm
8/9/00	1222004	342	113	minbias	P00hm
8/9/00	1222005	4732	1603	minbias	P00hm
8/9/00	1222006	878	300	minbias	P00hm

Table A.1: STAR data runs from 2000 used in this analysis, continues on next two pages.

date	run number	number events in DAQ file	number which passed event cuts	kind of trigger used	analysis library
8/9/00	1222007	3635	1205	minbias	P00hm
8/10/00	1223002	57771	3186	minbias	P00hm
8/16/00	1229018	9169	2792	central	P00hi
8/16/00	1229024	3667	852	minbias	P00hi
8/16/00	1229026	4148	3076	minbias	P00hm
8/16/00	1229027	24359	6897	minbias	P00hm
8/16/00	1229031	1089	198	minbias	P00hm
8/16/00	1229032	4148	800	minbias	P00hm
8/17/00	1230015	3876	1001	minbias	P00hm
8/18/00	1231003	3216	935	minbias	P00hm
8/18/00	1231005	2195	643	minbias	P00hm
8/18/00	1231011	6537	1850	minbias	P00hm
8/18/00	1231012	15542	4200	minbias	P00hm
8/18/00	1231015	28866	7598	minbias	P00hm
8/24/00	1237025	10013	2530	minbias	P00hm
8/25/00	1238009	10011	72	central	P00hm
8/25/00	1238019	6938	1556	minbias	P00hm
8/25/00	1238020	29951	6727	minbias	P00hm
8/25/00	1238029	10014	1196	central	P00hm
8/25/00	1238037	2922	1362	central	P00hm
8/25/00	1238038	12300	4157	central	P00hm
8/26/00	1239010	24550	6043	minbias	P00hm
8/26/00	1239012	29509	6454	minbias	P00hm
8/26/00	1239013	11578	2247	minbias	P00hm
8/27/00	1240006	9599	4855	central	P00hm
8/27/00	1240015	4651	2379	central	P00hm
8/27/00	1240026	14912	1198	central	P00hm
8/28/00	1241008	21675	6252	minbias	P00hm
8/28/00	1241010	12157	3357	minbias	P00hm
8/28/00	1241013	5858	1660	minbias	P00hm
8/28/00	1241018	5594	2785	central	P00hm
8/28/00	1241026	7437	2978	central	P00hm
8/30/00	1243006	10014	5258	central	P00hi
8/30/00	1243010	1002	391	central	P00hi
8/30/00	1243012	5315	1418	central	P00hi
8/30/00	1243017	23017	5878	minbias	P00hm

Table A.1: continued. STAR data runs from 2000 used in this analysis, continued from previous page.

date	run number	number events in DAQ file	number which passed event cuts	kind of trigger used	analysis library
8/30/00	1243020	1724	411	minbias	P00hm
8/30/00	1243037	6856	958	central	P00hi
8/30/00	1243038	1037	116	central	P00hi
8/30/00	1243042	5852	995	central	P00hi
8/30/00	1243047	16734	6625	central	P00hm
8/31/00	1244007	10013	4459	central	P00hm
8/31/00	1244011	4964	1275	minbias	P00hm
8/31/00	1244013	4028	961	minbias	P00hm
8/31/00	1244014	18831	4680	minbias	P00hm
8/31/00	1244023	10012	5093	central	P00hm
8/31/00	1244041	7584	3663	central	P00hm
9/1/00	1245004	10014	1667	central	P00hi
9/1/00	1245006	5442	2608	central	P00hm
9/1/00	1245008	10012	1289	central	P00hi
9/1/00	1245009	5032	573	central	P00hi
9/1/00	1245014	14119	5461	central	P00hi
9/1/00	1245015	8710	1933	minbias	P00hm
9/2/00	1246009	1973	940	central	P00hm
9/2/00	1246011	703	334	central	P00hi
9/2/00	1246013	2744	1278	central	P00hi
9/2/00	1246015	10014	1654	central	P00hi
9/2/00	1246018	22482	4865	minbias	P00hm
9/3/00	1247007	1788	1667	central	P00hi
9/3/00	1247014	5142	4704	central	P00hm
9/3/00	1247015	26438	7080	minbias	P00hm
9/3/00	1247017	7462	1954	minbias	P00hm
9/3/00	1247018	11344	2889	minbias	P00hi
9/3/00	1247027	6571	6137	central	P00hm
9/3/00	1247030	5874	5481	central	P00hm
9/3/00	1247033	4398	4069	central	P00hm
9/3/00	1247044	1031	949	central	P00hi
9/3/00	1247045	668	307	central	P00hi
9/3/00	1247047	16060	480	central	P00hi
9/4/00	1248001	6209	3036	central	P00hm
9/4/00	1248006	15305	4115	minbias	P00hm
9/4/00	1248009	3545	3301	central	P00hi
9/4/00	1248015	77841	22376	minbias	P00hm
9/4/00	1248017	44138	11551	minbias	P00hm
9/4/00	1248022	3737	3488	central	P00hm

Table A.1: continued. STAR data runs from 2000 used in this analysis, continued from previous two pages.

date	run number	number events	kind of trigger	reason not to use
7/3/00	1185005	1235	minbias	Q. Liu says ZDC vs. mult looks bad
7/3/00	1185007	1045	minbias	Q. Liu says ZDC vs. mult looks bad
7/3/00	1185008	591	minbias	Q. Liu says ZDC vs. mult looks bad
7/3/00	1185012	1728	minbias	Q. Liu says ZDC vs. mult looks bad
7/4/00	1185015	4276	minbias	Q. Liu says ZDC vs. mult looks bad
7/4/00	1185017	7246	minbias	Q. Liu says ZDC vs. mult looks bad
7/4/00	1186006	479	minbias	Q. Liu says ZDC vs. mult looks bad
7/4/00	1186007	85	minbias	Q. Liu says ZDC vs. mult looks bad
7/4/00	1186014	318	minbias	Q. Liu says ZDC vs. mult looks bad
7/4/00	1186017	1869	minbias	Q. Liu says ZDC vs. mult looks bad
7/24/00	1206003	1635	minbias	evidence of strong azimuthal quadrupole dependence in track direction
7/25/00	1207007	1013	minbias	trigger timing studies during run
8/6/00	1219008	158	minbias	evidence of strong azimuthal quadrupole dependence in track direction
8/6/00	1219023	1139	peripheral	peripheral trigger
8/6/00	1219026	4016	peripheral	peripheral trigger
8/6/00	1219027	382	minbias	notOK-rejected in production
8/8/00	1221004	516	minbias	evidence of strong azimuthal quadrupole dependence in track direction
8/8/00	1221013	23	minbias	notOK-rejected in production
8/8/00	1221014	147	minbias	evidence of strong azimuthal quadrupole dependence in track direction
8/8/00	1221019	516	peripheral	peripheral trigger
8/8/00	1221020	1353	peripheral	peripheral trigger
8/9/00	1222002	2016	peripheral	peripheral trigger
8/9/00	1222003	2016	peripheral	peripheral trigger
8/14/00	1227023	1025	peripheral	peripheral trigger
8/14/00	1227024	1036	peripheral	peripheral trigger
8/14/00	1227025	1019	peripheral	peripheral trigger
8/15/00	1228004	10015	minbias	TPC voltage change
8/15/00	1228006	811	minbias	Z. Xu says run fishy; bad trigger/RHIC clock sync
8/15/00	1228007	516	minbias	Z. Xu says run fishy; bad trigger/RHIC clock sync
8/15/00	1228008	5771	minbias	Z. Xu says run fishy; bad trigger/RHIC clock sync
8/15/00	1228009	4596	minbias	Z. Xu says run fishy; bad trigger/RHIC clock sync
8/15/00	1228010	10013	minbias	Z. Xu says run fishy; bad trigger/RHIC clock sync
8/15/00	1228012	7227	laser	laser trigger

Table A.2: Suspect STAR data runs from 2000 with logbook notes, continues on the next two pages.

date	run number	number events	kind of trigger	reason not to use
8/15/00	1228014	4466	minbias	Z. Xu says run fishy; bad trigger/RHIC clock sync
8/15/00	1228016	1406	minbias	Z. Xu says run fishy; bad trigger/RHIC clock sync
8/15/00	1228029	16166	minbias	Z. Xu says run fishy; bad trigger/RHIC clock sync
8/16/00	1228031	1089	minbias	bad; LASER trigger?
8/16/00	1229009	2249	central	not analyzed in P01he; dN/dnch is minbias!
8/16/00	1229010	13239	central	not analyzed in P01he; dN/dnch is minbias!
8/16/00	1229011	2289	central	not analyzed in P01he; dN/dnch is minbias!
8/16/00	1229013	18274	central	not analyzed in P01he; dN/dnch is minbias!
8/16/00	1229021	30031	central	not analyzed in P01he; dN/dnch is minbias!
8/16/00	1229023	10011	central	not analyzed in P01he; dN/dnch is minbias!
8/16/00	1229029	6702	minbias	magnet problem during run
8/17/00	1230013	2572	minbias	Primvtx = 50%; suspect run
8/17/00	1230018	10014	minbias	production notes indicate beam-gas type events; suspect
8/17/00	1230019	356	minbias	notOK-rejected by production
8/17/00	1230021	20772	minbias	TPC sector 6 section 8 turned off
8/18/00	1231007	25014	minbias	production trouble
8/20/00	1233040	9	minbias	production reject L3 test runs
8/20/00	1233041	2767	minbias	L3 test runs
8/20/00	1233042	116	minbias	production reject L3 test runs
8/22/00	1235029	10008	peripheral	peripheral trigger
8/22/00	1235034	1503	minbias	L3 test runs
8/24/00	1237021	8295	minbias	notOK according to production
8/24/00	1237026	4692	minbias	Magnet trip during run
8/24/00	1237034	6499	minbias	Magnet trip during run
8/25/00	1238005	9994	central	rejected in production; dN/dnch is minbias!
8/25/00	1238008	10014	central	rejected in production; dN/dnch is minbias!
8/25/00	1238016	14699	minbias	rejected by production
8/26/00	1239006	5495	minbias	L3 test runs
8/27/00	1240008	9576	laser	laser trigger

Table A.2: continued. Suspect STAR data runs from 2000 with logbook notes, continued from previous page.

date	run number	number events	kind of trigger	reason not to use
8/28/00	1241003	6808	central	TPC anode trip
8/28/00	1241016	7146	central	Physics B trigger; wrong
8/30/00	1243022	7295	minbias	TPC anode trip
8/30/00	1243059	29380	central	TPC trip inner sector
9/1/00	1245012	11501	central	TPC Anode trip during run
9/1/00	1245013	6274	central	TPC anode wire trip
9/2/00	1246017	30008	laser	laser trigger
9/3/00	1247009	11207	central	Physics B trigger; wrong
9/3/00	1247021	1606	peripheral	peripheral trigger
9/3/00	1247022	1459	peripheral	peripheral trigger
9/3/00	1247036	7139	peripheral	peripheral trigger
9/3/00	1247037	3314	peripheral	peripheral trigger
9/3/00	1247038	12543	central	TPC anode trip during run
9/3/00	1247039	11213	central	part of TPC sector number23 bad
9/4/00	1248004	38135	laser	laser trigger
9/4/00	1248011	10012	central	TPC anode trip sector 5
9/4/00	1248018	7080	minbias	rejected by production
9/4/00	1248024	3276	central	magnet drop

Table A.2: continued. Suspect STAR data runs from 2000 with logbook notes, continues from the previous two pages.

HIJING label	number of files	trigger	files used	events kept for balance function
b0-15b	34	hijing minimum bias	reco/auau130/hijing/b0_15/year_1h/ reco/auau130/hijing/b0_15/year_1h/ halffield/hadronic_on/trs_1i/ rcf0146_*_* evts.dst.root	9,689
b0-3	48	hijing central	reco/auau130/hijing/b0_3/year_1e/ halffield/hadronic_on/trs_1i/ rcf0147_*_* evts.dst.root	3,290
b0-3 jet05	18	hijing central jet5	reco/auau130/hijing/b0_3_jet05/year_1h/ halffield/hadronic_on/trs_1i/ rcf0145_*_* evts.dst.root	1,350
b3-6	127	hijing midcentral	reco/auau130/hijing/b3_6/year_1e/ halffield/hadronic_on/trs_1i/ rcf0148_*_* evts.dst.root	11,373
b0-15	169	hijing minimum bias	reco/auau130/hijing/b0_15/year_1h/ halffield/hadronic_on/trs_1i/ rcf0146_*_* evts.dst.root	47,829
			total	73,531

Table A.3: HIJING files used in simulation analysis. These have been run through GSTAR and TRS.

LIST OF REFERENCES

[1] J. W. Harris and B. Muller, Ann. Rev. Nucl. Part. Sci. **46**, 71 (1996) [arXiv:hep-ph/9602235].

[2] J. W. Harris, *Prepared for Lake Louise Winter Institute: Quantum Chromodynamics, Lake Louise, Alberta, Canada, 15-21 Feb 1998.*

[3] M. E. Peskin and D. V. Schroeder, *An Introduction to Quantum Field Theory* (Addison-Wesley, Reading, Massachusetts, 1995)

[4] R. Hwa, *Quark-Gluon Plasma* (World Scientific, Singapore, 1995), Vol. 2.

[5] CERN SPS, http://cern.web.cern.ch/CERN/Announcements/2000/NewStateMatter/, and http://public.web.cern.ch/Public/SCIENCE/heavyions.html, published on the internet.

[6] I. G. Bearden *et al.* [NA44 Collaboration], Phys. Rev. Lett. **78**, 2080 (1997).

[7] H. Beker *et al.*, Phys. Rev. Lett. **74**, 3340 (1995).

[8] I. Bearden *et al.* [NA44 Collaboration], Phys. Lett. B **471**, 6 (1999) [arXiv:nucl-ex/9907013].

[9] G. Agakishiev *et al.* [CERES/NA45 Collaboration], Phys. Lett. B **422**, 405 (1998) [arXiv:nucl-ex/9712008].

[10] B. Lenkeit *et al.* [CERES-Collaboration], Nucl. Phys. A **661**, 23 (1999) [arXiv:nucl-ex/9910015].

[11] J. Bachler *et al.* [NA49 Collaboration], Nucl. Phys. A **661**, 45 (1999).

[12] H. Appelshauser *et al.* [NA49 Collaboration], Eur. Phys. J. C **2**, 661 (1998) [arXiv:hep-ex/9711024].

[13] S. Margetis *et al.* [NA49 Collaboration], Phys. Rev. Lett. **75**, 3814 (1995).

[14] M. C. Abreu *et al.* [NA50 Collaboration], Phys. Lett. B **410**, 337 (1997).

[15] M. C. Abreu *et al.* [NA50 Collaboration], Phys. Lett. B **477**, 28 (2000).

[16] M. Gonin *et al.* [NA50 Collaboration], Nucl. Phys. A **610**, 404C (1996).

[17] G. Ambrosini *et al.* [NA52 (NEWMASS) Collaboration], New Jour. Phys. **1**, 22 (1999).

[18] R. Klingenberg *et al.* [NA52 (NEWMASS) Collaboration], Nucl. Phys. A **610**, 306C (1996).

[19] G. Ambrosini *et al.* [NA52 (NEWMASS) Collaboration], Phys. Lett. B **417**, 202 (1998).

[20] F. Antinori *et al.* [WA97 Collaboration], Nucl. Phys. A **661**, 130 (1999).

[21] F. Antinori *et al.* [WA97 Collaboration], Eur. Phys. J. C **14**, 633 (2000).

[22] E. Andersen *et al.* [WA97 Collaboration], Phys. Lett. B **449**, 401 (1999).

[23] M. M. Aggarwal *et al.* [WA98 Collaboration], Phys. Rev. Lett. **83**, 926 (1999) [arXiv:nucl-ex/9901009].

[24] R. Albrecht *et al.* [WA80 Collaboration], Phys. Rev. Lett. **76**, 3506 (1996).

[25] M. M. Aggarwal *et al.* [WA98 Collaboration], Phys. Rev. Lett. **81**, 4087 (1998) [Erratum-ibid. **84**, 578 (1998)] [arXiv:nucl-ex/9806004].

[26] S. A. Bass, arXiv:nucl-th/0202010.

[27] STAR image library, http://www.star.bnl.gov/STAR/img/images.html, 2002, published on the internet.

[28] J. W. Harris [STAR Collaboration], Nucl. Phys. A **566**, 277C (1994).

[29] K. H. Ackermann *et al.* [STAR Collaboration], Phys. Rev. Lett. **86**, 402 (2001) [arXiv:nucl-ex/0009011].

[30] C. Adler [the STAR Collaboration], Phys. Rev. Lett. **86**, 4778 (2001) [arXiv:nucl-ex/0104022].

[31] C. Adler *et al.* [STAR Collaboration], Phys. Rev. Lett. **87**, 082301 (2001) [arXiv:nucl-ex/0107008].

[32] C. Adler *et al.* [STAR Collaboration], Phys. Rev. Lett. **87**, 112303 (2001) [arXiv:nucl-ex/0106004].

[33] C. Adler *et al.* [STAR Collaboration], Phys. Rev. Lett. **87**, 182301 (2001) [arXiv:nucl-ex/0107003].

[34] C. Adler *et al.* [STAR Collaboration], Phys. Rev. Lett. **87**, 262301 (2001) [Erratum-ibid. **87**, 279902 (2001)] [arXiv:nucl-ex/0108022].

[35] C. Adler *et al.* [STAR Collaboration], Phys. Rev. Lett. **87**, 262302 (2001) [arXiv:nucl-ex/0110009].

[36] G. Schroeder, RHIC, http://www.bnl.gov/RHIC, 2000, published on the internet.

[37] M. Calderon, Ph.D. thesis, Yale University, Connecticut, 2001, unpublished.

[38] K. H. Ackermann *et al.* [STAR Collaboration], Nucl. Phys. A **661**, 681 (1999) [Nucl. Phys. A **698**, 408 (1999)].

[39] S. R. Klein *et al.*, IEEE Trans. Nucl. Sci. **43**, 1768 (1996).

[40] W. Betts *et al.*, IEEE Trans. Nucl. Sci. **44**, 592 (1997).

[41] C. Adler, H. Strobele, A. Denisov, E. Garcia, M. Murray and S. White, Nucl. Instrum. Meth. A **461**, 337 (2001).

[42] J. S. Lange *et al.*, Nucl. Instrum. Meth. A **453**, 397 (2000).

[43] Spencer Klein, private communication.

[44] B. Muller, arXiv:nucl-th/0111008.

[45] STAR collaboration, StEvent Reference Manual v2.5.7, 2001, (unpublished).

[46] STAR collaboration, STAR C++ Class Reference Manual v1.19, 2000, (unpublished).

[47] S. A. Bass, P. Danielewicz and S. Pratt, Phys. Rev. Lett. **85**, 2689 (2000) [arXiv:nucl-th/0005044], and references therein.

[48] D. Drijard *et al.* [ACCDHW Collaboration], Nucl. Phys. B **166**, 233 (1980).

[49] H. Aihara *et al.* [TPC/Two Gamma Collaboration], Phys. Rev. Lett. **53**, 2199 (1984).

[50] H. Aihara *et al.* [TPC/Two Gamma Collaboration], Phys. Rev. Lett. **57**, 3140 (1986).

[51] S. A. Bass, M. Gyulassy, H. Stocker and W. Greiner, J. Phys. G **25**, R1 (1999) [arXiv:hep-ph/9810281].

[52] J. D. Bjorken, Phys. Rev. D **27**, 140 (1983).

[53] T. Sjostrand, L. Lonnblad and S. Mrenna, arXiv:hep-ph/0108264.

[54] B. Andersson, G. Gustafson and B. Nilsson-Almqvist, Nucl. Phys. B **281**, 289 (1987).

[55] STAR Computing web pages, http://www.star.bnl.gov/STAR/comp, 2002, published on the internet.

[56] STAR newsletter, October 2000, (unpublished).

[57] X. N. Wang and M. Gyulassy, Phys. Rev. D **44**, 3501 (1991).

[58] STAR collaboration, STAR TRS (TPC Response Simulator) User Guide and Reference Manual, v1.3, 1999, (unpublished).

[59] P. Jacos, D. Irmscher, GSTAR Technical Report, STAR Note 235, 1996 (unpublished).

[60] STAR TRS and Embedding mailing list discussions, internal report (unpublished).

[61] Particle Data Group, *Particle Physics Booklet* (Springer, Berkeley, 2000), extracted from *Rev. Part. Phys.*, D. Groom *et al.* , The European Physical Journal **C15** (200) 1 (http://pdg.lbl.gov).

[62] U. W. Heinz and B. V. Jacak, Ann. Rev. Nucl. Part. Sci. **49**, 529 (1999) [arXiv:nucl-th/9902020].

[63] S. y. Jeon and S. Pratt, arXiv:hep-ph/0110043.

[64] S. Jeon and V. Koch, Phys. Rev. Lett. **85**, 2076 (2000) [arXiv:hep-ph/0003168].

[65] M. Asakawa, U. W. Heinz and B. Muller, Phys. Rev. Lett. **85**, 2072 (2000) [arXiv:hep-ph/0003169].

[66] CERN Program Library Long Writeups Q123, GEANT Detector Description and Simulation Tool by Application Software Group, 1993.

[67] B. Lasiuk, Technical Report No. YRHI-99-29, Yale University, Physics of the TPC Response Simulator (unpublished).

[68] H. Sorge, Phys. Rev. C **52**, 3291 (1995) [arXiv:nucl-th/9509007].

[69] S. Bass, private communication.

[70] S. Pratt, 18th Winter Workshop on Nuclear Dynamics, Nassau (preliminary)

[71] T. A. Trainor, arXiv:hep-ph/0001148.

[72] T. A. Trainor and J. G. Reid, arXiv:hep-ph/0004258.

[73] D. A. Brown and P. Danielewicz, Phys. Rev. C **64**, 014902 (2001) [arXiv:nucl-th/0010108].

[74] F. Retiere [STAR Collaboration], arXiv:nucl-ex/0111013.

[75] A. Poskanser, private communication.

[76] D. Griffiths, *Introduction to Elementary Particles* (John Wiley & Sons, New York, 1987)

[77] W. S. C. Williams, *Nuclear and Particle Physics* (Oxford University Press, New York, 1991)

[78] S. Weinberg, *The First Three Minutes* (Basic Books, Inc., New York, 1988)

[79] F. Halzen and A. D. Martin, *Quarks and Leptons* (John Wiley & Sons, New York, 1984)

[80] R.K. Bock and W. Krischer, The Data Analysis Brief Book, CERN, http://physics.web.cern.ch/Physics/DataAnalysis/BriefBook/ .

[81] R.K. Bock and A. Vasilescu, The Particle Detector Brief Book, CERN, http://rd11.web.cern.ch/RD11/rkb/titleD.html .

[82] J. R. Taylor, *An Introduction to Error Analysis* (University Science Books, Sausalito, 1997), 2nd ed.

[83] H. M. Deitel, P. J. Deitel, *C++ How to Program* (Prentice Hall, New Jersey, 1994)

[84] K. Kleinknecht, *Detectors for Particle Radiation* (Cambridge University Press, Cambridge, 1990)

[85] R. Hagedorn, *Relativistic Kinematics* (W. A. Benjamin, Inc., New York, 1963)

[86] H. Caines [STAR Collaboration], *In *Atlanta 1999, Heavy ion physics* 131-135.*

[87] J. Whitmore, Phys. Rept. **27**, 187 (1976).

[88] L. McLerran, arXiv:hep-ph/0202025.

[89] K. Adcox *et al.* [PHENIX Collaboration], arXiv:nucl-ex/0201008.

[90] D. P. Mahapatra, B. Mohanty and S. C. Phatak, arXiv:nucl-ex/0108011.

[91] B. B. Back *et al.* [PHOBOS Collaboration], Phys. Rev. Lett. **85**, 3100 (2000) [arXiv:hep-ex/0007036].

[92] F. W. Bopp and J. Ranft, Eur. Phys. J. C **22**, 171 (2001) [arXiv:hep-ph/0105192].

[93] C. Spieles, H. Stocker and C. Greiner, Phys. Rev. C **57**, 908 (1998) [arXiv:hep-ph/9708280].

[94] E. E. Zabrodin, L. V. Bravina, L. P. Csernai, H. Stocker and W. Greiner, Phys. Lett. B **423**, 373 (1998) [arXiv:hep-ph/9806207].

[95] E. V. Shuryak, Phys. Lett. B **423**, 9 (1998) [arXiv:hep-ph/9704456].

[96] K. Adcox *et al.* [PHENIX Collaboration], Phys. Rev. Lett. **87**, 052301 (2001) [arXiv:nucl-ex/0104015].

[97] K. Adcox *et al.* [PHENIX Collaboration], Phys. Rev. Lett. **86**, 3500 (2001) [arXiv:nucl-ex/0012008].

[98] L. Lamport, *LaTeX Users's Guide and Reference Manual* (Addison-Wesley, Boston, 1985)